2.18 Constitutive Equations, Rheological Behavior, and Viscosity of Rocks

DL Kohlstedt, University of Minnesota, Minneapolis, MN, USA
LN Hansen, University of Oxford, Oxford, UK

This chapter is a revision of the previous edition chapter by D L Kohlstedt, Volume 2, pp. 389–427, © 2007, Elsevier B.V.

2.18.1 Introduction

The rheological behavior of mantle rocks determines the mechanical response of lithospheric plates and the nature of convective flow in the deeper mantle. Geodynamic models of these large-scale processes require constitutive equations that describe rheological properties of the appropriate mantle rocks. The forms of such constitutive equations (flow laws or combinations of flow laws) are motivated by micromechanical analyses of plastic deformation phenomena based on physical processes such as ionic diffusion, dislocation migration, and grain-boundary sliding. Critical parameters in flow laws appropriate for rock deformation such as the dependence of strain rate on stress, grain size, temperature (activation energy), and pressure (activation volume) must be determined from well-designed, carefully executed laboratory experiments. Geophysical observations of the mechanical behavior of Earth's mantle in response to changes in the stress environment due, for example, to an earthquake or the retreat of a glacier provide tests of the applicability of the resulting constitutive equations to deformation occurring under geologic conditions.

Confident extrapolation of flow laws determined under laboratory conditions requires an understanding of the physical processes involved in deformation. Minerals and rocks deform plastically by a number of different mechanisms, each of which requires defects in the crystalline structure. Diffusion creep involves the movement of atoms or ions and thus of point defects; dislocation creep entails the glide and climb of line defects; grain-boundary sliding necessitates motion along planar defects. Within any deformation regime, more than one deformation process may be important. For example, diffusion creep can be divided into one regime dominated by diffusion along grain boundaries and another dominated by diffusion through grain interiors (the so-called grain matrix). Grain size, temperature, and pressure dictate which of these two processes is more important. Likewise, in dislocation creep, deformation can be divided into low-temperature and high-temperature regimes, with glide of dislocations controlling the rate of deformation in the former and climb of dislocations in the latter. As temperature decreases, differential stress necessarily increases if deformation is to continue at a given rate.

Plastic deformation is a thermally activated, kinetic, and irreversible process. Experimentalists frame laboratory investigations of plastic deformation in terms of strain rate as a function of differential stress, temperature, pressure, and grain size and other microstructural and chemical parameters. In contrast, geodynamicists cast plasticity in terms of viscosity, the ratio of stress to strain rate. In both cases, flow laws or constitutive equations describe the relationships between these parameters, thus providing the basis for extrapolating from laboratory to Earth conditions. Tests of the appropriateness of laboratory-derived flow laws to processes occurring in Earth at much slower strain rates (higher viscosities) – and thus necessarily much lower stresses and/or much lower temperatures and/or much coarser grain sizes – include comparisons of microstructures observed in experimentally deformed samples with those in naturally deformed rocks and of viscosities derived from laboratory experiments with those determined from geophysical observations.

This chapter, therefore, starts with an examination of the role of defects in plastic deformation, including a discussion of the influence of water-derived point defects on kinetic processes. Next, a section on some of the important mechanisms of deformation introduces constitutive equations that describe plastic flow by linking thermomechanical parameters such as strain rate, differential stress, temperature, pressure, and water fugacity with structural parameters such as dislocation density, grain size, and melt fraction. Finally, profiles of viscosity versus depth in the upper mantle are used to test the applicability of flow laws determined from micromechanical models and laboratory experiments to plastic flow taking place deep beneath Earth's surface.

2.18.2 Role of Lattice Defects in Deformation

Defects in rocks are essential for plastic deformation to proceed. Zero-dimensional or point defects (specifically vacancies and self-interstitials) allow flow by diffusive transport of ions, one-dimensional or line defects (dislocations) permit deformation by glide and climb, and two-dimensional or planar defects (grain–grain interfaces) facilitate deformation involving grain-boundary sliding and migration. More than one type of defect may be simultaneously involved in deformation. For example, diffusion creep involves not only diffusion by a point defect mechanism but also sliding on grain boundaries (Raj and Ashby, 1971), dislocation processes also frequently couple with grain-boundary sliding (Langdon, 1994), and dislocation creep necessitates glide on several slip systems often combined with climb (Groves and Kelly, 1969; Paterson, 1969; von Mises, 1928). In addition, dynamic recrystallization frequently acts as a recovery mechanism, producing a new generation of dislocation-free grains that are more easily deformed than the parent grains (e.g., de Bresser et al., 2001; Drury, 2005; Platt and Behr, 2011; Tullis and Yund, 1985). In this section, some fundamental aspects of point defects, dislocations, and grain boundaries are introduced as background for discussing the rheological behavior of rocks and the associated constitutive equations.

2.18.2.1 Point Defects: Thermodynamics and Kinetics

2.18.2.1.1 Thermodynamics

At temperatures above absolute zero, crystalline grains in thermodynamic equilibrium contain finite populations of vacancies and self-interstitials. Although the enthalpy of a crystal increases linearly with the addition of vacancies or self-interstitials, the entropy decreases nonlinearly. Hence, the Gibbs free energy of a crystal is minimized not when the crystal is perfect (i.e., defect-free) but rather when the crystal contains a finite concentration of vacancies and self-interstitials (i.e., when the crystal is imperfect) (see, e.g., Devereux, 1983, pp. 296–300). In metals, the concentrations of these point defects in thermodynamic equilibrium are determined by temperature and pressure through their Gibbs free energies of formation (Schmalzried, 1981, pp. 37–38). In ionic materials, the situation is more complicated because the concentrations of the different types of point defects are coupled through the necessity for electroneutrality, which requires that the sum of the concentrations of the various types of positively charged point defects equals the sum of the concentrations of all of the negatively charged point defects (Schmalzried, 1981, pp. 38–42). The concentration of one type of positively charged point defect often greatly exceeds the concentrations of the other positively charged point defects; a similar situation frequently exists for negatively charged defects. This combination of positive and negative defects defines the majority point defects or the defect type. The charge neutrality condition is then approximated by equating the concentration of the positively charged to the concentration of the negatively charged majority point defects. An example serves to illustrate the salient elements of point defect thermodynamics.

Consider the case of a simple metal oxide, MeO, where Me is an ion such as Mg, Ni, Co, Mn, or Fe. Structural elements for this system include $\mathrm{Me}_{\mathrm{Me}}^{\times}$, $\mathrm{O}_{\mathrm{O}}^{\times}$, $\mathrm{Me}_{\mathrm{Me}}^{\bullet}$, $\mathrm{Me}_{\mathrm{i}}^{\bullet\bullet}$, $\mathrm{V}_{\mathrm{O}}^{\bullet\bullet}$, $\mathrm{V}_{\mathrm{Me}}^{//}$, and $\mathrm{O}_{\mathrm{i}}^{//}$. The first two entries are termed 'regular structural elements' and the last five are called 'irregular structural elements' or point defects in the ideal crystal lattice. The Kröger–Vink (1956) notation is used to indicate the atomic species, A, occupying a specific crystallographic site, S, and having an effective charge, C, relative to the ideal crystal lattice: $\mathrm{A}_{\mathrm{S}}^{\mathrm{C}}$. In this nomenclature, the superscripted symbols ×, •, and / indicate neutral, one positive, and one negative effective charges. Vacant sites are denoted by a V, and ions located at interstitial sites are indicated by a subscripted i. The defect $\mathrm{Me}_{\mathrm{Me}}^{\bullet}$ corresponds to a 3+ ion sitting at a site normally occupied by a 2+ ion, such as a ferric iron in a ferrous iron site. In a strict sense, charge neutrality is given by

$$\left[\mathrm{Me}_{\mathrm{Me}}^{\bullet}\right]+2\left[\mathrm{V}_{\mathrm{O}}^{\bullet\bullet}\right]+2\left[\mathrm{Me}_{\mathrm{i}}^{\bullet\bullet}\right]=2\left[\mathrm{V}_{\mathrm{Me}}^{//}\right]+2\left[\mathrm{O}_{\mathrm{i}}^{//}\right] \qquad [1a]$$

where the square brackets, [ ], indicate molar concentration. In a Mg-rich system, one possible disorder type is the combination $\mathrm{Me}_{\mathrm{i}}^{\bullet\bullet}$ and $\mathrm{V}_{\mathrm{Me}}^{//}$ (Catlow et al., 1994), such that the charge neutrality condition is approximated as

$$\left[\mathrm{Me}_{\mathrm{i}}^{\bullet\bullet}\right]=\left[\mathrm{V}_{\mathrm{Me}}^{//}\right] \qquad [1b]$$

In contrast, in an Fe-rich quasi-binary material such as (Mg,Fe)O, likely majority point defects are $\mathrm{Fe}_{\mathrm{Me}}^{\bullet}$ and $\mathrm{V}_{\mathrm{Me}}^{//}$ (Hilbrandt and Martin, 1998), yielding the charge neutrality condition

$$\left[\mathrm{Fe}_{\mathrm{Me}}^{\bullet}\right]=2\left[\mathrm{V}_{\mathrm{Me}}^{//}\right] \qquad [1c]$$

where $\mathrm{Fe}_{\mathrm{Me}}^{\bullet}$ is often written as $\mathrm{h}^{\bullet}$, indicating a highly mobile electron hole localized at a Fe^{2+} site.

To obtain expressions that give the dependences of point defect concentrations on thermodynamic variables such as temperature, pressure, and component activities, reaction equations are needed. The first reaction equation should involve the majority point defects. In the case of the Frenkel disorder type given by eqn [1b], the appropriate reaction starts with a regular structural element resulting in

$$\mathrm{Me}^{\times}_{\mathrm{Me}} \leftrightarrow \mathrm{Me}^{\bullet\bullet}_{\mathrm{i}} + \mathrm{V}^{//}_{\mathrm{Me}} \qquad [2]$$

for which the law of mass action yields

$$a_{\mathrm{Me}^{\bullet\bullet}_{\mathrm{Me}}} a_{\mathrm{V}^{//}_{\mathrm{Me}}} = a_{\mathrm{Me}^{\times}_{\mathrm{Me}}} K_2 \qquad [3a]$$

where $K_2 = K_\mathrm{F}$ is the reaction constant for the reaction in eqn [2]. Since the activity of $\mathrm{Me}^{\times}_{\mathrm{Me}}$ is little affected by the presence of a small concentration of point defects (typically $<10^{-3}$), $a_{\mathrm{Me}^{\times}_{\mathrm{Me}}} \approx \left[\mathrm{Me}^{\times}_{\mathrm{Me}}\right] \approx 1$. Likewise, for ideally dilute solutions of point defects, the activities of the point defects can be replaced by their concentrations such that eqn [3a] becomes

$$\left[\mathrm{Me}^{\bullet\bullet}_{\mathrm{i}}\right]\left[\mathrm{V}^{//}_{\mathrm{Me}}\right] = K_F = \exp\frac{-G_\mathrm{F}}{RT} \qquad [3b]$$

where G_F is the Gibbs free energy for the reaction in eqn [2] and RT has the usual meaning. This reaction describes the formation of the so-called Frenkel point defects (a vacancy–interstitial pair). If the charge neutrality condition in eqn [1b] and the mass action equation in eqn [3b] are combined, the dependence on temperature and pressure of the concentrations of the Frenkel defects is

$$\left[\mathrm{Me}^{\bullet\bullet}_{\mathrm{i}}\right] = \left[\mathrm{V}^{//}_{\mathrm{Me}}\right] = \sqrt{K_\mathrm{F}} = \exp\frac{-G_\mathrm{F}}{2RT} \qquad [4]$$

Frenkel majority point defects are an example of a thermal disorder type, that is, the concentrations of these point defects depend on temperature and pressure but not on the activities of the components. A second example of thermal disorder occurs if Schottky point defects, $\mathrm{V}^{//}_{\mathrm{Me}}$ and $\mathrm{V}^{\bullet\bullet}_{\mathrm{O}}$, are the majority point defects.

For the disorder type given by eqn [1c], the appropriate reaction involves a regular structural element plus a neutral crystal component to yield

$$\frac{1}{2}\mathrm{O}_2(\mathrm{srg}) + 2\mathrm{Fe}^{\times}_{\mathrm{Me}} + \mathrm{Me}^{\times}_{\mathrm{Me}} \leftrightarrow 2\mathrm{Fe}^{\bullet}_{\mathrm{Me}} + \mathrm{V}^{//}_{\mathrm{Me}} + \mathrm{MeO}(\mathrm{srg}) \qquad [5]$$

where the oxygen is provided from a site of repeatable growth (srg) such as a dislocation, grain boundary, or crystal–gas interface (surface). The law of mass action yields

$$\left[\mathrm{Fe}^{\bullet}_{\mathrm{Me}}\right]^2\left[\mathrm{V}^{//}_{\mathrm{Me}}\right] a_{\mathrm{MeO}} = \left[\mathrm{Fe}^{\times}_{\mathrm{Me}}\right]^2\left[\mathrm{Me}^{\times}_{\mathrm{Me}}\right] f^{1/2}_{\mathrm{O}_2} K_5 \qquad [6]$$

where f_{O_2} is the oxygen fugacity. If the charge neutrality condition in eqn [1c] is now substituted into eqn [6] and the approximation $[\mathrm{Me}^{\times}_{\mathrm{Me}}] \approx a_{\mathrm{MeO}} = 1$ is made, then

$$\begin{aligned}\left[\mathrm{Fe}^{\bullet}_{\mathrm{Me}}\right] &= 2\left[\mathrm{V}^{//}_{\mathrm{Me}}\right] = \sqrt[3]{2}\left[\mathrm{Fe}^{\times}_{\mathrm{Me}}\right]^{2/3} f^{1/6}_{\mathrm{O}_2} K^{1/3}_5 \\ &= \sqrt[3]{2}\left[\mathrm{Fe}^{\times}_{\mathrm{Me}}\right]^{2/3} f^{1/6}_{\mathrm{O}_2} \exp\frac{-G_5}{3RT} \qquad [7]\end{aligned}$$

Thus, if a neutral crystal component is added from a site of repeatable growth, the concentrations of the majority point defects will depend not only on pressure and temperature but also on component activities, often referred to as an activity-dependent disorder type. In this case, it should be noted that the material will be nonstoichiometric with typically $[\mathrm{V}^{//}_{\mathrm{Me}}] >> [\mathrm{V}^{\bullet\bullet}_{\mathrm{O}}]$. Also, a comparison of eqn [4] with eqn [7] demonstrates that the functional form and the magnitude of the concentration of $\mathrm{V}^{//}_{\mathrm{Me}}$ depend on the charge neutrality condition.

Since $[\mathrm{V}^{\bullet\bullet}_{\mathrm{O}}]$ is generally several orders of magnitude smaller than $[\mathrm{V}^{//}_{\mathrm{Me}}]$, O diffuses much more slowly than Me, at least through the interiors of grains. Consequently, as discussed later in the text, the rate of diffusion creep (specifically, Nabarro–Herring creep) and rate of dislocation climb are limited by the rate of O diffusion. Hence, it is important to examine the dependence of the concentration of $\mathrm{V}^{\bullet\bullet}_{\mathrm{O}}$ on temperature, pressure, and oxygen fugacity. Since the dependence of the concentration of $\mathrm{V}^{//}_{\mathrm{Me}}$ on these parameters has been determined earlier in the text, the formulation of a reaction involving $\mathrm{V}^{\bullet\bullet}_{\mathrm{O}}$ and $\mathrm{V}^{//}_{\mathrm{Me}}$ provides a good starting point. The point defects $\mathrm{V}^{\bullet\bullet}_{\mathrm{O}}$ and $\mathrm{V}^{//}_{\mathrm{Me}}$ are related via the Schottky formation reaction

$$\mathrm{Me}^{\times}_{\mathrm{Me}} + \mathrm{O}^{\times}_{\mathrm{O}} \leftrightarrow \mathrm{V}^{//}_{\mathrm{Me}} + \mathrm{V}^{\bullet\bullet}_{\mathrm{O}} + \mathrm{MeO} \qquad [8]$$

It should be emphasized that it is essential in reaction equations such as eqn [8] that the number and identity of the atomic species, the crystallographic sites, and the effective charges (recall $\mathrm{A}^{\mathrm{C}}_{\mathrm{S}}$) be the same on the two sides of the reaction equation. The law of mass action for eqn [8] reads

$$\left[\mathrm{V}^{//}_{\mathrm{Me}}\right]\left[\mathrm{V}^{\bullet\bullet}_{\mathrm{O}}\right] = K_\mathrm{S} = \exp\frac{-G_\mathrm{S}}{RT} \qquad [9]$$

again using the approximations $a_{\mathrm{Me}^{\times}_{\mathrm{Me}}} \approx a_{\mathrm{O}^{\times}_{\mathrm{O}}} \approx 1$ with a_{MeO} equal to unity since MeO is present. For the Frenkel thermal disorder type given by eqn [1b], $[\mathrm{Me}^{\bullet\bullet}_{\mathrm{i}}] = [\mathrm{V}^{//}_{\mathrm{Me}}]$, if eqn [9] is now combined with eqn [4], then

$$\left[\mathrm{V}^{\bullet\bullet}_{\mathrm{O}}\right] = \left[\mathrm{V}^{//}_{\mathrm{Me}}\right]^{-1} K_\mathrm{S} = \frac{K_\mathrm{S}}{\sqrt{K_\mathrm{F}}} = \exp\frac{-(G_\mathrm{S} - G_\mathrm{F}/2)}{RT} \qquad [10]$$

For the activity-dependent disorder type given by eqn [1c], $[\mathrm{Fe}^{\bullet}_{\mathrm{Me}}] = 2[\mathrm{V}^{//}_{\mathrm{Me}}]$, if eqn [9] is combined with eqn [7], then

$$\begin{aligned}\left[\mathrm{V}^{\bullet\bullet}_{\mathrm{O}}\right] &= \left[\mathrm{V}^{//}_{\mathrm{Me}}\right]^{-1} K_8 = \sqrt[3]{4}\left[\mathrm{Fe}^{\times}_{\mathrm{Me}}\right]^{-2/3} f^{-1/6}_{\mathrm{O}_2} \frac{K_\mathrm{S}}{K^{1/3}_5} \\ &= \sqrt[3]{4}\left[\mathrm{Fe}^{\times}_{\mathrm{Me}}\right]^{-2/3} f^{-1/6}_{\mathrm{O}_2} \exp\frac{-(G_\mathrm{S} - G_5/3)}{RT} \qquad [11]\end{aligned}$$

Under hydrous conditions, additional point defects must be considered. Hydrogen ions, that is, protons, $\mathrm{p}^{\bullet}$, occupy interstitial sites, $\mathrm{H}^{\bullet}_{\mathrm{i}}$, near oxygen ions, thus corresponding to hydroxyl point defects, $(\mathrm{OH})^{\bullet}_{\mathrm{O}}$. This water-derived point defect can be introduced through dissociation of a water molecule by the reaction

$$\mathrm{H}_2\mathrm{O}(\mathrm{srg}) + 2\mathrm{O}^{\times}_{\mathrm{O}} + \mathrm{Me}^{\times}_{\mathrm{Me}} \leftrightarrow 2(\mathrm{OH})^{\bullet}_{\mathrm{O}} + \mathrm{V}^{//}_{\mathrm{Me}} + \mathrm{MeO}(\mathrm{srg}) \qquad [12]$$

In addition, point defect associates such as those produced between $(\mathrm{OH})^{\bullet}_{\mathrm{O}}$ and $\mathrm{V}^{//}_{\mathrm{Me}}$ can form

$$(\mathrm{OH})^{\bullet}_{\mathrm{O}} + \mathrm{V}^{//}_{\mathrm{Me}} \leftrightarrow \left\{(\mathrm{OH})^{\bullet}_{\mathrm{O}} - \mathrm{V}^{//}_{\mathrm{Me}}\right\}^{/} \qquad [13]$$

where the curly brackets, { }, indicate a defect associate. This and other defect associates and $(\mathrm{OH})^{\bullet}_{\mathrm{O}}$ must now be included in the charge neutrality equation, eqn [1a]. Note that the defect associate $\{(\mathrm{OH})^{\bullet}_{\mathrm{O}} - \mathrm{V}^{//}_{\mathrm{Me}}\}^{/}$ is sometimes written in shorthand as $\mathrm{H}_{\mathrm{Me}}^{/}$. It should be kept in mind that, as stated in the preceding text, protons occupy interstitial sites that are located very near oxygen ions giving rise to hydroxyl point defects; protons (or equivalently hydroxyl defects) can form defect associates with metal vacancies; however, they do not literally occupy metal vacancies. New disorder types such as

$$\left[(\mathrm{OH})_{\mathrm{O}}^{\bullet}\right]=\left[\left\{(\mathrm{OH})_{\mathrm{O}}^{\bullet}-\mathrm{V}_{\mathrm{Me}}^{//}\right\}^{/}\right] \qquad [14]$$

and

$$\left[\mathrm{Fe}_{\mathrm{Me}}^{\bullet}\right]=\left[\left\{(\mathrm{OH})_{\mathrm{O}}^{\bullet}-\mathrm{V}_{\mathrm{Me}}^{//}\right\}^{/}\right] \qquad [15]$$

must also be considered. A summary of the dependencies of the concentrations of various point defects on oxygen fugacity and water fugacity for the system MeO is provided in Table 1 for a range of charge neutrality conditions.

2.18.2.1.2 Kinetics

Diffusion of atoms and ions through crystalline solids takes place by the movement of point defects, namely, vacancies and self-interstitials. That is, ionic diffusion takes place by a vacancy or interstitial mechanism. Here, the discussion focuses on vacancies; a parallel analysis applies for self-interstitials. Since the fraction of vacant sites, X_{V}, on any specific sublattice is small, typically $<10^{-3}$ to $\ll 10^{-3}$, vacancies diffuse orders of magnitude more rapidly than the ions on that sublattice. From the point of view of a vacancy, all of the neighboring sites are available, while from the perspective of an ion, possibly one but more likely no neighboring sites are available at any particular moment. This connection between the movement of ions and that of vacancies leads to the following relationship between the diffusion coefficient for ions, D_{ion}, and that for vacancies, D_{V}:

$$X_{\mathrm{ion}}D_{\mathrm{ion}}=X_{\mathrm{V}}D_{\mathrm{V}} \qquad [16a]$$

where X_{ion} is the fraction of sites on a given sublattice occupied by the ions associated with that sublattice. Since $X_{\mathrm{ion}}=(1-X_{\mathrm{V}})\approx 1$, eqn [16a] is usually approximated as

$$D_{\mathrm{ion}}\approx X_{\mathrm{V}}D_{\mathrm{V}} \qquad [16b]$$

consequently,

$$D_{\mathrm{ion}}\ll D_{\mathrm{V}} \qquad [16c]$$

that is, vacancies diffuse orders of magnitude faster than ions because $X_{\mathrm{V}}\ll 1$.

One consequence of the rapid diffusion of vacancies (as well as of electron holes) is that equilibrium concentrations of vacancies are attained relatively rapidly in response to changes in oxygen partial pressure or oxide activity, typically in much less than an hour under laboratory conditions for which diffusion distances are on the scale of the sample size (Dieckmann and Schmalzried, 1986; Mackwell et al., 1988; Ricoult and Kohlstedt, 1985; Schmalzried, 1981, pp. 93–100; Schmalzried, 1995, pp. 117–123; Wanamaker, 1994; Yurek and Schmalzried, 1974). Point defect concentrations respond even more quickly to changes in temperature and pressure for which the appropriate diffusion length is the distance between the sites of repeatable growth, which serve as sources and sinks for point defects (Schmalzried, 1981, pp. 93–96; Schmalzried, 1995, pp. 10–12).

The concentration of vacancies in a mineral will differ from one sublattice to the next. In a system composed of Me = (Mg, Fe), Si, and O, the concentration of vacancies on the Me sublattice is generally several orders of magnitude larger than the concentrations on the Si and O sublattices, that is, $[\mathrm{V}_{\mathrm{Me}}^{//}]>>[\mathrm{V}_{\mathrm{O}}^{\bullet\bullet}], [\mathrm{V}_{\mathrm{Si}}^{////}]$ (e.g., Nakamura and Schmalzried, 1983, 1984; Tsai and Dieckmann, 2002). As a result, $D_{\mathrm{Me}}\gg D_{\mathrm{O}}, D_{\mathrm{Si}}$.

For deformation by diffusion creep or dislocation climb processes, the flux of ions directly enters expressions for the strain rate. The deformation rate is calculated from analyses of the flux of ions between regions experiencing different stress states, such as between grain boundaries in a rock that are oriented normal to and those that are oriented parallel to the maximum principal stress. In an ionic solid, the fluxes of all of the constituent ions must be coupled in order to maintain stoichiometry (Dimos et al., 1988; Gordon, 1973; Jaoul, 1990; Ruoff, 1965; Ready, 1966; Schmalzried, 1995, pp. 345–346). As a consequence, the creep rate of a monomineral rock is controlled by the rate of diffusion of the slowest-diffusing ion.

In the case of olivine, $\mathrm{Me_2SiO_4}$, for diffusion along parallel paths (i.e., one-dimensional diffusion), the fluxes of Me^{2+}, Si^{4+}, and O^{2-} are given by (e.g., Schmalzried, 1981, p. 63; Schmalzried, 1995, pp. 78–82)

$$\begin{aligned} j_{\mathrm{Me}^{2+}} &= -\frac{D_{\mathrm{Me}}C_{\mathrm{Me}}}{RT}\frac{\partial \eta_{\mathrm{Me}^{2+}}}{\partial \xi} \\ &= -\frac{D_{\mathrm{Me}}C_{\mathrm{Me}}}{RT}\left(\frac{\partial \mu_{\mathrm{Me}^{2+}}}{\partial \xi}+2F\frac{\partial \varphi}{\partial \xi}\right) \end{aligned} \qquad [17a]$$

$$j_{\mathrm{Si}^{4+}}=-\frac{D_{\mathrm{Si}}C_{\mathrm{Si}}}{RT}\frac{\partial \eta_{\mathrm{Si}^{4+}}}{\partial \xi}=-\frac{D_{\mathrm{Si}}C_{\mathrm{Si}}}{RT}\left(\frac{\partial \mu_{\mathrm{Si}^{4+}}}{\partial \xi}+4F\frac{\partial \varphi}{\partial \xi}\right) \qquad [17b]$$

and

$$j_{\mathrm{O}^{2-}}=-\frac{D_{\mathrm{O}}C_{\mathrm{O}}}{RT}\frac{\partial \eta_{\mathrm{O}^{2-}}}{\partial \xi}=-\frac{D_{\mathrm{O}}C_{\mathrm{O}}}{RT}\left(\frac{\partial \mu_{\mathrm{O}^{2-}}}{\partial \xi}-2F\frac{\partial \varphi}{\partial \xi}\right) \qquad [17c]$$

where j is the flux, D the self-diffusivity, C the concentration, and η the electrochemical potential of the appropriate ionic species. In eqn [17], ξ is a spatial variable. The electrochemical

Table 1 Dependence of point defect concentrations on oxygen fugacity and water fugacity, expressed as the exponents p and q in the relationship $[\,]\propto f_{\mathrm{O_2}}^{p}f_{\mathrm{H_2O}}^{q}$, for several charge neutrality conditions for MeO

Charge neutrality	$Me_{Me}^{\bullet}$	$V_{Me}^{//}$	$V_{O}^{\bullet\bullet}$	$\{Me_{Me}^{\bullet}-V_{Me}^{//}\}^{/}$	$(OH)_{O}^{\bullet}$	$\{(OH)_{O}^{\bullet}-V_{Me}^{//}\}^{/}$
$[\mathrm{Me}_{\mathrm{Me}}^{\bullet}]=2[\mathrm{V}_{\mathrm{Me}}^{//}]$	1/6, 0	1/6, 0	−1/6, 0	1/3, 0	−1/12, 1/2	1/12, 1/2
$[(\mathrm{OH})_{\mathrm{O}}^{\bullet}]=2[\mathrm{V}_{\mathrm{Me}}^{//}]$	1/4, −1/6	0, 1/3	0, −1/3	1/4, 1/6	0, 1/3	0, 2/3
$[\mathrm{Me}_{\mathrm{Me}}^{\bullet}]=[\{(\mathrm{OH})_{\mathrm{O}}^{\bullet}-\mathrm{V}_{\mathrm{Me}}^{//}\}^{/}]$	1/8, 1/4	1/4, −1/2	−1/4, 1/2	3/8, −1/4	−1/8, 3/4	1/8, 1/4
$[(\mathrm{OH})_{\mathrm{O}}^{\bullet}]=[\{(\mathrm{OH})_{\mathrm{O}}^{\bullet}-\mathrm{V}_{\mathrm{Me}}^{//}\}^{/}]$	1/4, 0	0, 0	0, 0	1/4, 0	0, 1/2	0, 1/2

potentials for the various ions are written in terms of the chemical potential, μ, and the electric potential, φ, as (e.g., Schmalzried, 1981, p. 63)

$$\eta = \mu + zF\varphi \qquad [18]$$

where z is the charge on the ion and F is the Faraday constant. To maintain stoichiometry during diffusion-controlled creep in which transport of entire lattice molecules must occur between sites of repeatable growth such as dislocations and grain boundaries, the flux coupling condition is

$$\frac{j_{\mathrm{Me}^{2+}}}{C_{\mathrm{Me}}} = \frac{j_{\mathrm{Si}^{4+}}}{C_{\mathrm{Si}}} = \frac{j_{\mathrm{O}^{2-}}}{C_{\mathrm{O}}} \qquad [19a]$$

Equation [19a] applies specifically to the case in which all of the ions diffuse along a single path or parallel paths; the more general case in which diffusion occurs along multiple paths (e.g., along grain boundaries and through grain interiors) is treated in Dimos et al. (1988; see also Kohlstedt, 2006).

The flux coupling equation provides a means of eliminating the $\partial\varphi/\partial\xi$ term from the flux equations. The flux coupling condition for olivine in eqn [19a] can be rewritten as

$$2j_{\mathrm{Me}^{2+}} = 4j_{\mathrm{Si}^{4+}} = j_{\mathrm{O}^{2-}} \qquad [19b]$$

Then, since $D_{\mathrm{Me}} \gg D_{\mathrm{O}} > D_{\mathrm{Si}}$, the approximation

$$\frac{\partial\eta_{\mathrm{Me}^{2+}}}{\partial\xi} = \frac{\partial\mu_{\mathrm{Me}^{2+}}}{\partial\xi} + 2F\frac{\partial\varphi}{\partial\xi} \approx 0 \qquad [20a]$$

that is

$$2F\frac{\partial\varphi}{\partial\xi} \approx -\frac{\partial\mu_{\mathrm{Me}^{2+}}}{\partial\xi} \qquad [20b]$$

must hold in order to satisfy eqn [19b]. Using the implicit assumption of local thermodynamic equilibrium, the chemical potentials of the ions can be written in terms of the chemical potentials of the oxides as

$$\mu_{\mathrm{Me}^{2+}} + \mu_{\mathrm{O}^{2-}} = \mu_{\mathrm{MeO}} \qquad [21a]$$

and

$$\mu_{\mathrm{Si}^{4+}} + 2\mu_{\mathrm{O}^{2-}} = \mu_{\mathrm{SiO}_2} \qquad [21b]$$

Combining eqn [19b] with eqns [17a], [17b], [20b], [21a], and [21b], leads to the relation

$$D_{\mathrm{Si}}\frac{\partial\mu_{\mathrm{SiO}_2}}{\partial\xi} = (D_{\mathrm{O}} + 2D_{\mathrm{Si}})\frac{\partial\mu_{\mathrm{MeO}}}{\partial\xi} \qquad [22]$$

Also, the flux of Si^{4+}, the slowest ionic species, becomes

$$j_{\mathrm{Si}^{4+}} = -\frac{C_{\mathrm{Si}}D_{\mathrm{Si}}}{RT}\left(\frac{\partial\mu_{\mathrm{SiO}_2}}{\partial\xi} - 2\frac{\partial\mu_{\mathrm{MeO}}}{\partial\xi}\right) \qquad [23a]$$

Since the chemical potential of olivine is

$$\mu_{\mathrm{Me_2SiO_4}} = 2\mu_{\mathrm{MeO}} + \mu_{\mathrm{SiO}_2} \qquad [24]$$

the flux of Si^{4+} can be rewritten as

$$j_{\mathrm{Si}^{4+}} = -\frac{C_{\mathrm{Si}}D_{\mathrm{Si}}}{RT}\frac{D_{\mathrm{O}}}{D_{\mathrm{O}} + 4D_{\mathrm{Si}}}\frac{\partial\mu_{\mathrm{Me_2SiO_4}}}{\partial\xi} \qquad [23b]$$

The chemical potential of olivine contains an activity, a, term and a stress, σ, term such that

$$\frac{\partial\mu_{\mathrm{Me_2SiO_4}}}{\partial\xi} = RT\frac{\partial\ln a_{\mathrm{Me_2SiO_4}}}{\partial\xi} - V_{\mathrm{Me_2SiO_4}}\frac{\partial\sigma}{\partial\xi} \qquad [25a]$$

where $V_{\mathrm{Me_2SiO_4}}$ is the molar volume of olivine (e.g., Dimos et al., 1988; Gordon, 1973; Ready, 1966; Schmalzried, 1995, p. 334). The first term on the right-hand side of eqn [25a] can be expressed in terms of the gradient in the concentration of vacancies on the Me sublattice (Dimos et al., 1988; Jaoul, 1990; Kohlstedt, 2006) as

$$RT\frac{\partial\ln a_{\mathrm{Me_2SiO_4}}}{\partial\xi} \approx -2RT\frac{\partial\left[\mathrm{V}_{\mathrm{Me}}^{//}\right]}{\partial\xi} \approx -2\left[\left(\mathrm{V}_{\mathrm{Me}}^{//}\right)^{\mathrm{o}}\right]V_{\mathrm{Me_2SiO_4}}\frac{\partial\sigma}{\partial\xi} \qquad [26]$$

where $[(\mathrm{V}_{\mathrm{Me}}^{//})^{\mathrm{o}}]$ is the concentration of Me vacancies under hydrostatic stress conditions. The gradient in the concentration in metal vacancies results from the gradient in normal stress between sources for vacancies (regions of minimum compressive stress) and sinks for vacancies (regions of maximum compressive stress). Since $[(\mathrm{V}_{\mathrm{Me}}^{//})^{\mathrm{o}}]$ is small, $<10^{-3}$, the second term in eqn [25a] dominates such that

$$\frac{\partial\mu_{\mathrm{Me_2SiO_4}}}{\partial\xi} \approx -V_{\mathrm{Me_2SiO_4}}\frac{\partial\sigma}{\partial\xi} \qquad [25b]$$

Therefore,

$$j_{\mathrm{Si}^{4+}} = \frac{C_{\mathrm{Si}}D_{\mathrm{Si}}}{RT}\frac{D_{\mathrm{O}}}{D_{\mathrm{O}} + 4D_{\mathrm{Si}}}V_{\mathrm{Me_2SiO_4}}\frac{\partial\sigma}{\partial\xi} \qquad [27a]$$

and if $D_{\mathrm{O}} \gg D_{\mathrm{Si}}$,

$$j_{\mathrm{Si}^{4+}} = \frac{C_{\mathrm{Si}}D_{\mathrm{Si}}}{RT}V_{\mathrm{Me_2SiO_4}}\frac{\partial\sigma}{\partial\xi} \qquad [27b]$$

2.18.2.2 Line Defects: Structure and Dynamics

Dislocations are line defects that separate regions of a crystal that have slipped from those that have not slipped. Their motion by glide and climb is central to the deformation of most crystalline solids, much like point defects are essential for diffusion. Unlike point defects, dislocations are not equilibrium defects. While the change in enthalpy associated with the formation of a dislocation is quite large, the change in entropy is relatively small. In a simplistic analogy, the former might be considered equal to the change in enthalpy due to the formation of N vacancies, where the vacancies form a row of the same length as the dislocation line. In contrast, the change in entropy resulting from the formation of N vacancies constrained to lie along a line will be significantly less than that associated with the formation of N vacancies randomly distributed in a crystal. The result is that, at equilibrium, a crystal is expected to be dislocation-free (Devereux, 1983, pp. 368–372).

A dislocation is characterized by two vector quantities: its line direction, $\boldsymbol{\mathcal{L}}$, which defines the direction of the dislocation at each point along its length, and a displacement or Burgers vector, $\boldsymbol{b}$, which defines the displacement of the lattice produced as the dislocation moves through a crystal. For a dislocation loop such as that illustrated in **Figure 1**, the tangential line direction changes from one point to the next along the loop, while the Burgers vector is the same at every point. Regions along the dislocation loop for which $\boldsymbol{b}$ is perpendicular to $\mathcal{L}$ are termed edge segments, while regions for which $\boldsymbol{b}$ is parallel to $\mathcal{L}$ are termed screw segments. Regions of a dislocation for which $\boldsymbol{b}$ and $\mathcal{L}$ are neither perpendicular nor parallel are referred to as mixed segments.

Movement of a dislocation can take place by glide and climb. An edge dislocation can move in one of two ways. If an edge dislocation moves in the glide plane defined by $\boldsymbol{b} \times \mathcal{L}$, its motion is conservative. In contrast, if an edge dislocation moves normal to its glide plane, the process is nonconservative in that lattice molecules are added to or taken away from the dislocation line by diffusion such that the dislocation climbs out of its glide plane. A screw dislocation does not have a specific glide plane since $\boldsymbol{b}$ and $\mathcal{L}$ are parallel to each other. Hence, a screw dislocation generally glides on the plane that offers least resistance to its motion. If it encounters an obstacle to its movement, a screw dislocation can cross slip off of its original glide plane onto a parallel glide plane in order to continue moving. A dislocation must always move in a direction perpendicular to its line direction. The displacement resulting from glide of an edge dislocation is thus parallel to the direction of dislocation glide, while the displacement resulting from movement of a screw dislocation is perpendicular to its direction of motion defined by the velocity vector, $\mathcal{V}$, as illustrated in **Figure 2**. Finally, a slip system is defined for a dislocation by the combination of a unit vector normal to the slip plane, $\boldsymbol{n}$, and $\boldsymbol{b}$. As an example, important slip systems in clinopyroxene include $\{110\}\langle 1\bar{1}0\rangle$, $\{110\}[001]$, and $(100)[001]$ (Bystricky and Mackwell, 2001). Slip systems in olivine include $(010)[100]$, $(001)[100]$, $(100)[001]$, and $(010)[001]$ with the dominate slip system determined by stress, and water concentration as well as pressure and temperature (Carter and Avé Lallemant, 1970; Castelnau et al., 2010; Durinck et al., 2005; Jung and Karato, 2001; Mainprice et al., 2005; Raterron et al., 2012).

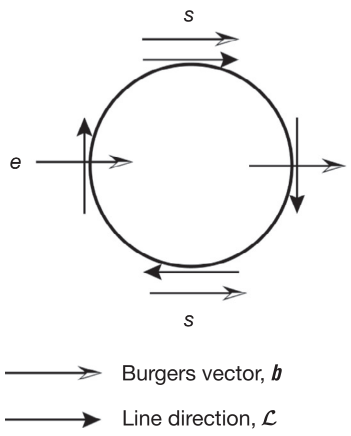

Figure 1 Sketch of dislocation loop indicating the directions of the Burgers vector, $\boldsymbol{b}$, and of the dislocation line, $\mathcal{L}$, at four points along the loop. The edge and screw segments of the dislocation loop are denoted by *e* and *s*, respectively.

To the first order, dislocations with short displacement vectors are preferred over those with longer displacement vectors since the energy per unit length of a dislocation, E_{disl}, is proportional to the square of the Burgers vector. For an edge dislocation in an elastically isotropic material (Weertman and Weertman, 1992, pp. 45–52),

$$E_{\text{disl}} = \frac{Gb^2}{4\pi(1-\nu)} \ln \frac{r}{r_c} \qquad [28]$$

where G is the shear modulus, r is the mean spacing between dislocations, and r_c is the radius of the dislocation core. In eqn [28], the contribution of the core of the dislocation to the elastic strain energy has been neglected. For elastically anisotropic materials, the full matrix of elastic constants must be considered, as discussed in detail by Hirth and Lothe (1968, pp. 398–440).

Slip generally occurs on the closest packed plane that contains $\boldsymbol{b}$, that is, the most widely separated planes and thus, in general, the most weakly bonded planes. In olivine, $|[100]| < |[001]| < |[010]|$ suggesting that $\boldsymbol{b} = [100]$ should dominate. However, plastic deformation of a polycrystalline material cannot proceed without opening up void space if only one or two independent slip systems operate. Homogeneous plastic deformation of a rock requires dislocation glide on five independent slip systems, a condition known as the von Mises criterion (von Mises, 1928), or glide and climb on three independent slip systems (Groves and Kelly, 1969). Plastic deformation can occur without fracture with glide on four independent slip systems if deformation is allowed to be heterogeneous (Hutchinson, 1976). Processes such as grain-boundary sliding, ionic diffusion, and twinning can also relax the von Mises criterion.

Glide and climb of dislocations involve steps along the dislocation line: steps that lie in the glide plane, called kinks, facilitate glide and steps that are out of the glide plane, called jogs, and facilitate climb.

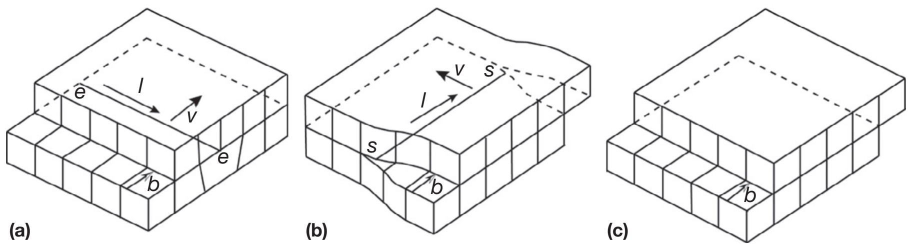

Figure 2 Sketch illustrating that (a) the movement of an edge dislocation, *e*, and (b) the movement of a screw dislocation, *s*, with the same Burgers vector (c) produce the same displacement of the upper half of a crystal relative to the lower half. Modified from Kelly A and Groves GW (1970) *Crystallography and Crystal Defects*. Addison-Wesley Publishing Company, p. 199.

Dislocations interact with one another and with an applied stress field through the stress field that arises due to the elastic distortion caused by the presence of each dislocation. The stress fields associated with edge and screw dislocations in elastically isotropic and elastically anisotropic media are derived in Hirth and Lothe (1968, pp. 398–440) and in Weertman and Weertman (1992, pp. 22–41). The force on a dislocation is then calculated using the Peach–Koehler equation (Peach and Koehler, 1950). In its simplest form, the force per unit length, f, on a dislocation is

$$f = \sigma b \qquad [29]$$

where the stress σ arises, for example, from a neighboring dislocation or an external force.

2.18.2.3 Planar Defects: Structure and Energy

Planar defects include twin boundaries, stacking faults, grain boundaries, and interphase boundaries. The emphasis in this chapter is on grain boundaries and interphase boundaries, because of the important role of these two types of interfaces in plastic deformation.

If the misorientation across a grain boundary is not too large, say $<15°$ (i.e., a low-angle boundary), the interface can be constructed from a periodic array of dislocations. A low-angle tilt boundary consists of a series of parallel edge dislocation, as illustrated schematically in **Figure 3** and imaged in **Figure 4**. In the case of a low-angle tilt boundary, the spacing between dislocations, h, can be expressed in terms of the misorientation angle, ϑ, across the boundary as

$$h = \frac{b}{2\sin(\vartheta/2)} \qquad [30a]$$

For a small misorientation, the misorientation angle can be approximated by

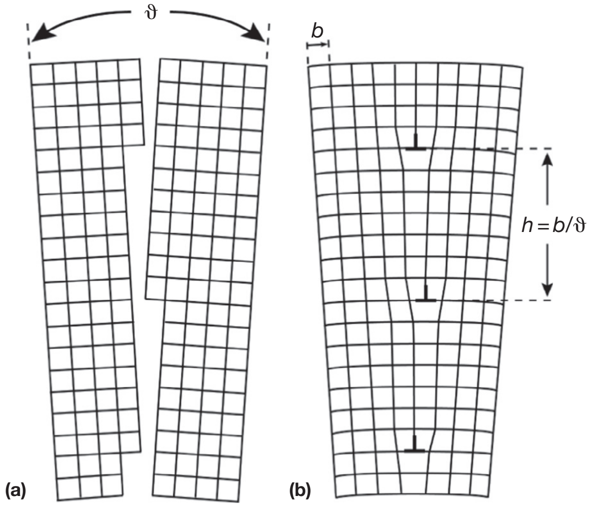

Figure 3 Sketch of a low-angle tilt boundary formed by a series of periodically spaced edge dislocations, which are denoted by the inverted 'T' symbols. Modified from Read Jr WT (1953) Dislocations in Crystals. McGraw-Hill Book Company, New York, p. 157.

$$\vartheta \approx \frac{b}{h} \qquad [30b]$$

Starting with eqn [28], the elastic strain energy per unit area of a low-angle tilt boundary can then be derived as (Read and Shockley, 1950)

$$E_{\text{tilt}} = \frac{Gb^2}{4\pi(1-\nu)}\frac{\vartheta}{b}(A - \ln\vartheta) \qquad [31]$$

where parameter A accounts for the fraction of the elastic strain energy associated with the cores of the dislocations. Once the cores of the dislocations in a tilt boundary begin to overlap, this simple description of a grain boundary breaks down.

A low-angle twist boundary requires two, generally orthogonal, sets of screw dislocations. The elastic energy per unit area for a low-angle twist boundary is similar to that for a low-angle tilt boundary. A sketch of the atomic structure of a low-angle twist boundary formed by rotating the lattices of two grains relative to each through an angle ϑ, thus forming orthogonal sets of dislocations, is presented in **Figure 5**. A transmission electron micrograph of a twist boundary is shown in **Figure 6**.

As illustrated in **Figure 7**, grain-boundary energy increases rapidly with increasing ϑ, as described by eqn [31], up to $\vartheta \approx 20°$. At larger values of ϑ, grain-boundary energy is approximately constant except for a few minima that occur at specific orientations. Other than twin boundaries, these minima occur at orientations for which a significant fraction of the lattice points in the two neighboring grains are nearly coincident (Chan and Balluffi, 1985, 1986). A simple example of this coincidence structure illustrating the type of periodicity that can be present in specific grain boundaries is shown in **Figure 8** for a twist boundary.

Grain and interphase boundaries influence the physical properties of rocks in several important ways. First, grain-boundary sliding provides a mechanism for producing strain in response to an applied differential stress. Grain-boundary sliding takes place by the movement of grain-boundary dislocations. As discussed in the next section, grain-boundary sliding is an essential part of diffusion creep (Raj and Ashby, 1971). Grain-boundary sliding can also be important during deformation in which dislocation glide and dislocation climb operate (e.g., Langdon, 1994). In this case, lattice dislocations

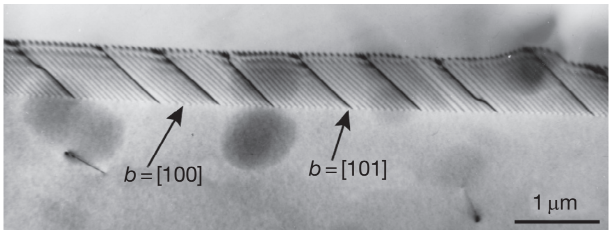

Figure 4 Bright-field transmission electron micrograph of a low-angle tilt boundary in olivine. Two sets of dislocations, one with $\boldsymbol{b} = [100]$ and the other with $\boldsymbol{b} = [101]$, are present in this boundary. The darker $\boldsymbol{b} = [101]$ dislocations are more widely spaced than the lighter, periodically spaced $\boldsymbol{b} = [100]$ dislocations. This image was taken with the diffraction condition $\boldsymbol{g} = (002)$; hence, the $\boldsymbol{b} = [100]$ dislocations exhibit only residual contrast. Modified from Goetze C and Kohlstedt DL (1973) Laboratory study of dislocation climb and diffusion in olivine. *Journal of Geophysical Research* 78: 5961–5971.

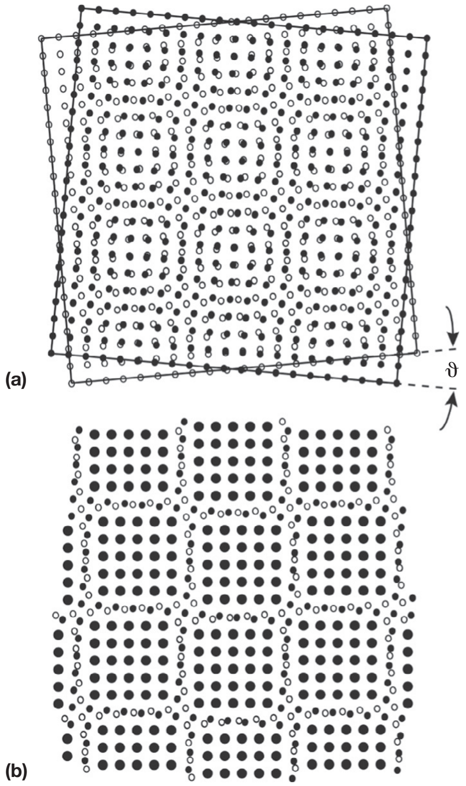

Figure 5 Sketch of atomic configuration for a [001] low-angle twist boundary in a simple cubic lattice with the boundary parallel to the plane of the figure. In this example, $\vartheta \approx 10°$. (a) In the unrelaxed atomic configuration, the open circles represent atoms in the plane just above the boundary, while the closed circles represent the atoms in the plane just below the boundary. (b) In the relaxed atomic configuration, the grains join in regions in which the atomic match is good with two orthogonal sets of screw dislocations located between these regions. Modified from Schmalzried H (1995) *Chemical Kinetics of Solids*. VCH Publishers, New York, p. 51.

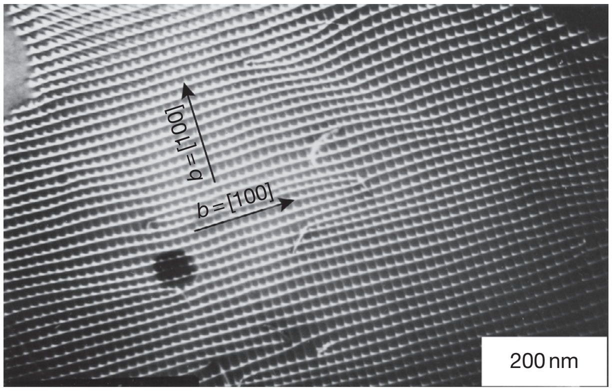

Figure 6 Dark-field transmission electron micrograph of two orthogonal sets of screw dislocations, one with ***b*** = [100] and the other with ***b*** = [001], forming a low-angle twist boundary in the (010) plane of olivine. The boundary is very nearly parallel to the plane of the figure. Modified from Ricoult DL and Kohlstedt DL (1983a) Structural width of low-angle grain boundaries in olivine. *Physics and Chemistry of Minerals*, 9: 133–138; see also Ricoult and Kohlstedt (1983b).

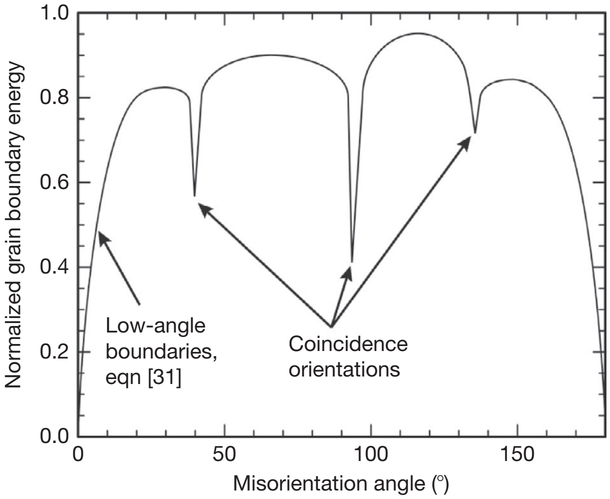

Figure 7 Sketch of normalized grain-boundary energy versus misorientation angle illustrating the energy minima that arise when the two neighboring grains are oriented such that a significant fraction of lattice sites are coincident, such as illustrated in Figure 8.

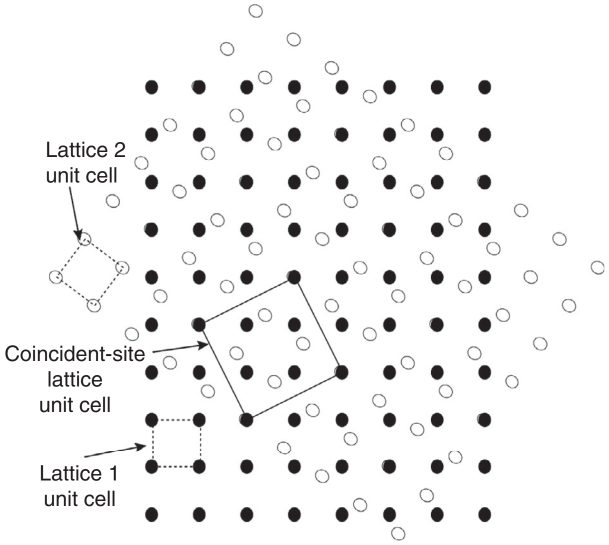

Figure 8 Sketch of lattice sites in two simple cubic grains that have been rotated relative to each other by ~53°. At this orientation, a fraction of the lattice sites from the two grains coincide forming a coincident-site lattice with a unit cell that is larger than those of the two adjoining grains. Open circles represent atoms in the plane just above the boundary, while the closed circles represent the atoms in the plane just below the boundary.

can dissociate and enter grain boundaries resulting in enhanced or stimulated grain-boundary sliding (Pshenichnyuk et al., 1998). As discussed later in the text, grain-boundary sliding often provides an additional mechanism of deformation and can be particularly important in rocks composed of minerals with fewer than five independent slip systems.

Second, grain boundaries migrate in response to a difference in dislocation density between neighboring grains. As expressed in eqn [28], each dislocation introduces elastic strain energy into a crystalline grain. If during deformation the dislocation density becomes higher in one grain than in the next grain, a thermodynamic driving force exists that can cause the grain boundary to migrate toward the region of higher dislocation density, absorbing lattice dislocations into the grain boundary, thus reducing the stored elastic strain energy. The dislocation-free region left in the wake of the migrating boundary will deform more easily than neighboring areas in which glide is slowed by dislocation–dislocation interactions.

Third, grain boundaries are short-circuit paths for diffusion. The rate of diffusion along a grain boundary is in general several orders of magnitude faster than through a grain interior (Shewmon, 1983, pp. 164–175). Thus, even though the cross-sectional area of a grain boundary is small relative to that of the grain itself, the flux of ions passing through a grain boundary can be significant. The result is that, in the diffusion creep regime, grain-boundary diffusion is often the primary mechanism for deformation. It should also be noted that grain boundaries provide storage sites for elements that, due to size or charge, are incompatible in the grain interior (Hiraga and Kohlstedt, 2007; Hiraga et al., 2003, 2004, 2007). The presence of incompatible elements at grain and interphase boundaries perturbs the structure and the local charge state of the boundary, which in turn can affect diffusion kinetics (Mishin and Herzig, 1999).

2.18.3 Mechanisms of Deformation and Constitutive Equations

The mechanism of deformation that dominates the plastic deformation of a rock depends both on the properties of the rock such as grain size, d, and phase content, Φ, and on the thermodynamic parameters such as temperature, pressure, P, water fugacity, $f_{\mathrm{H_2O}}$, and component (oxide) activity, a_{ox}. The dependence of strain rate, $\dot{\varepsilon}$, on these quantities can be expressed in a general constitutive equation or flow law as

$$\dot{\varepsilon} = \dot{\varepsilon}(d, \Phi, T, P, f_{\mathrm{H_2O}}, a_{\mathrm{ox}}, \ldots) \qquad [32]$$

Diffusion-controlled creep tends to be important at lower differential stresses in finer-grained rocks. In contrast, dislocation-dominated processes govern flow at higher stresses in coarser-grained rocks. In this section, some of the constitutive equations used to describe flow in the diffusion and dislocation deformation regimes are first introduced. Then, the influence on rheological behavior of two important fluids, water and melt, is discussed. Finally, the development of crystallographic fabrics and their resulting effect on deformation are presented.

2.18.3.1 Constitutive Equations

2.18.3.1.1 Diffusion creep

Diffusion creep can be divided into two regimes, one in which diffusion through the interiors of grains controls the rate of deformation (Herring, 1950; Nabarro, 1948) and the other in which diffusion along grain boundaries governs the rate of deformation (Coble, 1963). The relative importance of these two mechanisms depends primarily on grain size and temperature.

2.18.3.1.1.1 Grain matrix diffusion

The rate of deformation in the Nabarro–Herring creep regime in which diffusion through grain interiors limits the rate of creep is described by the relation (Herring, 1950; Nabarro, 1948)

$$\dot{\varepsilon}_{\mathrm{NH}} = \alpha_{\mathrm{NH}} \frac{\sigma V_{\mathrm{m}}}{RT} \frac{D_{\mathrm{gm}}}{d^2} \qquad [33]$$

where α_{NH} is a geometric term and D_{gm} is the diffusion coefficient for the slowest species diffusing through the grain matrix (gm), that is, the grain interior. Important points to note are that strain rate is linearly proportional to the differential stress, inversely proportional to the square of the grain size, and exponentially dependent on temperature and pressure through the diffusion coefficient since

$$D_{\mathrm{gm}} = D^{\mathrm{o}}_{\mathrm{gm}} \exp\left(-\frac{\Delta E_{\mathrm{gm}} + P\Delta V_{\mathrm{gm}}}{RT}\right) = D^{\mathrm{o}}_{\mathrm{gm}} \exp\left(-\frac{\Delta H_{\mathrm{gm}}}{RT}\right) \qquad [34]$$

where $D^{\mathrm{o}}_{\mathrm{gm}}$ is a function of the lattice vibration frequency, jump distance, and entropies for formation and migration of vacancies (assuming a vacancy diffusion mechanism) (Shewmon, 1983, pp. 61–62). ΔE_{gm}, ΔV_{gm}, and ΔH_{gm} are the activation energy, activation volume, and activation enthalpy for grain matrix diffusion, respectively; if ionic diffusion occurs via a vacancy mechanism, then each of these three terms is composed of the sum of a contribution for vacancy formation and a contribution for vacancy migration.

2.18.3.1.1.2 Grain-boundary diffusion

A similar expression applies in the Coble creep regime in which the creep rate is limited by diffusion through grain boundaries (Coble, 1963):

$$\dot{\varepsilon}_{\mathrm{C}} = \alpha_{\mathrm{C}} \frac{\sigma V_{\mathrm{m}}}{RT} \frac{\delta D_{\mathrm{gb}}}{d^3} \qquad [35]$$

where α_{C} is a geometric term; δ is the diffusion width of the grain boundary, which is approximately equal to the structural width of $\sim$1 nm (e.g., Atkinson, 1985; Carter and Sass, 1981; Ricoult and Kohlstedt, 1983a,b); and D_{gb} is the diffusion coefficient for the slowest species diffusing along grain boundaries. The grain-boundary diffusivity can be expressed as

$$D_{\mathrm{gb}} = D^{\mathrm{o}}_{\mathrm{gb}} \exp\left(-\frac{\Delta E_{\mathrm{gb}} + P\Delta V_{\mathrm{gb}}}{RT}\right) = D^{\mathrm{o}}_{\mathrm{gb}} \exp\left(-\frac{\Delta H_{\mathrm{gb}}}{RT}\right) \qquad [36]$$

where $D^{\mathrm{o}}_{\mathrm{gb}}$ is similar in nature to $D^{\mathrm{o}}_{\mathrm{gm}}$ in eqn [34] (Schmalzried, 1995, pp. 240–241) and ΔE_{gb}, ΔV_{gb}, and ΔH_{gb} are the activation energy, activation volume, and activation enthalpy for grain-boundary diffusion, respectively. Again, the strain rate increases linearly with increasing differential stress and increases exponentially with inverse temperature while decreasing exponentially with increasing pressure. However, in contrast to the Nabarro–Herring case, strain rate for Coble creep varies inversely as the cube, rather than the square, of the grain size.

Comparison of eqns [33] with [35] reveals the following points: (i) Both creep mechanisms give rise to Newtonian viscous behavior ($\dot{\varepsilon} \propto \sigma^1$) with viscosity, $\eta \equiv \sigma/\dot{\varepsilon}$, independent of stress. (ii) As long as the grain size is small enough that diffusion creep dominates over dislocation creep, Nabarro–Herring creep ($\dot{\varepsilon} \propto 1/d^2$) is more important than Coble creep ($\dot{\varepsilon} \propto 1/d^3$) at larger grain sizes. (iii) Nabarro–Herring creep dominates at higher temperatures and Coble creep at lower temperatures because $\Delta H_{\mathrm{gb}} < \Delta H_{\mathrm{gm}}$.

The analyses of Nabarro (1948) and Herring (1950) and of Coble (1963) strictly apply to the deformation of a single spherical grain. Subsequent analyses pointed out the necessity of grain-boundary sliding in diffusion creep of polycrystalline materials (Liftshitz, 1963; Raj and Ashby, 1971). The fact that grains tend to be equiaxed in samples deformed in the diffusion creep field indicates that grain-boundary sliding and grain rotation are crucial. The creep process is essentially that of grain-boundary sliding accommodated by diffusion both through grain interiors and along grain boundaries, if grain boundaries are too weak to support shear stress. For this case, $\alpha_{\mathrm{NH}} = 14$ and $\alpha_{\mathrm{C}} = 14\pi$. Since grain boundary and grain matrix diffusion are independent/parallel processes, eqns [33] and [35] can be combined to give

$$\dot{\varepsilon}_{\mathrm{diff}} = 14\left(\frac{\sigma V_{\mathrm{m}}}{RT}\right)\left(D_{\mathrm{gm}} + \frac{\pi\delta D_{\mathrm{gb}}}{d}\right)\left(\frac{1}{d^2}\right) \qquad [37]$$

In general, this deformation mechanism is referred to simply as diffusion creep. In multicomponent minerals, the rate of diffusion creep is controlled by the slowest species diffusing along its fastest path (grain boundary or grain interior).

2.18.3.1.2 Deformation involving dislocations

As differential stress and/or grain size increases, a transition occurs from diffusion creep to dislocation-dominated deformation. One estimate of the stress required to move from the diffusion creep regime to the dislocation creep regime is based on a calculation of the stress required to operate a Frank–Reed dislocation source, σ_{FR} (Frank and Read, 1950), and thus generate the dislocations necessary to sustain deformation:

$$\sigma_{\mathrm{FR}} \approx \frac{2Gb}{L} \qquad [38]$$

where L is the length of the dislocation segment operating as the source of new dislocations. If the length of a dislocation line is limited by the grain size, then for $G = 70$ GPa, $b = 0.5$ nm, and $L = d = 10$ μm, $\sigma_{\mathrm{FR}} \approx 7$ MPa.

The strain produced by a single dislocation moving across a grain is very small, thus many dislocations must be generated and move to accomplish a significant amount of deformation. The strain, ε, produced in a cubic grain of dimension d by one dislocation moving through the grain is

$$\varepsilon = \frac{b}{d} \qquad [39]$$

Thus, if $d = 1$ mm, $\varepsilon \approx 5 \times 10^{-7}$. Greater strain is achieved by moving a large number of dislocations through the grain. The density of dislocations, ρ, which scales with the magnitude of the applied differential stress, is often written as (Karato, 2008, p. 160; Poirier, 1985, p. 109; Takeuchi and Argon, 1976; Weertman, 1999)

$$\rho \approx \left(\frac{\sigma}{Gb}\right)^2 \qquad [40]$$

such that, for olivine, $\rho \approx 10^9$ m^{-2} for a differential stress of 1 MPa. The strain produced by this density of dislocations moving a distance x is

$$\varepsilon = \rho b x \qquad [41]$$

For $x = d$, $\varepsilon \approx 5 \times 10^{-4}$, which is still a small value. To produce geologically significant strains, dislocations must be generated, be moved through crystalline grains, and then be removed so that new dislocations can be generated to maintain an approximately constant (steady-state) density of dislocations and keep the deformation process going. If steady-state deformation is attained, then a balance must be achieved, and one step in this series of steps will limit the rate of deformation.

A number of models have been proposed to describe the rate of deformation in terms of applied stress, temperature, pressure, and other thermodynamic and structural variables (e.g., Evans and Kohlstedt, 1995; Poirier, 1985, pp. 94–144). In this chapter, characteristic elements of these models are reviewed in order to provide a framework for examining laboratory-determined deformation data and extrapolating to geologic conditions.

The dependence of the strain rate on differential stress for deformation accomplished by dislocation processes can be examined through the Orowan equation, which is obtained by differentiating eqn [41] with respect to time and noting that in steady state, the dislocation density is independent of time, $\partial\rho/\partial t = 0$ (Orowan, 1940; Poirier, 1985, pp. 62–63):

$$\dot{\varepsilon} = \rho b \bar{v} \qquad [42]$$

where $\bar{v}$ is the average dislocation velocity. It should be noted, however, that the $\partial\rho/\partial t$ term is critical in the discussions of transient deformation (e.g., deformation immediately following a change in stress). As discussed in reference to eqn [40], the dislocation density is often taken to be proportional to the square of the stress, such that $\dot{\varepsilon} \propto \rho \propto \sigma^2$. In addition, an additional dependence of strain rate on differential stress enters through the dislocation velocity term.

In this discussion, dislocation creep is divided into three regimes. As with diffusion creep, the main parameters determining the relative importance of the various dislocation creep mechanisms are differential stress, temperature, pressure, and grain size. First, at high temperature (low stress) and relatively large grain size, all of the strain can be accomplished by glide and climb of dislocations. These conditions define the dislocation creep regime. Second, at high temperature but smaller grain size, grain-boundary sliding operates in conjunction with dislocation processes to produce strain. These conditions define a regime in which dislocation processes are accommodated by grain-boundary sliding or grain-boundary sliding is accommodated by dislocation processes, simply referred to here as the grain-boundary sliding regime. Third, at low temperatures (high stresses), deformation takes place by dislocation glide limited by the intrinsic resistance of the lattice. These conditions delineate the low-temperature plasticity regime.

2.18.3.1.2.1 Dislocation creep

To date, by far the majority of analyses of plastic deformation in geologic materials have used a power-law equation to describe experimental results. A general form of this flow law is

$$\dot{\varepsilon} = A\frac{\sigma^n}{d^m} f^p_{\mathrm{O}_2} f^q_{\mathrm{H_2O}} a^r_{\mathrm{ox}} \exp - \frac{Q_{\mathrm{cr}}}{RT} \qquad [43]$$

where A is a material-dependent parameter and Q_{cr} is the activation energy (strictly, enthalpy) for creep. The power-law form of the creep equation arises by considering the roles of dislocation climb and grain-boundary sliding in the deformation process.

The potential importance of dislocation climb as the rate-controlling step of high-temperature, steady-state creep was suggested in the early 1950s by Mott (1951, 1953, 1956). Subsequently, several climb-controlled creep models were developed that relate strain rate to differential stress, temperature, and pressure, the latter two through the self-diffusivity (for reviews, see Cannon and Langdon, 1988; Evans and Kohlstedt, 1995; Poirier, 1985, pp. 94–144; Weertman, 1978, 1999). The rate of climb of edge dislocations depends directly on diffusive fluxes of ions (e.g., Hirth and Lothe, 1968, pp. 506–519; Poirier, 1985, pp. 58–62). The justification for emphasizing the importance of climb in high-temperature ($T > 2/3T_m$, where T_m is the melting temperature) deformation of crystalline materials is the one-to-one correlation between the activation energy for creep and the activation energy for self-diffusion of the slowest ionic species, which has been observed for a large number of metallic and ceramic materials (e.g., Dorn, 1956; Evans and Knowles, 1978; Mukerjee et al., 1969; Sherby and Burke, 1967; Takeuchi and Argon, 1976).

Two climb-based models of dislocation creep merit particular attention because of their pioneering contributions in this area and because they incorporate most of the elements found in subsequent models. Weertman (1955, 1957a, b) developed a flow law for steady-state dislocation creep in which dislocation glide produces most of the strain but dislocation climb controls the stain rate. In this model, a dislocation source generates a dislocation loop that expands by gliding until it encounters an obstacle such as a dislocation loop that was generated on a parallel glide plane. The two dislocations interact to form a dipole that prevents further glide until the two dislocations comprising the dipole climb to annihilate one another. Once the dipole is annihilated, the dislocation sources produce new dislocation loops (i.e., dislocation multiplication) to continue the deformation process. If glide is rapid and climb is slow, then the average dislocation velocity is

$$\bar{v} = \frac{\ell_g + \ell_c}{t_g + t_c} \approx \frac{\ell_g}{\ell_c} v_c \qquad [44]$$

where $\boldsymbol{\mathcal{L}}_g$ is the glide distance, $\boldsymbol{\mathcal{L}}_c$ is the climb distance, and $\mathbf{v}_c$ is the climb velocity (Poirier, 1985, p. 110; Weertman, 1999). The climb velocity, which is determined by diffusion of the slowest atomic/ionic species, is given by the expression (Hirth and Lothe, 1968, pp. 506–519)

$$v_c = 2\pi \frac{\sigma V_m}{RT} \frac{D}{b} \frac{1}{\ln(R_o/r_c)} \qquad [45]$$

where the average spacing between dislocations, R_o, is usually written in terms of the dislocation density as $R_o \approx 1/\sqrt{\rho}$ and the inner cutoff (core) radius, r_c, is generally set at $r_c \approx b$. A flow law is then obtained by inserting eqns [40] and [45] into the Orowan equation, eqn [42], to yield (Weertman, 1999)

$$\dot{\varepsilon} = 2\pi \frac{GV_m}{RT} \left(\frac{\sigma}{G}\right)^3 \frac{D}{b^2} \frac{1}{\ln(G/\sigma)} \frac{\ell_g}{\ell_c} \qquad [46]$$

Nabarro (1967) formulated a model for steady-state dislocation creep based solely on dislocation climb. Bardeen–Herring sources (Bardeen and Herring, 1952) generate dislocations that form a network and continuously climb. Dislocation multiplication occurs by the operation of dislocation sources, thus increasing their density, while climb of dislocations of opposite sign toward one another results in annihilation, thus decreasing their density. A balance between multiplication and annihilation results in steady-state creep described by the flow law (Nabarro, 1967; Nix et al., 1971)

$$\dot{\varepsilon} = 2 \frac{GV_m}{RT} \left(\frac{\sigma}{G}\right)^3 \frac{D}{b^2} \frac{1}{\ln(4G/\pi\sigma)} \qquad [47]$$

Although the steady-state strain rates obtained from the models developed by Weertman and Nabarro, eqns [46] and [47], respectively, differ in magnitude, these flow laws share fundamental elements. Both yield a cubic dependence of strain rate on differential stress and a linear dependence of strain rate on diffusivity. That is, both result in power-law equations similar to that given in eqn [43] with $m = 0$. The exponential dependence of strain rate on temperature enters through D as does at least part of the dependence of strain rate on oxygen and/or water fugacity. In detail, the dependence of diffusivity on fugacity enters through the concentration of the point defects (e.g., vacancies) that enable diffusion of ions, as expressed in eqn [16].

As discussed by Hirth and Lothe (1968, pp. 506–529) and Poirier (1985, pp. 58–62), the climb velocity is directly proportional to the concentration of jogs, c_j, times the migration velocity of jogs, v_j,

$$v_c = c_j v_j \qquad [48]$$

The jog migration velocity is directly proportional to the flux of ions to or from a dislocation and thus directly proportional to the self-diffusion coefficient of the slowest ion. It is usually assumed that dislocations are fully saturated with jogs (i.e., $c_j = 1$) such that the concentration of vacancies remains at local equilibrium along the dislocation line. If the concentration of jogs is significantly below this level (i.e., $c_j \ll 1$), then the jog concentration introduces an extra energy term into the climb velocity, such that the activation energy for climb will be larger than that for self-diffusion of the slowest ion. In addition, as discussed in the succeeding text, if the jog concentration depends on the concentration of other point defects, then c_j may also be a function of thermodynamic parameters such as oxygen fugacity and water fugacity (e.g., Hobbs, 1981, 1983, 1984).

For olivine under anhydrous conditions, the climb-based flow laws in eqns [46] and [47] significantly underpredict the observed rate of deformation for a given set of thermomechanical conditions. Measured laboratory strain rates are a factor of ~1000 slower than anticipated from eqn [47], for example, and an unrealistic value of $\boldsymbol{\mathcal{L}}_g/\boldsymbol{\mathcal{L}}_c$ of ~200 is needed to bring experiment and theory into agreement (Kohlstedt, 2006). The problem lies in the very slow rate of Si diffusion in olivine, since Si is the slowest-diffusing constituent ionic species and thus rate-controlling. Based on the Si diffusion results of Dohmen et al. (2002) with eqn [45], a dislocation can climb a distance of only ~1 nm in a 10 h experiment at an applied stress of 100 MPa at 1500 K. This value is much smaller than that indicated by the kinetics of dislocation recovery (Goetze and Kohlstedt, 1973; Karato and Sato, 1982;

Kohlstedt et al., 1980) and the dislocation microstructures in laboratory-deformed samples (Bai and Kohlstedt, 1992; Durham et al., 1977; Karato et al., 1986). A resolution to this problem was proposed by Hirth and Kohlstedt (2014) in a model that addresses the slow predicted rate of dislocation climb and the difference between the measured and predicted dependence of strain rate on stress ($n=3.6\pm0.2$ vs. $n=3.0$). These authors emphasize the role of diffusion along dislocation cores (pipe diffusion) as a mechanism that yields faster rates of diffusion and thus of climb. This model introduces an additional dependence of strain rate on dislocation density in the Orowan equation, eqn [42], by scaling the total cross-sectional area for pipe diffusion with the dislocation density (Spingarn et al., 1979). In addition, this model incorporates the measured dependence of dislocation density on applied stress, $\rho\propto\sigma^{1.37}$, rather than the commonly assumed relationship, $\rho\propto\sigma^{2}$ (eqn [40]). This approach thus directly accounts for the observed rate of dislocation recovery and the measured stress dependence of creep rate. It also helps explain the observation that, for constant oxygen fugacity conditions, the activation energy obtained from dislocation creep experiments, 450 kJ mol^{-1} (Keefner et al., 2011), is smaller than the activation for matrix diffusion of Si, 530 kJ mol^{-1} (Dohmen et al., 2002), as activation energies for short-circuit diffusion are consistently smaller than those for matrix diffusion.

2.18.3.1.2.2 Grain-boundary sliding and migration

Boundaries or interfaces separating neighboring grains often contribute substantially to plastic deformation of rocks. In the diffusion creep regime, sliding along grain and interphase boundaries is an essential aspect of deformation (Raj and Ashby, 1971). Thus, as discussed earlier in the text, diffusion creep might be more descriptively named diffusion-accommodated grain-boundary sliding.

Grain-boundary sliding (gbs) is also important during deformation in which dislocations dominate flow. Grain-boundary sliding has received a great deal of attention in the literature on superplastic deformation, a deformation process in which a solid is deformed (in tension) to very large strains (~1000% elongation) without failing by necking and subsequent fracture (see, e.g., Ridley, 1995). Based on microstructural analyses, Boullier and Gueguen (1975) argued that superplastic flow is responsible for deformation in at least some mylonites. Schmid et al. (1977) and Goldsby and Kohlstedt (2001) discussed the possibility of superplastic flow in their deformation experiments on limestone and ice, respectively. Recently, Hiraga et al. (2010) conclusively demonstrated superplasticity in fine-grained aggregates of forsterite + periclase and of forsterite + diopside + enstatite by deforming samples in tension to strains of several hundred percent without fracturing. However, as Poirier (1985, p. 204) pointed out, "superplasticity is a behavior, not a definite phenomenon." Thus, in this chapter, emphasis is given to the coupling between grain-boundary sliding and dislocation glide and/or climb as a deformation process without appealing specifically to the term superplasticity.

In this regime, strain rate varies with differential stress according to a power-law relationship such as the one presented in eqn [43] with $m>0$ and $n>1$. This observation immediately implies that grain-boundary sliding cannot be accommodated simply by diffusion, which would lead to a linear dependence of strain rate on stress (e.g., Ashby and Verrall, 1973). A number of models examine deformation processes involving grain-boundary sliding coupled with dislocation motion. A few of these studies are mentioned here to bring out the key elements of this process, with more extensive lists of references available in Poirier (1985, Section 7.4) and elsewhere (Kaibyshev, 1992; Langdon, 1994, 1995).

Ball and Hutchinson (1969), Mukherjee (1971), and Gifkins (1976, 1978) considered the motion of grain-boundary dislocations impeded by obstacles in the grain boundaries. Stress concentrations that develop at ledges or triple junctions are relieved by the generation of dislocations that then move through the adjoining grains. These dislocations, piled up against neighboring grain boundaries, are removed by climb into the grain boundaries. As these extrinsic dislocations move along grain boundaries, they contribute to grain-boundary sliding. Kaibyshev (2002) in particular emphasized the importance of this excess population of dislocation in grain boundaries due to the interaction of grain boundaries with lattice dislocations. This approach leads to the flow law

$$\dot{\varepsilon}=A_{\mathrm{gbs}}\frac{D_{\mathrm{gb}}}{d^{2}}\frac{GV_{\mathrm{m}}}{RT}\left(\frac{\sigma}{G}\right)^{2} \qquad [49]$$

where the value of the parameter A_{gbs}, which depends on the details of the grain-boundary sliding process and the dislocation recovery mechanism (see Langdon, 1994), has a value of order 10. This type of analysis is applied to the situation in which a subgrain structure does not build up within the individual grains so that dislocations move relatively freely from one grain boundary, across the grain, to the opposite grain boundary.

If grains contain subgrains, then dislocations that are generated by sliding along a grain boundary glide across the adjoining grain until they encounter a subgrain boundary. The dislocations then climb into the subgrain boundary, interact with dislocations in the subgrain wall, and are annihilated (Langdon, 1994). This type of analysis leads to a flow law of the form

$$\dot{\varepsilon}=B_{\mathrm{gbs}}\frac{D_{\mathrm{gm}}}{d^{1}}\frac{GV_{\mathrm{m}}}{RT}\left(\frac{\sigma}{G}\right)^{3} \qquad [50]$$

with $B_{\mathrm{gbs}}\approx1000$. Note that eqns [49] and [50] differ in their dependence on stress (σ^{2} vs. σ^{3}), on grain size ($1/d^{2}$ vs. $1/d$), and on temperature (Q_{gb} vs. Q_{gm}).

In silicates, evidence for creep involving dislocation-accommodated grain-boundary sliding was identified in deformation data for dry olivine (Hansen et al., 2011; Hirth and Kohlstedt, 1995b, 2003; Wang et al., 2010) and was apparent in the creep results for dry clinopyroxene (Bystricky and Mackwell, 2001) for which a coarse-grained rock is a factor of ~10 stronger than a fine-grained sample fabricated from powders prepared from the coarse-grained rock. In rocks composed primarily of highly anisotropic minerals such as olivine, which has only three independent slip systems, grain-boundary sliding can be very important because it relaxes the von Mises criterion of five independent slip systems for homogeneous deformation or four independent slip systems for volume-conserved inhomogeneous deformation. As a consequence, the strength of coarse-grained dunites lies between those of the stronger two slip systems (Keefner et al., 2011), while the strength of fine-grained dunites for which grain-boundary sliding is a significant deformation mechanism approaches that of the weakest slip system (Hirth and Kohlstedt, 1995b). Interestingly, this dislocation-accommodated grain-boundary sliding regime appears to be absent in olivine-rich rocks deformed under hydrous conditions, possibly because a water (hydrogen)-induced enhancement in ionic diffusivity and thus in dislocation climb velocity provides the extra deformation process required to fulfill the relaxed von Mises criterion (Hirth and Kohlstedt, 2003). As a result, in the hydrous case, the strengths of coarse-grained and fine-grained dunites are both similar to that of the weakest slip system (Mei and Kohlstedt, 2000a).

In addition to their contribution to deformation by producing strain via sliding, grain boundaries facilitate deformation by migrating in response to the strain energy associated with high densities of dislocations within the grains. This dynamic recrystallization process does not itself produce strain; however, it does remove dislocations within grains, resulting in a population of small grains that are, at least initially, free of dislocations. Dislocations generated at grain boundaries can more easily glide across these dislocation-free grains, unimpeded by interactions with other dislocations, than through larger grains that contain high densities of dislocations. In addition, since the contribution of grain-boundary sliding to deformation increases with decreasing grain size as indicated in eqns [49] and [50], grain-boundary sliding can contribute to deformation in regions composed primarily of small grains, thus also enhancing the rate of deformation. Hence, dynamic recrystallization often results in 'strain softening,' a reduction in creep strength with constant-rate, progressive deformation (i.e., increasing strain) of a rock (e.g., de Bresser et al., 2001; Drury, 2005; Platt and Behr, 2011). Dynamic recrystallization can also occur by subgrain rotation by which dislocations are removed from the interiors of grains by addition to low-angle boundaries (e.g., Poirier, 1985, pp. 169–177). As dislocations are added to these (low-angle) subgrain boundaries, the misorientation angle increases until distinct new grains (i.e., high-angle grain boundaries) form. An example of dynamic recrystallization involving both grain-boundary migration and subgrain rotation is presented in **Figure 9**. Again, the removal of dislocations from within the grains reduces temporarily the number of obstacles to dislocation glide, and the formation of smaller grains makes the operation of grain size-sensitive deformation processes (diffusion creep and dislocation-accommodated grain-boundary sliding) more favorable.

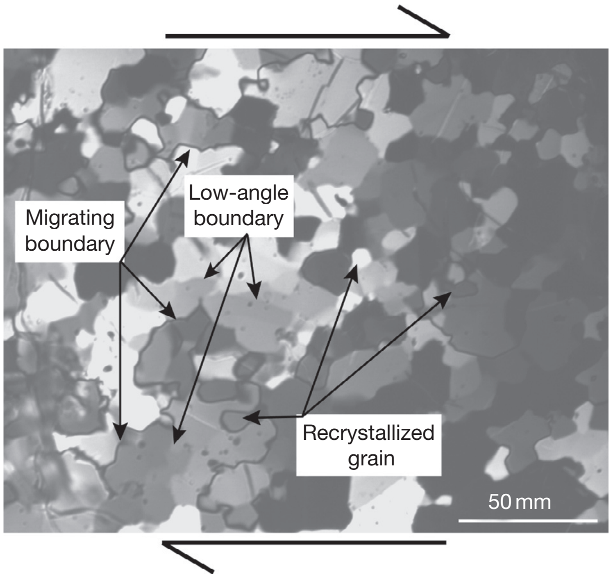

Figure 9 Transmitted light optical micrograph with polarizers crossed of thin section of (Fe$_{0.5}$ Mg0$_{.5}$)$_2$SiO$_4$ illustrating the process of dynamic recrystallization occurring by both subgrain rotation and grain-boundary migration. Sample was deformed in torsion to a shear strain of $\gamma = 4$. Figure courtesy of Y.-H. Zhao.

2.18.3.1.2.3 *Low-temperature plasticity*

At lower temperatures and hence higher stresses, power-law formulations underpredict the observed increase in strain rate with increasing stress. As temperature decreases, diffusion becomes too slow to permit a significant contribution of dislocation climb to the deformation process. The rate of deformation then becomes limited by the ability of dislocations to glide past obstacles. In silicate minerals with a significant component of covalent bonding, dislocations must overcome the resistance imposed by the lattice itself, often referred to as the Peierls barrier (e.g., Frost and Ashby, 1982, pp. 6–9). Motion of dislocations over the Peierls barrier requires the nucleation and migration of kinks (steps along dislocation lines that lie in the glide plane), with the nucleation rate of pairs of kinks generally assumed to limit the dislocation velocity (Frost and Ashby, 1982, p. 8). The dislocation velocity is determined by the glide velocity, v_g, and consequently by the kink velocity, v_k:

$$v \approx v_g = c_k v_k \qquad [51]$$

where c_k is the concentration of kinks. The activation enthalpy for the nucleation and migration of double kinks, $\Delta H_k(\sigma)$, is a function of differential stress. A detailed analysis for $\Delta F_k(\sigma)$ yields (Frost and Ashby, 1982, p. 8; Kocks et al., 1975, p. 243)

$$\Delta F_k(\sigma) = \Delta F_k^o \left[1 - \left(\frac{\sigma}{\sigma_P}\right)^r\right]^s \qquad [52]$$

where ΔF_k^o is the Helmholtz free energy of an isolated pair of kinks, σ_P is the Peierls stress, and r and s are model-dependent parameters (Frost and Ashby, 1982, p. 9). From the Orowan equation, eqn [42], the flow law then becomes

$$\dot{\varepsilon} = \dot{\varepsilon}_P \left(\frac{\sigma}{G}\right)^2 \exp - \left\{\frac{\Delta F_k^o}{RT}\left[1 - \left(\frac{\sigma}{\sigma_P}\right)^r\right]^s\right\} \qquad [53]$$

where $\dot{\varepsilon}_P$ is a material-dependent parameter.

2.18.3.1.3 *Deformation mechanism maps*

An illustrative method for displaying the conditions under which a given deformation mechanism dominates flow is the deformation mechanism map (Frost and Ashby, 1982). At present, olivine is the only mineral for which data exist in the diffusion, dislocation, grain-boundary sliding, and low-temperature plasticity regimes. Four parameters are usually considered when constructing a deformation mechanism map: strain rate, stress, grain size, and temperature. The examination of eqn [32] indicates that other parameters could be included (e.g., pressure, water fugacity, and melt fraction) depending on the application. Flow parameters for the diffusion and dislocation creep regimes are taken from Hirth and Kohlstedt (2003). Flow parameters for the dislocation-accommodated grain-boundary sliding regime and modified flow parameters for diffusion creep are used from Hansen et al. (2011), while those for the low-temperature plasticity regime are from Mei et al. (2010). The Mei et al. (2010) results, which were obtained in creep experiments in a deformation-DIA apparatus, yield somewhat larger strengths than those obtained from microindentation experiments of Goetze (1978) and Evans and Goetze (1979).

Here, the classical form is first used in which stress is plotted as a function of temperature for a fixed grain size (and fixed pressure, water fugacity, etc.) with strain rate illustrated parametrically. In **Figure 10(a)** and **10(b)**, differential stress is plotted as a function of temperature for dunite rocks composed of 10 μm grains and 1000 μm grains, respectively. For a fine-grained rock with $d = 10$ μm such as might be found in a shear zone (**Figure 10(a)**), diffusion creep dominates at geologic strain rates, 10^{-15}–10^{-10} s^{-1}, for stresses below ~100 MPa. At higher stresses, dislocation-accommodated grain-boundary sliding becomes important, and at still higher stresses, low-temperature plasticity dominates. For a coarser-grained rock with $d = 1000$ μm such as might be expected in the upper mantle (**Figure 10(b)**), dislocation-accommodated grain-boundary sliding is dominant over more than three orders of magnitude in stress for strain rates relevant to both lithospheric shear zones and asthenospheric flow.

An alternative form of the deformation mechanism map that provides insight into mantle deformation process is obtained by plotting stress as a function of grain size with strain rate again shown parametrically, as illustrated in **Figure 11**. The greater importance of dislocation-accommodated grain-boundary sliding at the lower temperature (800 °C vs. 1300 °C) is clear in this comparison. This behavior reflects the fact that the activation energy for dislocation-accommodated grain-boundary sliding appears to be smaller than that for dislocation creep, ~445 kJ mol^{-1} (Hansen et al., 2011) versus ~530 kJ mol^{-1} (Hirth and Kohlstedt, 2003). Also, the contribution of low-temperature plasticity is, as expected, greater at 800 °C. Finally, at 1300 °C, the range of grain sizes over which dislocation-accommodated grain-boundary sliding is the dominant mechanism is reduced by an order of magnitude, which primarily serves to increase the grain-size range over which dislocation creep is the dominant mechanism.

2.18.3.2 Role of Fluids in Rock Deformation

Melt and water significantly influence the strength of a rock. If either is present even in small concentration, it profoundly affects rock viscosity.

2.18.3.2.1 Role of melt in rock deformation

The influence of melt on rock viscosity enters constitutive equations in two ways (for reviews, see Kohlstedt, 1992, 2002; Xu et al., 2004). First, melt provides a path along which ions can diffuse more rapidly than they can either through grain interiors or along grain boundaries. Second, since melt does not support shear stresses, for a given applied macroscopic stress, the stress at the grain scale will be locally increased if melt is present.

Both of these contributions to the high-temperature strength of a rock were included in the analysis of Cooper and Kohlstedt (1984, 1986) and Cooper et al. (1989) of the effect of melt on diffusion creep of aggregates composed of a fluid phase plus a solid phase. Such analyses depend critically on the distribution of the melt phase. In this particular model, the melt distribution was assumed to be dictated by surface tension for an isotropic system under a hydrostatic state of stress for which the dihedral angle, θ, is determined by the relative values of the solid–liquid and solid–solid interfacial energies, γ_{sl} and γ_{ss}, respectively:

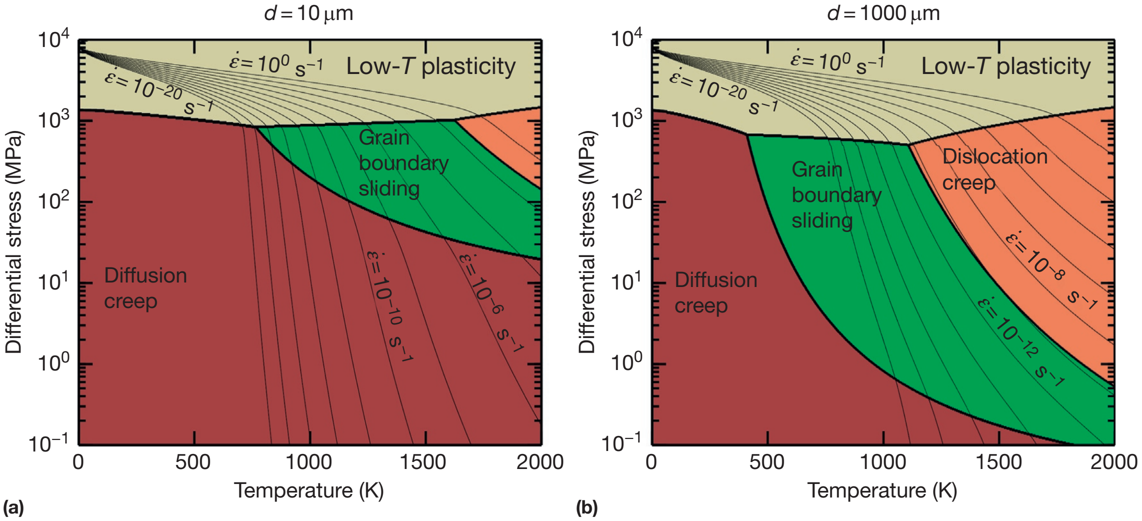

Figure 10 Deformation mechanism maps plotted as differential stress as a function of temperature for dunite with grain sizes of (a) 10 μm and (b) 1000 μm. (a) At the smaller grain size for a strain rate of 10^{-15} s^{-1}, deformation occurs by diffusion creep for stresses up to ~200 MPa above which deformation is dominated by grain-boundary sliding and then by low-temperature plasticity. (b) At the larger grain size for a strain rate of 10^{-15} s^{-1}, deformation occurs by grain-boundary sliding for a much larger range of stress (0.2–600 MPa).

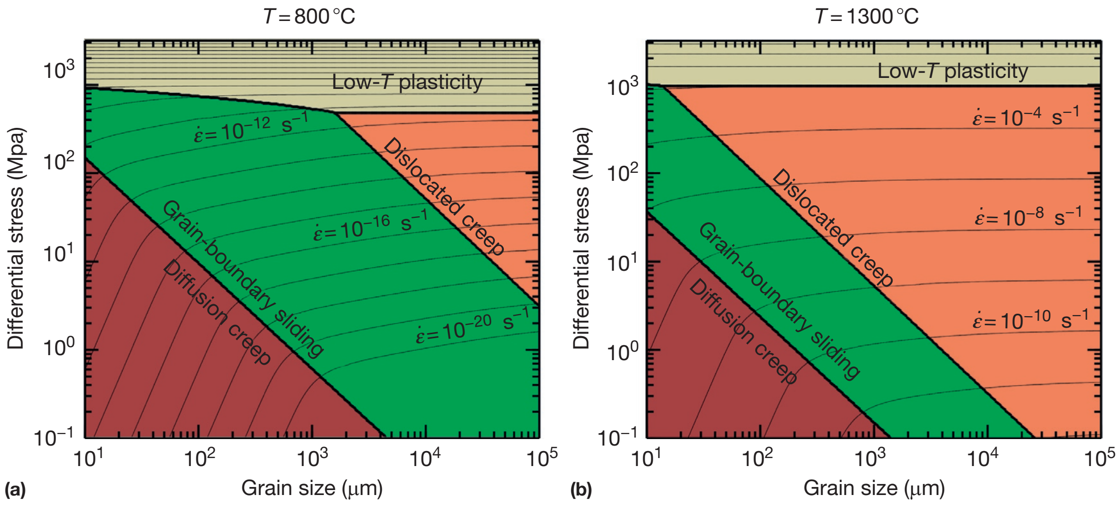

Figure 11 Deformation mechanism maps plotted as differential stress as a function of grain size for dunite at temperatures of (a) 800° and (b) 1300 °C. (a) At the lower temperature for a strain rate of 10^{-15} s^{-1}, deformation occurs by diffusion creep for grain sizes less than ~80 μm, by grain-boundary sliding at grain sizes between 80 and 10 000 μm, and by dislocation creep at grain sizes larger than 10 000 μm. (b) At a comparable stress for the higher temperature, the boundary between diffusion creep and grain-boundary sliding occurs at a factor of ~2 smaller grain size than at the lower temperature, but the boundary between grain-boundary sliding and dislocation creep occurs at a factor of ~100 smaller grain size than at a comparable stress for the lower temperature.

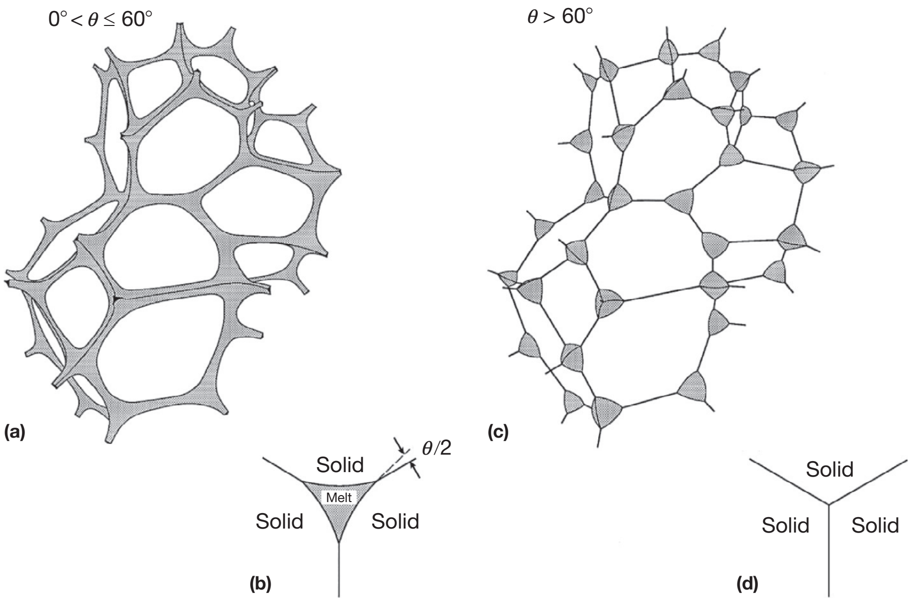

Figure 12 Sketch of melt distribution in a partially molten rock with isotropic interfacial energies. In (a) with $0° < \theta \le 60°$, melt wets all of the triple junctions and four-grain junctions; (b) cross section through a triple junction midway along a grain edge illustrates the presence of melt. In (c) with $\theta > 60°$, melt is confined to four-grain junctions; (d) cross section through a triple junction midway along a grain edge illustrates the absence of melt. Modified from Riley Jr GN and Kohlstedt DL (1990) An experimental study of melt migration in an olivine–melt system. In: Ryan MP (ed.), Magma Transport and Storage. John Wiley & Sons, New York, pp. 77–86.

$$\cos\left(\frac{\theta}{2}\right)=\frac{\gamma_{ss}}{2\gamma_{sl}} \qquad [54]$$

For the olivine + MORB case, the average dihedral angle is ~40° (i.e., $0<\theta<60°$) such that, ideally, melt forms an interconnected network along three-grain junctions and through four-grain corners, such as illustrated in Figure 12. Average values for dihedral angle of <60° are observed for many rocks composed of silicate minerals plus a silicate melt. However, as illustrated in Figure 13, for melt fractions greater than ~0.05, the model of Cooper and Kohlstedt (e.g., Cooper and Kohlstedt, 1986) significantly underpredicts the decrease in viscosity measured in experiments on partially molten rocks in the diffusion creep regime (Hirth and Kohlstedt, 1995a; Zimmerman and Kohlstedt, 2004).

One important aspect not taken into account in the previously mentioned analysis is the fact that the wetting behavior of most partially molten systems is not isotropic (e.g., Cooper and Kohlstedt, 1982). As illustrated in **Figure 14**, microstructural observations demonstrate that melt wets a fraction of the grain boundaries, behavior not predicted for an isotropic system with $\theta > 0°$. Furthermore, the percentage of grain boundaries wetted by melt increases with increasing melt fraction, ϕ (Hirth and Kohlstedt, 1995b).

To deal with the influence of melt distribution on diffusion creep, Takei and Holtzman (2009a) expressed the viscosity of a partially molten rock in terms of grain-boundary contiguity, φ, a state variable equal to the ratio of grain-boundary area to grain-boundary area plus grain–melt interfacial area. This model extends that of Cooper and Kohlstedt (1984, 1986) from two to three dimensions, incorporating the observed anisotropic wetting of grains. The Takei and Holtzman (2009a) analysis expresses the viscosity of a partially molten rock in terms of contiguity and the viscosity of the melt-free material, η_0, as

$$\eta(\phi) = 0.2\varphi^2\eta_0 = 0.2\left(1 - A\phi^{1/2}\right)^2\eta_0 \qquad [55]$$

Contiguity is then written in terms of melt fraction using the semiempirical relationship $\varphi = (1 - A\phi^{1/2})$ with $A = 2.3$. One important result of this model is that it predicts a factor of greater than five decrease in viscosity as melt fraction is increased from 0 to 0.001 (i.e., 0.1% melt). This model yields a good fit to the experimental data on samples of borneol + diphenylamine, an organic binary eutectic system (McCarthy and Takei, 2011), and samples of sol–gel-derived olivine + basaltic melt (Faul and Jackson, 2007). Both materials exhibit the predicted large decrease in viscosity in going from $\phi = 0$ to $\phi = 0.001$, as illustrated in **Figure 15** for the organic system.

Experimental determinations of strain rate as a function of melt fraction in both the diffusion creep regime and the dislocation creep regime have been empirically fit to the relation

$$\dot{\varepsilon}(\phi) = \dot{\varepsilon}(0)\exp(\alpha\phi^r) \qquad [56]$$

for melt fractions from near zero to the rheologically critical melt fraction (RCMF) with $r = 1$ for the olivine + basalt system (Kelemen et al., 1997; Mei et al., 2002; Scott and Kohlstedt, 2006) and the borneol plus eutectic melt system (Takei, 2005) and $r = 3$ for a partially molten granitic rock (Rutter and Neuman, 1995; Rutter et al., 2006). This exponential dependence of strain rate on melt fraction is consistent with the dependence of viscosity on melt fraction derived by Takei and Holtzman (2009a) given by eqn [55] for $\phi \gtrsim 0.01$ with $r = 1$ and $\alpha = 23$, as illustrated in **Figure 15**.

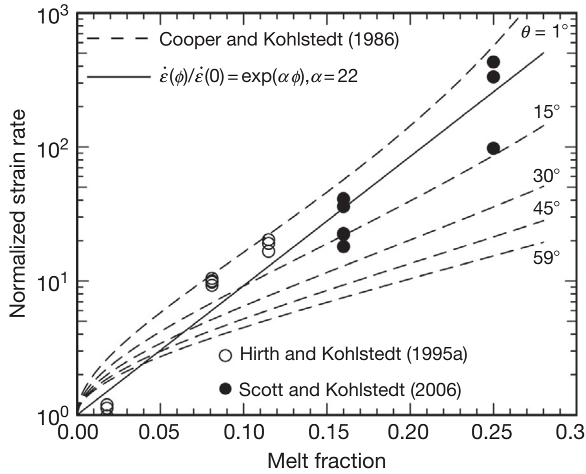

Figure 13 Plot of normalized strain rate, $\dot{\varepsilon}(\phi)/\dot{\varepsilon}(0)$, versus melt fraction. Circles are the experimentally determined values; for $\phi < 0.15$, data are from Hirth and Kohlstedt (1995a), while for $\phi > 0.15$, data are from Scott and Kohlstedt (2006). Dashed curves are based on the model of Cooper and Kohlstedt (1986) for $1° \leq \theta \leq 59°$. Solid line is a fit of the experimental data to the empirical relationship $\dot{\varepsilon}(\phi)/\dot{\varepsilon}(0) = \exp(\alpha\phi)$, yielding $\alpha = 22$.

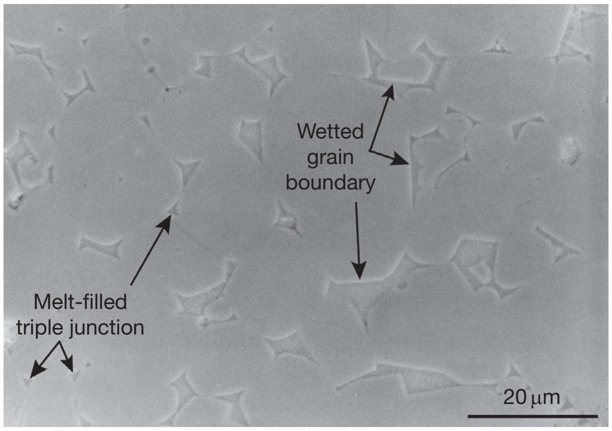

Figure 14 Backscattered scanning electron micrograph of sample of olivine + 5% basalt. Both melt-filled triple junctions and wetted grain boundaries are identified. The presence of wetted grain boundaries demonstrates that the interfacial energies are anisotropic in this system, since melt would be confined to triple junctions in an isotropic system with a similar dihedral angle of $\theta \approx 40°$.

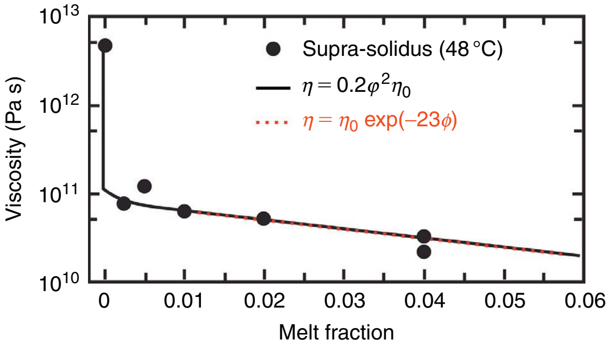

Figure 15 Viscosity as a function of melt fraction for the borneol ($C_{10}H_{18}O$)–diphenylamine ($(C_6H_5)_2NH$) binary eutectic organic system, which has a eutectic temperature of $T_e = 43$ °C. The data are well fit by eqn [55], which relate viscosity to melt fraction (Takei and Holtzman, 2009a). At melt fractions greater than ~0.01, the experimental results are also well described by the empirically derived, exponential relationship between viscosity and melt fraction, eqn [56]. Modified from McCarthy C and Takei Y (2011) Anelasticity and viscosity of partially molten rock analog: Toward seismic detection of small quantities of melt. *Geophysical Research Letters* 38: http://dx.doi.org/10.1029/2011GL048776.

At least for $\phi \gtrsim 0.01$, melt has a greater influence on viscosity in the dislocation creep regime than in the diffusion creep regime for the olivine+basalt and partially molten lherzolite systems (Mei et al., 2002; Scott and Kohlstedt, 2006; Zimmerman and Kohlstedt, 2004). This point is illustrated in **Figure 16** with $\alpha = 21$ in the diffusion creep regime and $\alpha = 32$ in the dislocation creep regime. At melt fractions greater than the RCMF, a partially molten rock behaves as a fluid (melt) containing suspended particles. The Einstein–Roscoe equation (Roscoe, 1952),

$$\eta_{\mathrm{ER}}(\phi) = \frac{\mu}{(1.35\phi - 0.35)^{2.5}} \qquad [57]$$

which reasonably well describes the viscosity of a system with $\phi > 0.25$–0.30, is also shown in **Figure 16**. In eqn [57], μ is the melt viscosity. It is also important to note that the onset of melting will affect grain-boundary chemistry, which will indirectly – but significantly – affect rock viscosity through its influence on the rates of ionic diffusion along grain boundaries (Hiraga et al., 2007; McCarthy and Takei, 2011).

Importantly, not only does a small amount of melt significantly affect rock viscosity, but also, in turn, deformation profoundly influences melt distribution (Holtzman et al., 2003a,b; King et al., 2010; Kohlstedt and Zimmerman, 1996; Kohlstedt et al., 2010; Takei and Holtzman, 2009a, 2009b). The scale and extent of the influence of stress on melt distribution are determined by the compaction length, δ_c (Holtzman et al., 2003a; Stevenson, 1989), where $\delta_c = \sqrt{(k/\mu)\left(\frac{4}{3}\eta + \zeta\right)}$ with k the permeability, η the shear viscosity, and ζ the bulk viscosity. For δ_c larger compared to the size of the region (sample) undergoing deformation, melt aligns 15–25° to the shear plane, antithetic to the shear direction (Kohlstedt and Zimmerman, 1996, Zimmerman et al., 1999). An example of stress-driven melt alignment is presented in **Figure 17** for the olivine+basalt system. For δ_c smaller than the region of deformation, melt spontaneously segregates into melt-enriched bands, again aligned 15–25° to the shear plane, antithetic to the shear direction (Holtzman et al., 2003a,b; King et al., 2010; Kohlstedt et al., 2010). An example of stress-driven melt segregation is included in **Figure 18** for an olivine+basalt+chromite sample. The role of chromite in this sample is to reduce the permeability and thus the compaction length (Holtzman et al., 2003a).

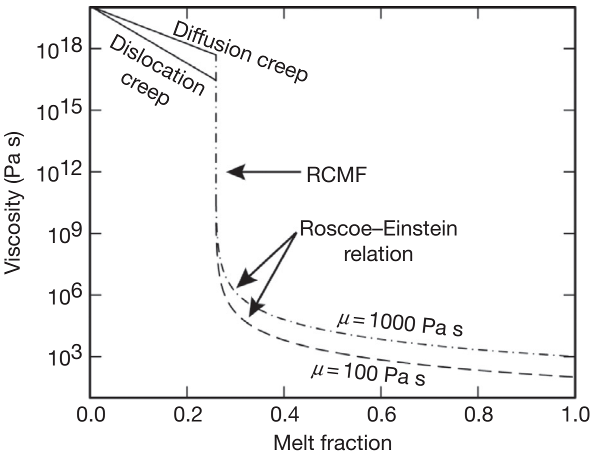

Figure 16 Plot of viscosity of a partially molten rock versus melt fraction for $\phi > 0.01$ illustrating the transition between flow controlled by a framework of solid particles with interstitial melt and flow dominated by melt with suspended particles. At low melt fractions, dislocation creep and diffusion creep are described by eqn [55] with $r = 1$ and $\alpha = 21$ and 32, respectively. At the rheologically critical melt fraction, which marks the transition from solid-like to fluid-like behavior, viscosity plummets rapidly with increasing melt fraction. At higher melt fractions, $\phi > 0.25$–0.30, the Roscoe–Einstein relation, eqn [56], describes deformation of a mixture of melt with suspended particles. Modified from Scott T and Kohlstedt DL (2006) The effect of large melt fraction on the deformation behavior of peridotite. *Earth and Planetary Science Letters* 246: 177–187.

The formation of melt-enriched bands or sheets occurs in partially molten rocks for which viscosity decreases with increasing melt fraction (Stevenson, 1989). In these rocks, the melt-enriched bands develop at a low angle to the shear plane (**Figure 18**) as a result of the viscous anisotropy produced by stress-driven alignment of melt at the grain scale (**Figure 17**), that is, microstructural anisotropy (Takei and Holtzman, 2009b; Takei and Katz, 2013). These melt-enriched layers have a significantly lower viscosity than the neighboring melt-depleted regions, thus forming zones of localized deformation (shear zones) that reduce the rock viscosity relative to the viscosity of a partially molten rock in which the melt is homogeneously distributed (Holtzman et al., 2012; King et al., 2010). Melt-enriched layers also act as high-permeability paths for rapid extraction of melt from the mantle (Kelemen and Dick, 1995; Kohlstedt and Holtzman, 2009).

2.18.3.2.2 Role of water in rock deformation

Water weakening of nominally anhydrous silicate minerals was first observed in the mid-1960s in an experimental study of the strength of quartz (Griggs and Blacic, 1965). In these solid-

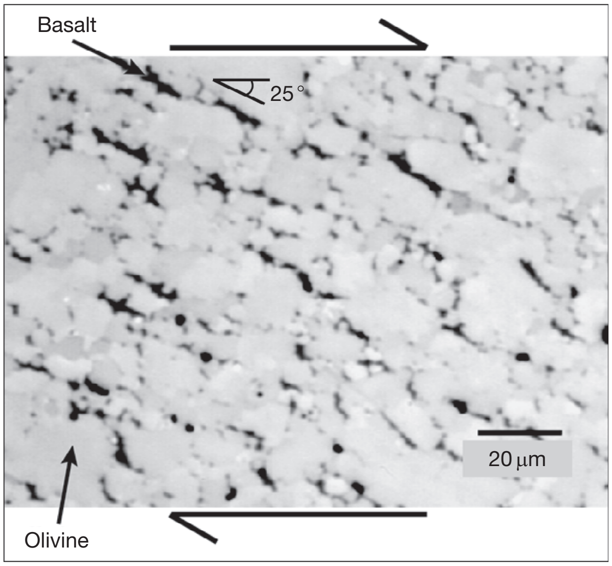

Figure 17 Sample of olivine+3 vol% MORB deformed in general shear. Melt (black) is aligned at the grain scale 20–25° to the shear plane, antithetic to the shear direction. Olivine grains are light gray. Modified from Kohlstedt DL and Zimmerman ME (1996) Rheology of partially molten mantle rocks. *Annual Review of Earth and Planetary Sciences* 24: 41–62.

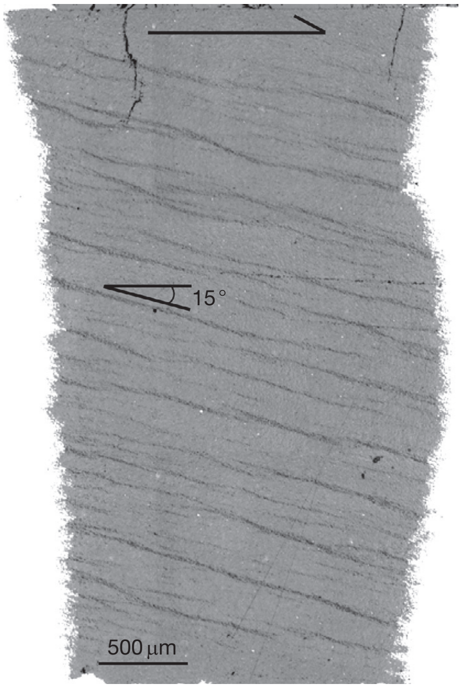

Figure 18 Reflected light photomicrograph of a tangential surface of a sample of olivine (72%), chromite (24%), and basalt (4%) deformed in torsion to an outer-radius shear strain of 1.3 at an outer-radius strain rate of $1.8\times10^{-5}\ \mathrm{s}^{-1}$ and outer-radius shear stress of 57 MPa. The darker bands trending NW–SE are melt-enriched, containing up to ~20 vol% basalt. The lighter gray regions are melt-depleted, containing <1 vol% basalt. Two unloading cracks extend from the top dunite piston a short distance into the sample. Modified from King D, Zimmerman ME, and Kohlstedt DL (2010) Stress-driven melt segregation in partially molten olivine-rich rocks deformed in torsion. *Journal of Petrology* 51: 21–42, http://dx.doi.org/10.1093/petrology/egp062.

medium deformation experiments, samples deformed with a hydrous confining medium (talc) were weaker than samples deformed with an anhydrous confining medium. Subsequently, water weakening has been reported for other nominally anhydrous minerals (NAMs) including olivine (e.g., Avé Lallemant and Carter, 1970), pyroxene (Avé Lallemant, 1978), and feldspar (e.g., Tullis and Yund, 1980). These first studies of water weakening emphasized the phenomenon. A second generation of experiments focused on the mechanism of water weakening by studying the dependence of viscosity on water fugacity, that is, on the concentration of water-derived point defects (Chen et al., 2006; Karato and Jung, 2003; Kohlstedt et al., 1995; Kronenberg and Tullis, 1984; Mei and Kohlstedt, 2000a,b; Post et al., 1996).

The first model of water or hydrolytic weakening was built on a mechanism in which water hydrolyzes strong Si—O bonds forming weaker Si–OH···OH–Si bonds (Griggs, 1967). Thus, dislocation glide is easier under hydrous conditions than under anhydrous conditions; effectively, the Peierls stress/barrier decreases as Si—O—Si bridges become hydrolyzed. In this analysis, the rate of dislocation glide is limited by the propagation of kinks along dislocations, a process facilitated by the diffusion of water along dislocation cores. Dislocation velocity is then taken to be proportional to the concentration of water (Griggs, 1974).

More recent models of water weakening have emphasized the role of water-derived point defects, particularly hydrogen ions (protons) (Hobbs, 1981, 1983, 1984; Mackwell et al., 1985; Poumellec and Jaoul, 1984). Protons diffuse rapidly in NAMs (for a review, see Ingrin and Skogby, 2000) such as quartz (Kronenberg et al., 1986), olivine (Demouchy and Mackwell, 2003; Kohlstedt and Mackwell, 1998, 1999; Mackwell and Kohlstedt, 1990), and pyroxene (Carpenter Woods et al., 2000; Hercule and Ingrin, 1999; Ingrin et al., 1995; Stalder and Skogby, 2003). Thus, initially dry, millimeter-size samples can be hydrated in high-temperature, high-pressure experiments lasting a few hours or less. The presence of protons in a NAM affects the velocity of a dislocation in two possible ways. First, since protons are charged, a change in the concentration of protons will result in a change in the concentration of all other charged point defects. Hence, the introduction of protons into a NAM will directly affect the concentrations of vacancies and self-interstitials on each ionic sublattice and consequently the rates of diffusion of the constituent ions and the rate of dislocation climb. In addition, extrinsic point defects, specifically water-derived point defects, can affect the concentrations of kinks and jogs along dislocation lines and thus dislocation velocity as expressed in eqns [48] and [51] (Hirsch, 1979, 1981; Hobbs, 1981, 1984). The effect of water-derived point defects on the concentrations of kinks and jogs can enter defect reactions in two ways. First, for minerals containing a transition metal such as Fe (i.e., semiconducting silicates), the presence of water-derived point defects will affect the concentration of electron holes, $h^{\bullet}$, which in turn can affect the concentrations of kinks and jogs by ionizing initially neutral jogs (Hirsch, 1979, 1981; Hobbs, 1984). For the case of kinks, a positively charged kink, $k^{\bullet}$, can be produced from a neutral kink by the reaction

$$k^{\times} + h^{\bullet} \leftrightarrow k^{\bullet} \qquad [58]$$

for which the law of mass action yields

$$[k^{\bullet}] = K_{58}[k^{\times}][h^{\bullet}] \qquad [59]$$

The total concentration of kinks then becomes

$$\left[k^{\mathrm{tot}}\right] = [k^{\times}] + [k^{\bullet}] = [k^{\times}](1 + K_{58}[h^{\bullet}]) \qquad [60]$$

where the second term can be much larger than unity and dominate the kink population. The dependence of kink concentration on water (proton) concentration or water fugacity then enters through the concentration of positively charged kinks, thus enhancing the dislocation glide velocity. A similar argument can be used for increasing the concentration of jogs and thus the dislocation climb velocity. While this approach provides one mechanism for increasing dislocation velocity in NAMs, it is not easily extended to minerals such as quartz that do not contain significant concentrations of transition metals. Therefore, a more direct influence of water-derived point defects on kink and jog concentrations needs to be considered. In point defect notation, the addition of protons, $p^{\bullet}$, to a nominally anhydrous silicate will affect the concentration of kinks through a reaction such as

$$k^{\times} + p^{\bullet} \Leftrightarrow \{k^{\times} - p^{\bullet}\}^{\bullet} \qquad [61]$$

where the curly brackets, { }, indicate the formation of a neutral kink associated with a proton. The application of the law of mass action yields

$$[\{k^{\times} - p^{\bullet}\}^{\bullet}] = K_{61}[k^{\times}][p^{\bullet}] \qquad [62]$$

The total concentration of kinks is then

$$[k^{\mathrm{tot}}] = [k^{\times}] + [\{k^{\times} - p^{\bullet}\}^{\bullet}] = [k^{\times}](1 + K_{61}[p^{\bullet}]) \qquad [63]$$

Again, a similar equation applies for jogs. The dependence of kink and jog concentrations on water concentration/fugacity then comes directly through the dependence of proton concentration on water fugacity.

The high-temperature deformation behaviors of anorthite, clinopyroxene, and olivine deformed in the dislocation creep regime under anhydrous and under hydrous conditions are compared in **Figure 19**. A similar comparison was made for the diffusion creep regime by Hier-Majumder et al. (2005a). In the dislocation creep regime, the dependence of strain rate on water fugacity has been quantified for olivine (Hirth and Kohlstedt, 2003; Karato and Jung, 2003; Mei and Kohlstedt, 2002b) and for clinopyroxene (Chen et al., 2006). In the case of olivine, strain rate increases as water fugacity to the ~1st power, while in the case of clinopyroxene, strain rate increases as water fugacity to the ~3rd power. In the diffusion creep regime, creep rate increases as water fugacity to the ~1st power for olivine (Mei and Kohlstedt, 2000a) and to the ~1.4 power for clinopyroxene (Hier-Majumder et al., 2005a).

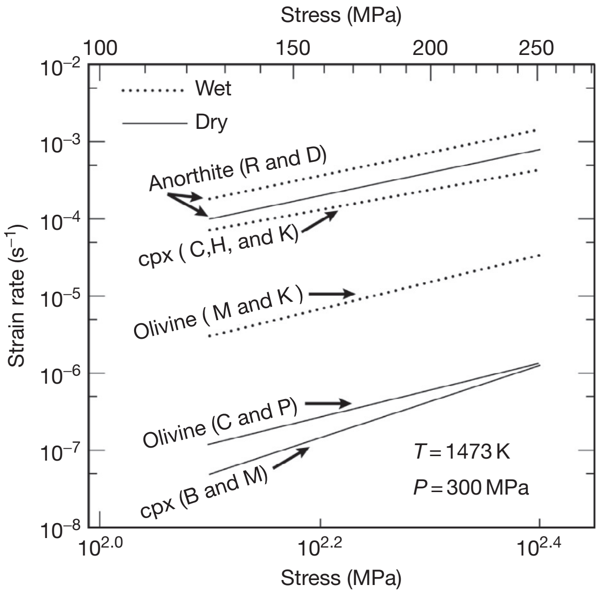

Figure 19 Strain rate versus stress for samples of anorthite, clinopyroxene, and olivine deformed in the dislocation creep regime under anhydrous and hydrous conditions. In each case, samples deformed under hydrous conditions are weaker than those deformed under anhydrous conditions. The water fugacity for samples deformed under hydrous conditions at a confining pressure of 300 MPa and 1473 K is ~300 MPa. Results are taken from R&D, Rybacki and Dresen (2000); C,H,&K, Chen et al. (2006); Mei and Kohlstedt (2000a); Chopra and Paterson (1984); and Bystricky and Mackwell (2001).

To help assess possible explanations for these observed dependences of strain rate on water fugacity, **Table 2** summarizes the relationships between the concentration of various point defects and water fugacity for several charge neutrality conditions for a transition-metal silicate. For olivine under hydrous conditions, the activation energy for dislocation creep of 470–520 kJ mol^{-1} (Hirth and Kohlstedt, 2003; Karato and Jung, 2003) is somewhat larger than those for Si and O self-diffusion of 360 and 440 kJ mol^{-1}, respectively (Costa and Chakraborty, 2008). Over the temperature range explored experimentally (1200–1350 °C), the diffusivities of Si and O are of similar magnitude. Thus, if the high-temperature creep of olivine is controlled by dislocation climb limited by the diffusion of the slowest ionic species, it is not clear which species (Si or O) is rate-controlling. Karato and Jung (2003) proposed a model in which creep rates are controlled by dislocation climb with Si diffusing by a vacancy mechanism coupled with positively charged jogs leading to a water fugacity exponent of $q = 5/4$ in eqn [43], close to the value that they obtained from their deformation experiments of 1.2. A water fugacity exponent of 5/4 is also satisfied by Si diffusing via a vacancy mechanism with the dominate Si vacancy resulting from the defect associate $[(3H)'_{\mathrm{Si}}]$ with the charge neutrality condition $[h^{\bullet}] = [H'_{\mathrm{Me}}]$ (see **Table 2**). In both cases, it is difficult to reconcile the substantial difference between the activation energies for Si self-diffusion and creep.

The situation appears to be equally or possibly more complex for clinopyroxene. The stress exponent is $n = 2.7 \pm 0.3$, consistent with the climb-controlled creep models discussed in the preceding text. Unfortunately, diffusion data are lacking for comparison with the creep data. The relatively strong dependence of strain rate on water fugacity, $q = 3.0 \pm 0.6$, in the dislocation creep regime suggests that a simple climb-controlled mechanism may not apply for high-temperature deformation of clinopyroxene (see **Table 2**). One possible way to reconcile this large value for the water fugacity exponent is as follows: (a) Creep is climb-controlled; (b) charge neutrality condition is given by $[h^{\bullet}] = [H'_{\mathrm{Me}}]$ or by $[p^{\bullet}] = [H'_{\mathrm{Me}}]$; (c) strain rate is limited by Si diffusion by a vacancy mechanism involving the defect associate $\{4p^{\bullet} - V''''_{\mathrm{Si}}\}^{\times} \equiv (4H)^{\times}_{\mathrm{Si}}$; and (d) dislocations are undersaturated with jogs with the jog concentration dominated by neutral jogs associated with protons, $\{j^{\times} - p^{\bullet}\}^{\bullet}$, as in eqns [62] and [63]. These scenarios yield a water fugacity exponent for strain rate of 2¾ and 2½, both within the experimental uncertainty of the measured value. Clearly, diffusion data are critical in order to develop this type of argument more completely.

As is evident from the previously mentioned analysis of high-temperature creep data for olivine and clinopyroxene, unambiguous identification of creep mechanism is difficult, at best. The complication arises because multiple ionic species and defect types are involved, including some of the following: Si, O, Me, vacancies, interstitials, dislocations, jogs, and kinks. At the very least, robust diffusion results are required for all of the constituent ionic species, including not only the magnitude of diffusivity but also the dependence of diffusivity on temperature and water fugacity and on other thermodynamic parameters. Nonetheless, the application of rheological data to

Table 2 Dependence of point defect concentrations on water fugacity, expressed as the exponent q in the relationship $[\,]\propto f^{q}_{\mathrm{H_2O}}$, for several charge neutrality conditions for a transition-metal silicate

	$[\mathrm{Fe}^{\bullet}_{\mathrm{Me}}]$ $[h^{\bullet}]$	$[\mathrm{Fe}'_{\mathrm{Si}}]$	$[V''_{\mathrm{Me}}]$	$[(\mathrm{OH})^{\bullet}_{\mathrm{O}}]$ $[p^{\bullet}]$	$[H'_{\mathrm{Me}}]$	$[(2H)^{x}_{\mathrm{Me}}]$	$[O''_{i}]$	$[V''''_{\mathrm{Si}}]$	$[H'''_{\mathrm{Si}}]$	$[(2H)''_{\mathrm{Si}}]$	$[(3H)'_{\mathrm{Si}}]$	$[(4H)^{x}_{\mathrm{Si}}]$
$[\mathrm{h}^{\bullet}]=2[\mathrm{V}''_{\mathrm{Me}}]$	0	0	0	1/2	1/2	1	0	0	1/2	1	3/2	2
$[\mathrm{p}^{\bullet}]=2[\mathrm{V}''_{\mathrm{Me}}]$	−1/6	1/6	1/3	1/3	2/3	1	1/3	2/3	1	4/3	5/3	2
$[\mathrm{p}^{\bullet}]=[\mathrm{Fe}'_{\mathrm{Si}}]$	−1/4	1/4	1/2	1/4	3/4	1	1/2	1	5/4	3/2	7/4	2
$[\mathrm{h}^{\bullet}]=[\mathrm{H}'_{\mathrm{Me}}]$	1/4	−1/4	−1/2	3/4	1/4	1	−1/2	−1	−1/4	1/2	5/4	2
$[\mathrm{p}^{\bullet}]=[\mathrm{H}'_{\mathrm{Me}}]$	0	0	0	1/2	1/2	1	0	0	1/2	1	3/2	2

understanding and modeling mantle dynamics relies less on detailed models of creep processes and more on robust experimental results that can be extrapolated from laboratory to geologic conditions.

2.18.3.3 Role of Texture in Rock Deformation

Many deformed rocks exhibit textures defined by crystallographic alignment of the constituent mineral grains. This alignment arises from the viscous anisotropy inherent to most crystals, and strong crystallographic fabrics can therefore impart anisotropy in viscosity to an aggregate of grains. Texture development related to deformation is sensitive to deformation conditions, composition, and strain history. Several approaches have been formulated to simulate texture development and predict bulk constitutive behavior of rocks using constitutive equations derived from the deformation of single crystals. Thus, simulated textures and viscous anisotropy can be compared to those derived in the laboratory under known conditions and with known compositions to calibrate micromechanical models of rock deformation. In turn, those models can be used to interpret anisotropy in geophysical signals such as seismic velocity, electric conductivity, and lithospheric flexure.

2.18.3.3.1 Texture development during deformation

Single crystals deforming by the motion of dislocations change shape due to the operation of specific slip systems. For a force, F, applied to a crystal of cross-sectional area A, the shear stress resolved onto a slip system in the slip direction, σ_s, is defined by (Schmid and Boas, 1950, p. 105)

$$\sigma_s=\frac{F}{A}\cos\alpha\cos\beta \qquad [64]$$

where α and β are the angles between the direction of the applied force and the Burgers vector and normal to the slip plane, respectively. The resolved shear stress results in a strain rate following the constitutive behavior outlined in **Section 2.18.3.1.2**. The term $\cos\alpha\cos\beta$ is often referred to as the Schmid factor. Individual slip systems can be characterized by a critical resolved shear stress, which is the resolved shear stress necessary for dislocations in that slip system to produce deformation at a given strain rate. The glide of dislocations yields a change in the shape of a single crystal, which is dominated by the strain resulting from the most favorable slip system, that is, the slip system with the most advantageous combination of low critical resolved shear stress and high Schmid factor. The change in shape induces a rotation of the crystallographic reference frame relative to the direction of the applied force. Schmid and Boas (1950, pp. 58–63) demonstrated that this deformation is characterized (i) by the rotation of ***b*** toward the direction of an applied tensional force or (ii) by the rotation of the normal to the slip plane toward the direction of an applied compressional force. Because the rotation results in changes in the values of α and β, progressive deformation can lead to weakening or hardening of the crystal. In a polycrystalline rock, stresses and strain rates are partitioned among grains with a distribution of orientations. Although all grains are continually rotating, crystallographic textures can be developed if certain orientations are statistically favored (e.g., Wenk and Christie, 1991). For simple scenarios in which only a few slip systems are available, the orientation and shape of the crystallographic fabric can be used to infer the operative (dominant) slip planes and slip directions.

A wide range of experimental studies have linked texture development in rocks to deformation involving dislocations. As depicted in **Figure 20**, olivine-rich rocks deformed under dry, melt-free conditions in which $n>1$ exhibit a crystallographic fabric with most [010] axes normal to the slip plane and most [100] axes parallel to the shear direction, consistent with intragranular deformation dominantly produced by (010)[100] slip (Bystricky et al., 2000; Carter and Avé Lallemant, 1970; Hansen et al., 2012b; Nicolas et al., 1973; Zhang and Karato, 1995; Zhang et al., 2000). This observation is anticipated based on experiments on single crystals, which demonstrate that (010)[100] is the weakest slip system under the relevant conditions (Bai et al., 1991; Durham and Goetze, 1977). The similarity between fabrics developed in the laboratory and those observed in naturally deformed rocks (e.g., Ismail and Mainprice, 1998) suggests that the same mechanisms are accommodating deformation in both cases (**Figure 20**). Notably, most of the available creep data for aggregates of olivine have been obtained on samples deformed in the dislocation-accommodated grain-boundary sliding regime. Thus, even when sliding along grain boundaries contributes significantly to deformation, intragranular deformation appears to control grain rotations and produce strong crystallographic fabrics.

Because the weakest slip system has a significant influence on the orientation of the resulting crystallographic fabric, transitions in the relative strengths of slip systems result in a change in the crystallographic fabric. The relative strengths of slip systems depend on chemical environment (Bai et al., 1991; Mackwell et al., 1985) and thermomechanical conditions (Raterron et al.,

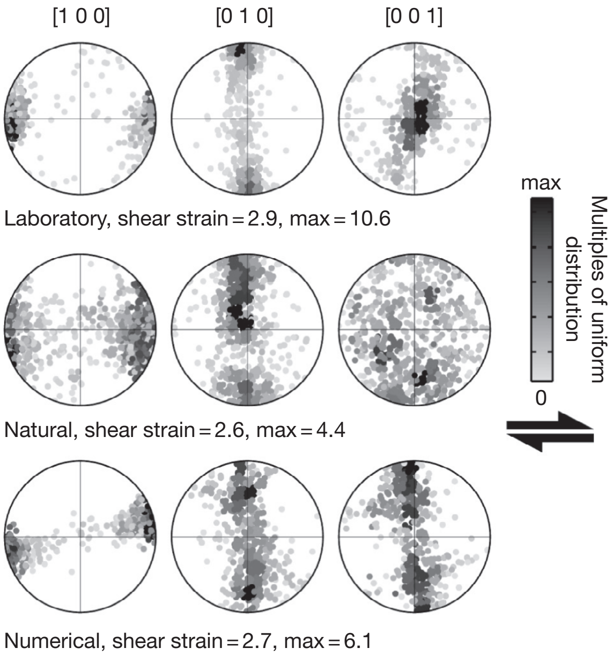

Figure 20 Olivine crystallographic fabrics observed in laboratory experiments, natural shear zones, and numerical simulations. All data are one point per grain plotted on equal-area lower hemisphere projections. Data from the laboratory are from a torsion experiment on an aggregate of Fo_{50} (Hansen et al., 2014). Data from nature are from a shear zone in the Josephine peridotite (Warren et al., 2008). Data from numerical simulation are from a calculation using the viscoplastic self-consistent approach with code provided by Ricardo Lebensohn (Lebensohn and Tomé, 1993).

2007, 2009, 2012); therefore, crystallographic fabrics provide valuable indicators of the thermodynamic state during deformation. As an important example, Mackwell et al. (1985) demonstrated that for single crystals, (001)[100] slip becomes easier than (010)[100] slip with a small addition of water; subsequently, Jung and Karato (2001) observed the related fabric transition in olivine aggregates. Further details of transitions in crystallographic fabrics associated with changes in experimental conditions are described by Mainprice (2007) and Karato et al. (2008).

Several studies have formulated numerical descriptions of the development of crystallographic fabrics in rocks, as reviewed by Karato (2008, pp. 262–265) and Wenk and Christie (1991). Crystallographic fabric development in geologic materials is a complex mechanical problem because many minerals exhibit fewer than five independent slip systems such that the von Mises compatibility criterion is not satisfied (von Mises, 1928). Some of the most computationally efficient formulations describe bulk behavior and do not deal with the complexity of grain–grain interactions (Mühlhaus et al., 2004; e.g., Lev and Hager, 2008); unfortunately, the necessary assumptions limit their applicability. Models that track multiple grains are bounded by those that assume all grains are deforming either at the same stress (Reuss, 1929) or at the same strain rate (Bishop and Hill, 1951; Taylor, 1938) with more sophisticated approaches allowing both the stress and strain rate to vary between grains. Many approaches use a self-consistent formalism in which each grain is considered to be interacting with a homogeneous surrounding medium (e.g., Lebensohn and Tomé, 1993). These methods include a second-order linearization (Castelnau et al., 2008; Ponte Castañeda, 2002) and an approximation to that linearization often referred to as the viscoplastic self-consistent model (Lebensohn and Tomé, 1993; Tommasi et al., 2000). **Figure 20**, which compares results from this latter approach to fabrics formed in naturally and experimentally deformed olivine-rich rocks, demonstrates that numerical simulations based on experimental results from deformation of single crystals can reasonably approximate deformation of aggregates, although significant differences remain.

2.18.3.3.2 Texture as a constraint on deformation mechanism

Because crystallographic fabrics are easily measureable and are, in general, directly related to the activity of dislocations during deformation, they are commonly used to infer the dominant deformation mechanism in both experimentally and naturally deformed rocks. As noted earlier in the text, strong crystallographic fabrics have been observed in laboratory experiments in which deformation involved dislocations. In contrast, relatively few experiments have been conducted in the diffusion creep regime to high enough strain to comment on fabric development. Samples from the few experiments that reached moderate strains in the diffusion creep regime exhibit either no or a relatively weak crystallographic fabric (Dell'Angelo and Olgaard, 1995; Fliervoet et al., 1999; Rutter and Brodie, 2004; Sundberg and Cooper, 2008). Thus, many studies have used the presence or lack of a crystallographic fabric to distinguish between deformation involving dislocations and that dominated by diffusion creep, respectively. However, several recent studies suggest that deformation by diffusion creep can result in relatively strong fabrics if there is significant anisotropy in grain shapes (Miyazaki, 2013; Wheeler, 2009) or anisotropy in diffusion or reaction kinetics (Sundberg and Cooper, 2008); thus, care must be taken if deformation mechanisms are inferred from crystallographic fabrics.

Several studies have used the strength of crystallographic fabrics measured in naturally deformed rocks to confirm extrapolations of laboratory-derived flow laws. Reductions in fabric strength have been correlated with the predicted transition from dislocation creep to diffusion creep or from dislocation-accommodated grain-boundary sliding to diffusion creep in plagioclase-rich mylonites (Mehl and Hirth, 2008), quartz-rich mylonites (Okudaira and Shigematsu, 2012), and olivine-rich mylonites (Linckens et al., 2011; Warren and Hirth, 2006). In these studies, the transition in deformation mechanism is hypothesized to result from reduced steady-state grain size of the primary phase due to dispersed secondary phases inhibiting grain growth (e.g., Olgaard, 1990). The relatively good agreement between transitions in crystallographic fabric strength and predicted transitions in deformation mechanism demonstrates the applicability of laboratory-derived constitutive equations to real-earth conditions.

2.18.3.3.3 Effect of texture on rock viscosity

In addition to being a valuable indicator of deformation mechanism, strong crystallographic fabrics result in macroscopically

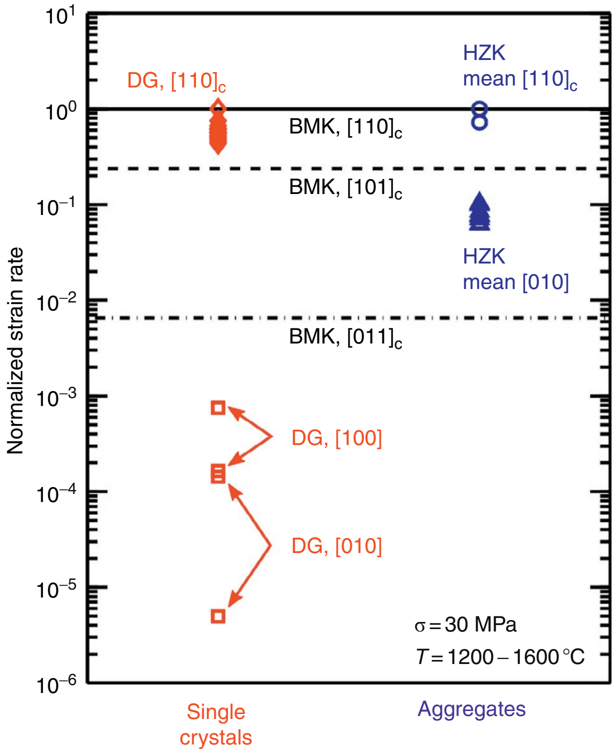

Figure 21 Normalized strain rates from experiments on both single crystals and polycrystalline aggregates illustrating the mechanical anisotropy of olivine. Single-crystal data are from Bai et al. (1991) (BMK) and Durham and Goetze (1977) (DG). Aggregate data are from Hansen et al. (2012a,b) (HZK). Strain rates are normalized by the highest rate in each group. Flow laws from Bai et al. (1991) are calculated for three different crystal orientations with the oxygen fugacity buffered by the Ni:NiO reaction with $T = 1200$ °C. Notation for crystal orientations follows Durham and Goetze (1977) and Bai et al. (1991). Because the strong crystallographic fabrics formed during the torsion experiments of Hansen et al. (2012a,b) have symmetry similar to olivine single crystals, data from torsion and tension experiments represent stress orientations similar to $[110]_c$ and [010], respectively. Data from Durham and Goetze (1977) were collected at $T = 1600$ °C, and data from Hansen et al. (2012a,b) were collected at $T = 1200$ °C.

anisotropic mechanical behavior. Many minerals are mechanically anisotropic as evidenced by deformation experiments on single crystals of varying orientations. In **Figure 21**, results of deformation experiments on olivine single crystals reveal a variation of over two orders of magnitude in viscosity depending on which slip systems are activated (Bai et al., 1991; Durham and Goetze, 1977). Further, in experiments with applied compressive stresses along the primary crystallographic axes of olivine single crystals for which there is no resolved shear stress on the available slip systems, viscosity is over three orders of magnitude larger than for orientations with large Schmid factors (Durham and Goetze, 1977).

Many of the numerical simulations used to predict texture development in geologic materials have also been used to estimate the magnitude of viscous anisotropy in those materials. Such models are currently the primary source for estimating the magnitude and symmetry of viscous anisotropy in Earth (for a review, see Wenk, 1999). Geologic materials investigated in this manner include ice (Castelnau et al., 1997; Lebensohn and Canova, 1996; Rudolph and Manga, 2012), halite (Siemes, 1974; Wenk et al., 1989a), calcite (Lebensohn et al., 1998; Tomé et al., 1991), quartz (Lister and Hobbs, 1980; Lister et al., 1978; Wenk et al., 1989b), olivine (Castelnau et al., 2008, 2009; Knoll et al., 2009; Lebensohn et al., 2010; Tommasi, 1998; Tommasi et al., 1999, 2000, 2009; Wenk and Tomé, 1999), and wadsleyite (Tommasi et al., 2004).

Several phenomenological constitutive models exist that describe the macroscopic behavior of anisotropic materials. In a manner similar to that used in elasticity theory, viscosity can be defined as a fourth-rank tensor, η_{ijkl}, which is related to the deviatoric stress tensor, σ_{ij}, and strain rate tensor, $\dot{\varepsilon}_{kl}$, through the expression

$$\sigma_{ij} = 2\eta_{ijkl}\dot{\varepsilon}_{kl} \qquad [65]$$

where subscripts indicate tensor indices following the Einstein convention. Commonly, the viscosity tensor is assumed to have transverse isotropy, which reduces the total number of independent components to three (e.g., Han and Wahr, 1997). Simplifying the problem to two dimensions further reduces the viscosity tensor to two components (Christensen, 1987; Honda, 1986). Although this approach allows easy incorporation into geodynamic models, it suffers from being limited to Newtonian viscosity, that is, a constitutive equation with a stress exponent of $n = 1$.

A nonlinear form of a power-law flow law was first extended to multiaxial deformation by Odqvist (e.g., Odqvist et al., 1962). Written in terms of fluidity rather than viscosity, which is more useful for application to laboratory experiments, this power-law relationship is

$$\dot{\varepsilon}_{ij} = \Phi_{ijkl}\sigma_{kl}\mathrm{II}_{\sigma}^{\left(\frac{n-1}{2}\right)} \qquad [66]$$

where Φ_{ijkl} is the fluidity tensor (the inverse of the viscosity tensor), II_{σ} is the second invariant of the deviatoric stress tensor, and n is the stress exponent. The von Mises equivalent stress is defined as $\sigma_e \equiv \sqrt{3\mathrm{II}_{\sigma}}$, which allows eqn [66] to be rewritten in Voigt notation as

$$\dot{\varepsilon}_i = 3^{-\left(\frac{n-1}{2}\right)}\Phi_{ij}\sigma_j\sigma_e^{(n-1)} \qquad [67]$$

Note that eqn [67] is equivalent to eqn [37] in Karato (2008). For the case in which the stress state is triaxial compression (i.e., $\sigma_1 > \sigma_2 = \sigma_3$ such that σ_e is equal to the differential stress) and the deformation maintains constant volume, the axial strain rate measured in the laboratory is given by

$$\dot{\varepsilon}_1 = 3^{-\left(\frac{n-1}{2}\right)}\Phi_{11}\sigma_e^n \qquad [68]$$

Note that, for triaxial compression, $\dot{\varepsilon}_1 = \dot{\varepsilon}_e$. If the stress state is simple shear (i.e., σ_6 is the only nonzero stress component), the shear strain rate measured in the laboratory is given by

$$\dot{\varepsilon}_6 = \Phi_{66}\sigma_6^n \qquad [69]$$

Note that, for simple shear, $\dot{\varepsilon}_6$ and σ_6 are related to the equivalent strain rate, $\dot{\varepsilon}_e$, and equivalent stress, σ_e, by $\dot{\varepsilon}_e = 2\dot{\varepsilon}_6/\sqrt{3}$ (where $2\dot{\varepsilon}_6$ is the engineering shear strain rate) and $\sigma_e = \sigma_6\sqrt{3}$, respectively. If the material is isotropic, then $\Phi_{66} = 2(\Phi_{11} - \Phi_{12})$ and, through conservation of volume, $\Phi_{66} = 3\Phi_{11}$

and $\Phi_{12} = -\frac{1}{2}\Phi_{11}$. Thus, the magnitude of viscous anisotropy can be assessed through comparison of the components of the fluidity tensor. A useful example is

$$\delta = \frac{\Phi_{66}}{3\Phi_{11}} \quad [70]$$

For an isotropic material, $\delta = 1$. If eqns [68] and [69] are combined with eqn [70], then

$$\delta = \left(\frac{\dot{\varepsilon}_{\mathrm{e,s}}}{\dot{\varepsilon}_{\mathrm{e,n}}}\right)\left(\frac{\sigma_{\mathrm{e,n}}}{\sigma_{\mathrm{e,s}}}\right)^{n} \quad [71]$$

where the subscripts s and n denote equivalent values measured in simple shear and triaxial compression or tension, respectively. Note that if the value of δ is assessed at constant equivalent stress, then eqn [71] reduces to the form used by Hansen et al. (2012a,b).

Relatively few laboratory-based experiments have measured the magnitude of viscous anisotropy in rocks. Muto et al. (2011) deformed quartz single crystals in three different orientations to high enough strains that dynamic recrystallization produced fine-grained aggregates with crystallographic fabrics with orientations controlled by the orientation of the starting single crystal. Their experiments demonstrate that slip on the basal plane is up to an order of magnitude less viscous than slip on the prism plane. Wendt et al. (1998) conducted experiments on cores of natural dunite with a preexisting crystallographic fabric. Although these experiments experienced extensive brittle and semibrittle deformation behavior, the viscosity was qualitatively determined to be a function of the orientation of the applied stress relative to the orientation of the preexisting fabric. As depicted in **Figure 20**, Hansen et al. (2012a) performed torsion tests on olivine aggregates and demonstrated that strong crystallographic fabrics favor slip on the weakest slip system and reduce the bulk flow stress by ~30% relative to an isotropic aggregate. Subsequent tension tests were performed on samples previously deformed in torsion with the tensional stress applied along the dominant [010] axis orientation, a geometry that minimizes the resolved shear stress on the available slip systems (Hansen et al., 2012a). These latter tests demonstrated that the viscosity of textured olivine aggregates can vary by over an order of magnitude depending on the orientation of the applied stress relative to the crystallographic fabric. However, the maximum anisotropy observed is still multiple orders of magnitude smaller than the anisotropy measured on olivine single crystals, which suggests that small misorientations between grains and the average orientation significantly affect the macroscopic viscosity.

Several lines of field evidence indicate that viscous anisotropy plays an important role in lithospheric deformation. The examination of mantle shear zones exposed in orogenic peridotites demonstrates that crystallographic fabrics have a controlling influence on shear zone orientation (Michibayashi and Mainprice, 2004). Further, the magnitude of localization in these shear zones can only be accounted for if viscous anisotropy is taken into account (Skemer et al., 2014). Investigations of upper mantle seismic anisotropy in regions of incipient rifting observe strong correlations between the orientation of seismic anisotropy and the trend of the rift axes (Vauchez et al., 1998). Additionally, some studies of lithospheric flexure have noted that the flexural rigidity of the lithosphere is anisotropic and the orientation of that anisotropy correlates well with the orientation of seismic anisotropy (Audet and Mareschal, 2004; Kirby and Swain, 2006; Simons and Van der Hilst, 2003).

2.18.4 Upper Mantle Viscosity

In this section, viscosity profiles for the oceanic upper mantle are calculated. Radial gradients in upper mantle viscosity are responsible for some of the key geodynamic characteristics of terrestrial planets. For instance, lithospheric plates act as a mechanical boundary layer to the convecting mantle because of a sharp transition to significantly lower viscosities in the underlying asthenosphere. Additionally, the presence of a sublithospheric minimum in viscosity (i.e., the asthenosphere) may be crucial for the operation of plate tectonics (Höink et al., 2012). Three sets of conditions are considered here: First, to examine the first-order effects of temperature and pressure, viscosity profiles are calculated assuming dry, melt-free conditions. Second, viscosity is calculated assuming the shallowest portions of the mantle are dry and the deeper portions have a water content of 800 ppm H/Si. Third, viscosity is calculated assuming the shallowest portions of the mantle are melt-free and the deeper portions are partially molten with a total melt fraction of 0.01.

Laboratory results for dunite (i.e., olivine volume fraction >95%) – rather than for harzburgite or lherzolite – are used because it is the only rock for which data are available over a wide range of upper mantle conditions. Justification for this choice is based on the observations that olivine is the major mineral in the upper mantle and that, under conditions for which data are available, the flow behavior of dunite is nearly identical to that of lherzolite (Zimmerman and Kohlstedt, 2004). Calculations are carried out assuming that dislocation creep, dislocation-accommodated grain-boundary sliding, and diffusion creep are all contributing to the strain rate independently. Flow-law parameters for dislocation creep and diffusion creep in olivine aggregates are largely taken from Hirth and Kohlstedt (2003) with the activation volume for wet dislocation creep taken to be $20 \times 10^{-6}\ \mathrm{m^3\ mol^{-1}}$ (Mei and Kohlstedt, 2000b), a value consistent with recent experiments on single crystals (Girard et al., 2013). Flow-law parameters for dislocation-accommodated grain-boundary sliding and a modification of the preexponential constant in the diffusion creep flow law are taken from Hansen et al. (2011). Grain size is assumed to be at the steady-state value described by the grain size–stress relationship determined experimentally by Karato et al. (1980). Activation volumes for dry dislocation creep and dislocation-accommodated grain-boundary sliding flow laws are taken from the results of experiments conducted on single crystals of olivine (Raterron et al., 2009, 2012). Because dislocation creep requires activation of all three primary dislocation slip systems in olivine to satisfy the von Mises criterion (von Mises, 1928), we suggest that the activation volume for dislocation creep is that of a single crystal deforming by the motion of dislocations of the strongest slip system, (010)[001] ($3 \times 10^{-6}\ \mathrm{m^3\ mol^{-1}}$). Similarly, because dislocation-accommodated grain-boundary sliding appears to require only the activation of a single slip system (Goldsby and Kohlstedt, 2001; Hirth and Kohlstedt, 2003), we suggest that the activation volume for grain-boundary sliding is that of a single crystal deforming by the motion of dislocations of the weakest slip system (010)[100] (12×10^{-6} m^3 mol^{-1}). Because (010)[001] slip is predicted to become easier than (010)[100] slip at depths greater than ~240 km (Raterron et al., 2012), we implement a corresponding switch in activation volume. Most calculations were carried out assuming that the differential stress is constant throughout the upper mantle. Values of the differential stress were chosen to yield magnitudes of viscosity that result in plate velocities of approximately 5 cm year^{-1} assuming a Couette flow geometry, which is equivalent to an average strain rate of 4×10^{-15} s^{-1} for a 400 km thick upper mantle.

2.18.4.1 Effect of Temperature and Pressure

In Figure 22(a), viscosity is depicted as a function of depth for dry, melt-free olivine. The temperature as a function of depth was determined for 50 million-year-old lithosphere using a half-space cooling model and an adiabatic geotherm with a potential temperature, T_p, of 1350 °C (Turcotte and Schubert, 2002, pp. 185–187). The resulting temperature profile is illustrated in Figure 22(b). A differential stress of $\sigma=0.8$ MPa was required to produce the desired plate velocity. A second calculation is depicted in which the rate of viscous energy dissipation per unit volume, $\sigma\dot{\varepsilon}$, is assumed to be constant (e.g., Christensen, 1989). For this second calculation, a dissipation rate of $\sigma\dot{\varepsilon}=4\times10^{-9}$ Pa s^{-1} was required to produce the desired plate velocity.

Because of the significant temperature dependence of the viscosity of mantle rocks, the shallowest and thus coldest portions of the upper mantle are characterized by large viscosities. Therefore, the thermal boundary layer inherent to the half-space cooling model yields a distinct mechanical boundary layer characterized by a viscosity that decreases by approximately a factor of 10 per 10 km.

The calculated viscosity profiles are also characterized by a minimum in viscosity at ~150 km, due to the increasing effect of pressure relative to that of temperature. Minimum viscosities

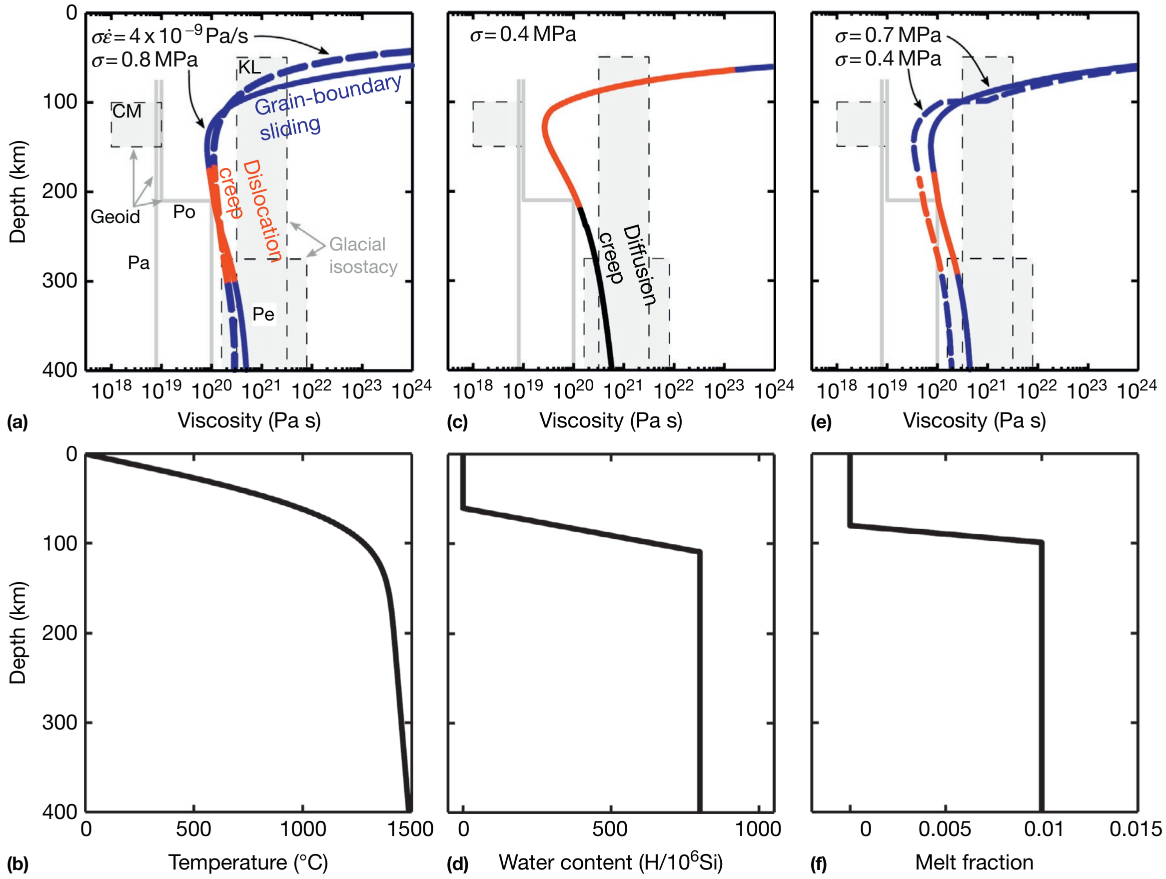

Figure 22 Viscosities as a function of depth in the upper mantle calculated using laboratory-derived flow laws for dunite. (a) Viscosities for dry, melt-free conditions calculated using both uniform stress (solid line) and uniform viscous dissipation rate (dashed line) and the temperature profile for 50 million-year-old lithosphere depicted in (b). The temperature profile in (b) was used for all calculations. Viscosity profiles are colored according to the mechanism of deformation that contributes most to the strain rate (dislocation creep = red; grain-boundary sliding = blue; diffusion creep = black). Viscosity profiles are compared to estimates from geophysical observations denoted by gray boxes and lines. Citation abbreviations are as follows: CM, Craig and McKenzie (1986); KL, Kaufmann and Lambeck (2002); Pa, Panet et al. (2010); Pe, Peltier (1998); Po, Pollitz et al. (2006). (c) Viscosities for hydrated conditions calculated using the profile of water content depicted in (d). (e) Viscosities for partially molten conditions calculated using the profile of melt fraction depicted in (f). Calculations for partially molten conditions were conducted assuming either homogeneously distributed melt (solid line) or melt segregated into melt-rich bands (dashed line).

are 8.1×10^{19} and 1.1×10^{20} Pa s for calculations assuming constant stress and constant dissipation rate, respectively. Below the viscosity minimum, viscosity increases by a factor of ~1.01 per 10 km. We note that the viscosity gradient below the viscosity minimum is distinctly less pronounced than previous calculations of mantle viscosity using laboratory-derived flow laws (e.g., Hirth and Kohlstedt, 2003) because of the recently determined activation volumes used here. Thus, solely the effects of temperature and pressure result in both a low-viscosity zone and a mechanical boundary between the lithosphere and asthenosphere.

Several interesting observations can be made regarding the relative contributions of different mechanisms to deformation. First, diffusion creep never dominates except in the coldest portions of the lithosphere. Instead, dislocation-accommodated grain-boundary sliding governs over the largest volume of the upper mantle. With increasing depth, the dominant mechanism switches to dislocation creep at ~175 km due to the different activation volumes for the hardest and easiest slip systems. Interestingly, the primary deformation mechanism again becomes dislocation-accommodated grain-boundary sliding at ~300 km because of the change in relative slip system strength. The observed distribution of deformation mechanisms is at odds with previous studies that have suggested diffusion creep is the dominant mechanism in the deeper portions of the upper mantle based on the lack of seismic anisotropy at those depths (e.g., Karato and Wu, 1993). We point out, however, that the magnitude of seismic anisotropy is a strong function of the total strain (e.g., Bystricky et al., 2000; Hansen et al., 2014). Since the strain can be multiple orders of magnitude larger near the viscosity minimum than at the base of the upper mantle, there can be significant gradients in the magnitude of seismic anisotropy even if dislocation creep or dislocation-accommodated grain-boundary sliding is the dominant flow mechanism (e.g., Behn et al., 2009; Podolefsky et al., 2004).

2.18.4.2 Effect of Water

In **Figure 22(c)**, viscosity is plotted as a function of depth for conditions similar to those used in the previous section but with the addition of a hydrated sublithospheric mantle. We construct a profile of water content as a function of depth following the argument of Hirth and Kohlstedt (1996). The uppermost portion of the mantle is considered to be free of water-related defects due to the extraction of water from mantle peridotites during partial melting at a mid-ocean ridge axis. We assume that olivine in the lower portion of the upper mantle has a constant water content of 800 ppm H/Si and that the water content gradually transitions from 0 to 800 ppm H/Si between 60 and 110 km depth. The increase in water content is formulated as a linear function of depth, which is expected for batch melting (Hirth and Kohlstedt, 1996). We note that using a nonlinear increase in water content, as expected for fractional melting, does not significantly affect the results of this calculation. The water content as a function of depth is depicted in **Figure 22(d)**.

The resulting viscosity profile is very similar to that depicted in **Figure 22(a)**. Gradients in viscosity at shallower depths than the viscosity minimum are comparable to those for the dry case. However, the magnitude of the viscosity minimum (2.8×10^{19} Pa s) is significantly less than for the dry case and the viscosity gradient below the viscosity minimum (factor of 1.6 per 10 km) is greater than for the dry case. Weakening associated with water-related defects is manifested in the differential stress being a factor of 2 lower than that for the dry case.

The dominant deformation mechanisms are distinctly different in the hydrated case compared to the dry case, primarily due to the absence of dislocation-accommodated grain-boundary sliding under hydrous conditions. This mechanism dominates in the dry upper 60 km of the model, but the dominant mechanism becomes dislocation creep once the water content increases at depths greater than 60 km. Diffusion creep becomes the dominant mechanism at a depth of 220 km and remains the dominant mechanism throughout the remainder of the upper mantle.

2.18.4.3 Effect of Melt and Melt Segregation

Figure 22(e) depicts the viscosity of the upper mantle calculated assuming dry conditions, as in **Figure 22(a)**, but including a small volume of melt. The melt fraction is assumed to be $\phi=0$ in the upper 80 km and to increase linearly to $\phi=0.01$ by 100 km depth (Langmuir et al., 1992).

The effect of a partial melting on viscosity is calculated using eqn [56] with $\alpha=35$ for both dislocation creep and dislocation-accommodated grain-boundary sliding flow laws and $\alpha=30$ for the diffusion creep flow law. Based on experiments on partially molten aggregates of olivine + chromite + MORB (Holtzman et al., 2003a,b; King et al., 2010), Holtzman et al. (2012) demonstrated that partially molten systems in which the melt segregates into melt-rich bands can have dramatically reduced viscosities. **Figure 22(e)** presents a second calculation that takes the effect of stress-driven melt segregation into account. Based on Holtzman et al. (2012), the total strain rate is taken to be

$$\dot{\varepsilon}=a_{\mathrm{b}}\dot{\varepsilon}_{\mathrm{b}}+\dot{\varepsilon}_{\mathrm{n}}a_{\mathrm{n}} \qquad [72]$$

where the subscripts b and n denote band (melt-enriched) and nonband (melt-depleted) regions, respectively, and a is the volume fraction of those regions. The volume fractions are given by

$$a_{\mathrm{b}}=\frac{\phi_{\mathrm{t}}S}{\phi_{\mathrm{b}}} \qquad [73a]$$

$$a_{\mathrm{n}}=1-a_{\mathrm{b}} \qquad [73b]$$

where ϕ_{t} and ϕ_{b} are the total melt fraction and the melt fraction in the bands, respectively. The total melt fraction is set to $\phi_{\mathrm{t}}=0.01$, and the melt fraction in the bands is set to $\phi_{\mathrm{b}}=0.15$. S describes the degree of melt segregation, which varies from 0 to 1 for a homogeneously distributed melt and a completely segregated melt, respectively. We use a value of $S=0.7$, which Holtzman et al. (2012) determined to be the steady-state value.

Both calculations involving melt-rich conditions result in viscosity profiles similar to the dry, melt-free case depicted in **Figure 22(a)**. Viscosity gradients above and below the viscosity minimum closely match those in **Figure 22(a)**. Additionally, the dominant deformation mechanisms and their depth ranges are approximately the same as in the dry, melt-free case. The melt-rich case without segregation results in a viscosity minimum (7.5×10^{-19} Pa s) similar in magnitude to the melt-free case, but the stress, $\sigma = 0.7$ MPa, is slightly less than the melt-free case. Notably, the melt-rich case with segregation results in a factor of eight reduction in viscosity at 100 km depth, corresponding to the increase in melt fraction. This sharp viscosity gradient illustrates the important role of stress-driven melt segregation in local viscosity reduction and the localization of deformation. The observed viscosity drop results in smaller minima in viscosity (3.4×10^{-19} Pa s) and stress (0.4 MPa) than in the case without segregation.

2.18.4.4 Comparison to Geophysical Observations

Several geophysical observations place constraints on the viscosity structure of the upper mantle. In **Figure 22(a), 22(c)**, and **22(e)**, calculated viscosity profiles are compared to estimates of upper mantle viscosity from observations of glacial isostatic adjustment and analyses of the geoid. Estimates of the globally averaged upper mantle viscosity from isostatic adjustment during the retreat of late Pleistocene ice sheets, as are illustrated in **Figure 22**, range from approximately 10^{20} to 10^{22} Pa s (Kaufmann and Lambeck, 2002; Peltier, 1998). Estimates of upper mantle viscosity from analyses of the geoid, as illustrated in **Figure 22**, are based either on geoid observations near oceanic fracture zones (Craig and McKenzie, 1986) or on post-seismic variation in the geoid after the 2004 Sumatra–Andaman earthquake (Panet et al., 2010; Pollitz et al., 2006). Estimates of viscosity based on post-seismic deformation range from 10^{18} to 10^{19} Pa s in the 100–150 km depth range and from 10^{19} to 10^{20} Pa s in the deep upper mantle.

The calculations based on laboratory-derived flow laws depicted in **Figure 22** correlate well with certain aspects of the geophysical observations and poorly with others. The viscosities predicted between depths of 100 and 400 km fall into a relatively narrow window ($10^{19.5}$ to $10^{20.5}$ Pa s). The predicted values near the base of the upper mantle overlap with those predicted by investigations of glacial isostatic adjustment. However, predicted viscosities are at least a half an order magnitude larger than estimates from observations of the geoid. Notably, none of the three sets of calculations (dry, wet, melt-rich) predict geophysically observed viscosity profiles significantly better than any of the others.

There are several potential explanations for the discrepancies between viscosities determined by geoid observations and those predicted by constitutive models. First, the age of the lithosphere in the region of the Mendocino Fracture Zone, for which the geoid was modeled (Craig and McKenzie, 1986), is significantly younger than that used to predict the thermal structure of the upper mantle in our calculations. Second, the viscous portion of the deformation subsequent to the 2004 Sumatra–Andaman earthquake was geologically fast and therefore characterized by small strains, a situation more akin to the transient portion of a stress-change test in the laboratory (Freed et al., 2012). For small strains after a stress increase, the viscous deformation of crystalline materials is typically characterized by a gradual increase in viscosity until a steady state is reached (e.g., Takeuchi and Argon, 1976). The flow laws used in our calculations are for steady-state deformation, which thus overestimate the viscosity for small strain deformation. Third, both stresses and strain rates during post-seismic deformation are likely increased relative to background tectonic values. Because the viscous deformation of the uppermost mantle is almost certainly non-Newtonian (i.e., stress exponent $n > 1$), an increase in stress results in a decrease in viscosity. Fourth, because our calculation is constrained to a set average strain rate, only a larger gradient in the viscosity as a function of depth allows for a lower viscosity minimum. Because the total accumulated strain in the upper mantle likely varies over multiple orders of magnitude as a function of depth (e.g., Behn et al., 2009), incorporating strain into constitutive models (e.g., Hansen et al., 2012a,b) would potentially result in large enough viscosity gradients to match predictions from geoid observations. With these caveats in mind, we suggest that particular attention must be made to thermal structure, timescale of deformation, stress during deformation, and deformation history in comparing different estimates of viscosity.

2.18.5 Concluding Remarks

While the good agreement between laboratory and field observations for the viscosity structure of the upper mantle is encouraging, even exciting, several important areas remain that require experimental investigation of the rheological properties of mantle rocks. Possibly the most obvious void is the paucity of deformation studies on transition zone and lower mantle minerals and rocks. Progress in this field has been slow, largely due to a lack of apparatuses capable of carrying out experiments under well-controlled thermomechanical conditions at very high pressures. However, recent developments combining a new generation of deformation apparatuses such as the deformation-DIA (D-DIA) and the rotational Drickamer apparatus (RDA) with high-intensity, synchrotron-produced x-rays hold promise for significant progress in this area (e.g., Durham et al., 2009; Hustoft et al., 2013; Mei et al., 2010; Raterron et al., 2011, 2012; Xu et al., 2005).

For the upper mantle, further work is needed to quantify the deformation behavior in the low-temperature plasticity regime, particularly under hydrous conditions, for application to studies of deformation of the lithosphere. Furthermore, laboratory (e.g., Jung and Karato, 2001) and seismic (e.g., Mainprice et al., 2005) observations indicate that a transition in slip system occurs below a depth of ~250 km in Earth's upper mantle, related to changes in water, stress, and/or pressure conditions. At present, flow laws for the upper mantle are primarily based on experiments carried out at relatively modest pressures for which measurements of lattice-preferred orientations indicate that deformation in olivine is dominated by dislocations with [100] Burgers vectors. If dislocations with [001] Burgers vectors become important in deeper portions of the upper mantle, the flow law determined at very high pressures may deviate from that extrapolated from lower-pressure conditions (Cordier et al., 2012; Couvy et al., 2004; Mainprice et al., 2005; Raterron et al., 2011, 2012).

Finally, to date, most studies of plastic deformation of rocks have concentrated on steady-state creep with little attention given to transient deformation. While a steady-state approach may describe convective flow in the mantle reasonably well, it cannot provide an adequate description of deformation that occurs in an environment for which thermomechanical conditions are changing and microstructures are simultaneously evolving (e.g., Evans, 2005). This point has been appreciated by a number of researchers, some of whom have taken a state-variable or mechanical equation-of-state approach (e.g., Covey-Crump, 1994, 1998; Lerner and Kohlstedt, 1981; Rutter, 1999; Stone et al., 2004). Such approaches will be critical in the development of the next generation of constitutive equations that must be capable of describing flow in regions such as shear zones and metamorphic belts in which changes in thermal and chemical environment – including composition of fluids and evolution of material's parameters (e.g., dislocation density, grain size, and lattice-preferred orientation) – occur continuously.

Acknowledgments

This work was supported by grants NASA-NNX10AM95G (deformation of nominally anhydrous minerals), NSF-OCE-1060983 (deformation of partially molten rocks), NSF-EAR-1214876 (viscous anisotropy), and DOE-DE-FG02-04ER15500 (low-temperature plasticity).

References

Ashby MF and Verrall RA (1973) Micromechanisms of flow and fracture and their relevance to the rheology of the upper mantle. *Philosophical Transactions of the Royal Society of London* A288: 59–95.

Atkinson A (1985) Grain boundary diffusion – Structural effects and mechanisms. *Journal de Physique* 46: 379–391.

Audet P and Mareschal JC (2004) Anisotropy of the flexural response of the lithosphere in the Canadian Shield. *Geophysical Research Letters* 31, L20601.

Avé Lallemant HG (1978) Experimental deformation of diopside and websterite. *Tectonophysics* 48: 1–27.

Avé Lallemant HG and Carter NL (1970) Syntectonic recrystallization of olivine and modes of flow in the upper mantle. *Geological Society of America Bulletin* 81: 2203–2220.

Bai Q and Kohlstedt DL (1992) High-temperature creep of olivine single crystals: 2. Dislocation microstructures. *Tectonophysics* 206: 1–29.

Bai Q, Mackwell SJ, and Kohlstedt DL (1991) High-temperature creep of olivine single crystals 1. Mechanical results for buffered samples. *Journal of Geophysical Research* 96: 2441–2463. http://dx.doi.org/10.1029/90JB01723.

Ball A and Hutchinson MM (1969) Superplasticity in the aluminium–zinc eutectoid. *Metal Science Journal* 3: 1–7.

Bardeen J and Herring C (1952) *Diffusion in alloys and the Kirkendall effect*. *Imperfections in Nearly Perfect Crystals*. New York: John Wiley, pp. 261–288.

Behn MD, Hirth G, and Elsenbeck JR (2009) Implications of grain size evolution on the seismic structure of the oceanic upper mantle. *Earth and Planetary Science Letters* 282: 178–189. http://dx.doi.org/10.1016/j.epsl.2009.03.014.

Bishop J and Hill R (1951) XLVI. A theory of the plastic distortion of a polycrystalline aggregate under combined stresses. *Philosophical Magazine* 42: 414–427.

Boullier AM and Gueguen Y (1975) Origin of some mylonites by superplastic flow. *Contributions to Mineralogy and Petrology* 50: 93–104.

Bystricky M, Kunze K, Burlini L, and Burg JP (2000) High shear strain of olivine aggregates: Rheological and seismic consequences. *Science* 290: 1564–1567. http://dx.doi.org/10.1126/science.290.5496.1564.

Bystricky M and Mackwell SJ (2001) Creep of dry clinopyroxene aggregates. *Journal of Geophysical Research* 106: 13443–13454.

Cannon WR and Langdon TG (1988) Review: Creep of ceramics. Part 2, An examination of flow mechanism. *Journal of Materials Science* 23: 1–20.

Carpenter Woods S, Mackwell SJ, and Dyar D (2000) Hydrogen in diopside: Diffusion profiles. *American Mineralogist* 85: 480–487.

Carter NL and Avé Lallemant HG (1970) High temperature deformation of dunite and peridotite. *Bulletin of the Geological Society of America* 81: 2181–2202.

Carter CB and Sass SL (1981) Electron diffraction and microscopy techniques for studying grain boundary structure. *Journal of the American Ceramic Society* 64(6): 335–345.

Castelnau O, Blackman DK, and Becker TW (2009) Numerical simulations of texture development and associated rheological anisotropy in regions of complex mantle flow. *Geophysical Research Letters* 36, L12304. http://dx.doi.org/10.1029/2009GL038027.

Castelnau O, Blackman D, Lebensohn R, and Castañeda PP (2008) Micromechanical modeling of the viscoplastic behavior of olivine. *Journal of Geophysical Research* 113, B09202. http://dx.doi.org/10.1029/2007JB005444.

Castelnau O, Canova G, Lebensohn R, and Duval P (1997) Modeling viscoplastic behavior of anisotropic polycrystalline ice with a self-consistent approach. *Acta Materialia* 45: 4823–4834.

Castelnau O, Cordier P, Lebensohn RA, Merkel S, and Raterron P (2010) Microstructures and rheology of Earth's upper mantle inferred from a multiscale approach. *Comptes Rendus Physique* 11: 304–315.

Catlow CRA, Bell RG, and Gale JD (1994) Computer modeling as a technique in materials chemistry. *Journal of Materials Chemistry* 4: 781–792. http://dx.doi.org/10.1039/JM9940400781.

Chan S-W and Balluffi RW (1985) Study of energy vs. misorientation for grain boundaries in gold by crystallite rotation method. I. (001) twist boundaries. *Acta Metallurgica* 33: 1113–1119.

Chan S-W and Balluffi RW (1986) Study of energy vs. misorientation for grain boundaries in gold by crystallite rotation method. II. Tilt boundaries and mixed boundaries. *Acta Metallurgica* 34: 2191–2199.

Chen S, Hiraga T, and Kohlstedt DL (2006) Water weakening of clinopyroxene in the dislocation creep regime. *Journal of Geophysical Research* 111, B08203. http://dx.doi.org/10.1029/2005JB003885.

Chopra PN and Paterson MS (1984) The role of water in the deformation of dunite. *Journal of Geophysical Research* 89: 7681–7876.

Christensen UR (1987) Some geodynamical effects of anisotropic viscosity. *Geophysical Journal of the Royal Astronomical Society* 91: 711–736. http://dx.doi.org/10.1111/j.1365-246X.1987.tb01666.x.

Christensen UR (1989) Mantle rheology, constitution, and convection. In: Peltier WR (ed.) *Mantle Convection: Plate Tectonics and Global Dynamics, The Fluid Mechanics of Astrophysics and Geophysics*, pp. 595–655. New York: Gordon and Breach Science Publishers.

Coble R (1963) A model for boundary diffusion controlled creep in polycrystalline materials. *Journal of Applied Physics* 34: 1679–1682.

Cooper RF and Kohlstedt DL (1982) Interfacial energies in the olivine–basalt system. In: Akimota S and Manghnani MH (eds.) *High-Pressure Research in Geophysics*, *Advances in Earth and Planetary Sciences*, vol. 12, pp. 217–228. Tokyo: Center for Academic Publications Japan.

Cooper RF and Kohlstedt DL (1984) Solution-precipitation enhanced diffusional creep of partially molten olivine–basalt aggregates during hot-pressing. *Tectonophysics* 107: 207–233.

Cooper RF and Kohlstedt DL (1986) Rheology and structure of olivine–basalt partial melts. *Journal of Geophysical Research* 91: 9315–9323.

Cooper RF, Kohlstedt DL, and Chyung K (1989) Solution-precipitation enhanced creep in solid–liquid aggregates which display a non-zero dihedral angle. *Acta Materialia* 37: 1759–1771.

Cordier P, Amodeo J, and Carrez P (2012) Modelling the rheology of MgO under Earth's mantle pressure, temperature and strain rates. *Nature* 481: 177–180.

Costa F and Chakraborty S (2008) Effect of water on Si and O diffusion rates in olivine and implications for transport properties and processes in the upper mantle. *Physics of the Earth and Planetary Interiors* 166: 11–29.

Couvy H, Frost D, Heidelbach F, et al. (2004) Shear deformation experiments of forsterite at 11 GPa–1400 °C in the multianvil apparatus. *European Journal of Mineralogy* 16: 877–889.

Covey-Crump SJ (1994) The application of Hart's state variable description of inelastic deformation to Carrara marble at $T < 450$ °C. *Journal of Geophysical Research* 99: 19793–19808.

Covey-Crump SJ (1998) Evolution of mechanical state in Carrara marble during deformation at 400° to 700 °C. *Journal of Geophysical Research* 103: 29781–29794.

Craig CH and McKenzie D (1986) The existence of a thin low-viscosity layer beneath the lithosphere. *Earth and Planetary Science Letters* 78: 420–426.

de Bresser JHP, Ter Heege JH, and Spiers CJ (2001) Grain size reduction by dynamic recrystallization: Can it result in major rheological weakening? *International Journal of Earth Sciences* 90: 28–45.

Dell'Angelo LN and Olgaard DL (1995) Experimental deformation of fine-grained anhydrite: Evidence for dislocation and diffusion creep. *Journal of Geophysical Research* 100: 15425–15440.

Demouchy S and Mackwell SJ (2003) Water diffusion in synthetic iron-free forsterite. *Physics and Chemistry of Minerals* 30: 486–494. http://dx.doi.org/10.1007/s00269-003-0342-2.

Devereux OF (1983) *Topics in Metallurgical Thermodynamics*. John Wiley & Sons, 494 pp.

Dieckmann R and Schmalzried H (1986) Defects and cation diffusion in magnetite (VI): Point defect relaxation and correlation in cation tracer diffusion. *Berichte der Bunsengesellschaft für Physikalische Chemie* 90: 564–575.

Dimos D, Wolfenstine J, and Kohlstedt DL (1988) Kinetic demixing and decomposition of multicomponent oxides due to a nonhydrostatic stress. *Acta Metallurgica* 36: 1543–1552.

Dohmen R, Chakraborty S, and Becker H-W (2002) Si and O diffusion in olivine and implications for characterizing plastic flow in the mantle. *Journal of Geophysical Research* 29: 2030. http://dx.doi.org/10.1029/2002GL015480.

Dorn JE (1956) *Some fundamental experiments on high temperature creep*. *Creep and Fracture of Metals at High Temperatures*. London: Her Majesty's Stationary Office, pp. 89–132.

Drury MR (2005) Dynamic recrystallization and strain softening of olivine aggregates in the laboratory and the lithosphere. In: Gapais D, Brun JP, and Cobbold PR (eds.) *Deformation Mechanisms, Rheology and Tectonics: from Minerals to the Lithosphere*, pp. 143–158. London: Geological Society, Special Publications 243.

Durham WB and Goetze C (1977) Plastic flow of oriented single crystals of olivine 1. Mechanical data. *Journal of Geophysical Research* 82: 5737–5753. http://dx.doi.org/10.1029/JB082i036p05737.

Durham WB, Goetze C, and Blake B (1977) Plastic flow of oriented single crystals of olivine, 2. Observations and interpretations of the dislocation structures. *Journal of Geophysical Research* 82: 5755–5770.

Durham WB, Mei S, Kohlstedt DL, Wang L, and Dixon NA (2009) New measurements of activation volume in olivine under anhydrous conditions. *Physics of the Earth and Planetary Interiors* 172: 67–73. http://dx.doi.org/10.1016/j.pepi.2008.07.045.

Durinck J, Legris A, and Courdier P (2005) Pressure sensitivity of olivine slip systems: First-principle calculations of generalised stacking faults. *Physics and Chemistry of Minerals* 42: 646–654.

Evans B (2005) Creep constitutive laws for rocks with evolving structure. In: Bruhn D and Burlini L (eds.) *High Strain Zones: Structure and Physical Properties*, pp. 329–346. London: Geological Society, Special Publications 245.

Evans B and Goetze C (1979) The temperature variation of hardness of olivine and its implications for polycrystalline yield stress. *Journal of Geophysical Research* 84: 5505–5524.

Evans HE and Knowles G (1978) Dislocation creep in non-metallic materials. *Acta Metallurgica* 26: 141–145.

Evans B and Kohlstedt DL (1995) Rheology of rocks. In: Ahrens (ed.) *Rock Physics and Phase Relations: A Handbook of Physical Constants*. Washington: American Geophysical Union, pp. 148–165.

Faul UH and Jackson I (2007) Diffusion creep of dry, melt-free olivine. *Journal of Geophysical Research* 112: B04204. http://dx.doi.org/10.1029/2006JB004586.

Fliervoet TF, Drury MR, and Chopra PN (1999) Crystallographic preferred orientations and misorientations in some olivine rocks deformed by diffusion or dislocation creep. *Tectonophysics* 303: 1–27.

Frank FC and Read WT (1950) Multiplication processes for slow moving dislocations. *Physics Review* 70: 722–723.

Freed AM, Hirth G, and Behn MD (2012) Using short-term postseismic displacements to infer the ambient deformation conditions of the upper mantle. *Journal of Geophysical Research* 117, B01409.

Frost HJ and Ashby MF (1982) *Deformation-Mechanism Maps: The Plasticity and Creep of Metals and Ceramics*. Pergamon Press, 166 pp.

Gifkins RC (1976) Grain-boundary sliding and its accommodation during creep and superplasticity. *Metallurgical Transactions A* 7A: 1225–1232.

Gifkins RC (1978) Grain rearrangements during superplastic deformation. *Journal of Materials Science* 13: 1924–1936.

Girard J, Chen J, Raterron P, and Holyoke CW (2013) Hydrolytic weakening of olivine at mantle pressure: Evidence of [100](010) slip system softening from single-crystal deformation experiments. *Physics of the Earth and Planetary Interiors* 216: 12–20. http://dx.doi.org/10.1016/j.pepi.2012.10.009.

Goetze C (1978) The mechanisms of creep in olivine. *Philosophical Transactions of the Royal Society A* 288: 99–119.

Goetze C and Kohlstedt DL (1973) Laboratory study of dislocation climb and diffusion in olivine. *Journal of Geophysical Research* 78: 5961–5971.

Goldsby DL and Kohlstedt DL (2001) Superplastic deformation of ice: Experimental observations. *Journal of Geophysical Research* 106: 11017–11030.

Gordon RS (1973) Mass transport in the diffusional creep of ionic solids. *Journal of the American Ceramic Society* 56: 147–152.

Griggs DT (1967) Hydrolytic weakening of quartz and other silicates. *Geophysical Journal of the Royal Astronomical Society* 14: 19–31.

Griggs DT (1974) A model of hydrolytic weakening in quartz. *Journal of Geophysical Research* 79: 1653–1661.

Griggs DT and Blacic JD (1965) Quartz: Anomalous weakness of synthetic crystals. *Science* 147: 292–295.

Groves GW and Kelly A (1969) Change of shape due to dislocation climb. *Philosophical Magazine* 19: 977–986.

Han D and Wahr J (1997) An analysis of anisotropic mantle viscosity, and its possible effects on post-glacial rebound. *Physics of the Earth and Planetary Interiors* 102: 33–50. http://dx.doi.org/10.1016/S0031-9201(96)03268-2.

Hansen LN, Zimmerman ME, and Kohlstedt DL (2011) Grain-boundary sliding in San Carlos olivine: Flow-law parameters and crystallographic-preferred orientation. *Journal of Geophysical Research* 116: B08201. http://dx.doi.org/10.1029/2011JB008220.

Hansen LN, Zimmerman ME, and Kohlstedt DL (2012a) Laboratory investigations of the viscous anisotropy of olivine aggregates. *Nature* 492: 415–418.

Hansen LN, Zimmerman ME, and Kohlstedt DL (2012b) The influence of microstructure on deformation of olivine in the grain-boundary sliding regime. *Journal of Geophysical Research* 117: B09201. http://dx.doi.org/10.1029/2012JB009305.

Hansen LN, Zhao YH, Zimmerman ME, and Kohlstedt DL (2014) Protracted fabric evolution in olivine: Implications for the relationship among strain, crystallographic fabric, and seismic anisotropy. *Earth and Planetary Science Letters* 387: 157–168.

Hercule S and Ingrin J (1999) Hydrogen in diopside: Diffusion, kinetics of extraction-incorporation, and solubility. *American Mineralogist* 84: 1577–1587.

Herring C (1950) Diffusional viscosity of a polycrystalline solid. *Journal of Applied Physics* 21: 437–445.

Hier-Majumder S, Anderson IM, and Kohlstedt DL (2005a) Influence of protons on Fe–Mg interdiffusion in olivine. *Journal of Geophysical Research* 110: B02202. http://dx.doi.org/10.1029/2004JB003292.

Hier-Majumder S, Mei S, and Kohlstedt DL (2005b) Water weakening in clinopyroxene in diffusion creep. *Journal of Geophysical Research* 110: B07406. http://dx.doi.org/10.1029/2004JB003414.

Hilbrandt N and Martin M (1998) High-temperature point defect equilibria in iron-doped MgO: An in situ Fe-K XAFS study on the valence and site distribution of iron in ($Mg_{1-x}Fe_x$)O. *Berichte der Bunsengesellschaft für Physikalische Chemie* 102: 1747–1759.

Hiraga T, Anderson IM, and Kohlstedt DL (2003) Chemistry of grain boundaries in mantle rocks. *American Mineralogist* 88: 1015–1019.

Hiraga T, Anderson IM, and Kohlstedt DL (2004) Partitioning in mantle rocks: Grain boundaries as reservoirs of incompatible elements. *Nature* 427: 699–703.

Hiraga T, Hirschmann MM, and Kohlstedt DL (2007) Equilibrium interface segregation in the diopside–forsterite system II: Applications of interface enrichment to mantle geochemistry. *Geochimica et Cosmochimica Acta* 71: 1281–1289. http://dx.doi.org/10.1016/j.gca.2006.11.020.

Hiraga T and Kohlstedt DL (2007) Equilibrium interface segregation in the diopside–forsterite system I: Analytical techniques, thermodynamics, and segregation characteristics. *Geochimica et Cosmochimica Acta* 71: 1266–1280. http://dx.doi.org/10.1016/j.gca.2006.11.019.

Hiraga T, Miyazaka T, Tasaka M, and Yoshida H (2010) Mantle superplasticity and its self-made demise. *Nature* 468: 1091–1094.

Hirsch PB (1979) A mechanism for the effect of doping on dislocation mobility. *Journal de Physique, Colloque* 40(C6): 117–121.

Hirsch PB (1981) Plastic deformation and electronic mechanisms in semiconductors and insulators. *Journal de Physique, Colloque* 42(C3): 149–159.

Hirth G and Kohlstedt DL (1995a) Experimental constraints on the dynamics of the partially molten upper mantle. Deformation in the diffusion creep regime. *Journal of Geophysical Research* 100: 1981–2001.

Hirth G and Kohlstedt DL (1995b) Experimental constraints on the dynamics of the partially molten upper mantle. 2. Deformation in the dislocation creep regime. *Journal of Geophysical Research* 100: 15441–15449.

Hirth G and Kohlstedt DL (1996) Water in the oceanic upper mantle: Implications for rheology, melt extraction and the evolution of the lithosphere. *Earth and Planetary Science Letters* 144: 93–108.

Hirth G and Kohlstedt DL (2003) Rheology of the upper mantle and the mantle wedge: A view from the experimentalists. In: Eiler J (ed.) *Inside the Subduction Factory*. *Geophysical Monograph*, vol. 138, pp. 83–105. Washington, DC: American Geophysical Union.

Hirth G and Kohlstedt DL (2014). The stress dependence of olivine creep rate: Implications for extrapolation of lab data and interpretation of recrystallized grain size. *Tectonophysics*, submitted for publication.

Hirth JP and Lothe J (1968) *Theory of Dislocations*. New York: McGraw-Hill Book Company, 780 pp.

Hobbs BE (1981) The influence of metamorphic environment upon the deformation of materials. *Tectonophysics* 78: 335–383.

Hobbs BE (1983) Constraints on the mechanism of deformation of olivine imposed by defect chemistry. *Tectonophysics* 78: 335–383.

Hobbs BE (1984) Point defect chemistry of minerals under hydrothermal environment. *Journal of Geophysical Research* 89: 4026–4038.

Höink T, Adrian L, and Mark R (2012) Depth-dependent viscosity and mantle stress amplification: implications for the role of the asthenosphere in maintaining plate tectonics. *Geophysical Journal International* 191(1): 30–41.

Holtzman BK, Groebner NH, Zimmerman ME, Ginsberg SB, and Kohlstedt DL (2003a) Deformation-driven melt segregation in partially molten rocks. *Geochemistry, Geophysics, Geosystems* 4: 8607. http://dx.doi.org/10.1029/2001GC000258.

Holtzman BK, King DSH, and Kohlstedt DL (2012) Effects of stress-driven melt segregation on the viscosity of rocks. *Earth and Planetary Science Letters* 359: 184–193.

Holtzman BK, Kohlstedt DL, and Phipps Morgan J (2005) Viscous energy dissipation and strain partitioning in partially molten rocks. *Journal of Petrology* http://dx.doi.org/10.1093/petrology/egi065.

Holtzman BK, Kohlstedt DL, Zimmerman ME, Heidelbach F, Hiraga T, and Hustoft J (2003b) Melt segregation and strain partitioning: Implications for seismic anisotropy and mantle flow. *Science* 301: 1227–1230.

Honda S (1986) Strong anisotropic flow in a finely layered asthenosphere. *Geophysical Research Letters* 13(13): 1454–1457. http://dx.doi.org/10.1029/GL013i013p01454.

Hustoft J, Amulele G, Ando J-I, et al. (2013) Plastic deformation experiments to high strain on mantle transition zone minerals wadsleyite and ringwoodite in the rotational Drickamer apparatus. *Earth and Planetary Science Letters* 361: 7–15.

Hutchinson JW (1976) Bounds and self-consistent estimates for creep of polycrystalline materials. *Proceeding of the Royal Society of London* 348: 101–127.

Ingrin J, Hercule S, and Charton T (1995) Diffusion of hydrogen in diopside: Results of dehydration experiments. *Journal of Geophysical Research* 100: 15489–15499.

Ingrin J and Skogby H (2000) Hydrogen in nominally anhydrous upper-mantle minerals: Concentration levels and implications. *European Journal of Mineralogy* 12: 543–570.

Ismail WB and Mainprice D (1998) An olivine fabric database: An overview of upper mantle fabrics and seismic anisotropy. *Tectonophysics* 296: 145–157. http://dx.doi.org/10.1016/S0040-1951(98)00141-3.

Jaoul O (1990) Multicomponent diffusion and creep in olivine. *Journal of Geophysical Research* 95: 17631–17642.

Jung H and Karato S-i (2001) Water-induced fabric transitions in olivine. *Science* 293: 1460–1463.

Kaibyshev O (1992) *Superplasticity of Alloys, Intermetallides, and Ceramics*. Berlin/New York: Springer, 317 pp.

Kaibyshev OA (2002) Fundamental aspects of superplastic deformation. *Materials Science and Engineering A* 324: 96–102.

Karato S-I (2008) *Deformation of Earth Materials: An Introduction to Rheology of Solid Earth*. New York: Cambridge University Press, 463 pp.

Karato S-i and Jung H (2003) Effects of pressure on high-temperature dislocation creep in olivine. *Philosophical Magazine* 83: 401–414.

Karato S, Jung H, Katayama I, and Skemer P (2008) Geodynamic significance of seismic anisotropy of the upper mantle: New insights from laboratory studies. *Annual Review of Earth and Planetary Sciences* 36: 59–95. http://dx.doi.org/10.1146/annurev.earth.36.031207.124120.

Karato S-I, Paterson MS, and Fitz Gerald JD (1986) Rheology of synthetic olivine aggregates; influence of grain size and water. *Journal of Geophysical Research* 91: 8151–8176.

Karato S and Sato H (1982) The effect of oxygen partial pressure on the dislocation recovery in olivine: A new constraint on creep mechanisms. *Physics of the Earth and Planetary Interiors* 28: 312–319.

Karato S, Toriumi M, and Fujii T (1980) Dynamic recrystallization of olivine single crystals during high-temperature creep. *Geophysical Research Letters* 7: 649–652. http://dx.doi.org/10.1029/GL007i009p00649.

Karato S and Wu P (1993) Rheology of the upper mantle: A synthesis. *Science* 260: 771–778. http://dx.doi.org/10.1126/science.260.5109.771.

Kaufmann G and Lambeck K (2002) Glacial isostatic adjustment and the radial viscosity profile from inverse modeling. *Journal of Geophysical Research* 107: 2280. http://dx.doi.org/10.1029/2001JB000941.

Keefner JW, Mackwell SJ, Kohlstedt DL, and Heidelback F (2011) Dependence of the creep of dunite on oxygen fugacity: Implications for viscosity variations in Earth's mantle. *Journal of Geophysical Research* 116: B05201. http://dx.doi.org/10.1029/2010JB007748.

Kelemen PB and Dick HJB (1995) Focused melt flow and localized deformation in the upper mantle: Juxtaposition of replacive dunite and ductile shear zones in the Josephine Peridotite, SW Oregon. *Journal of Geophysical Research* 100: 423–438.

Kelemen PB, Hirth G, Shimizu N, Spiegelman M, and Dick HJB (1997) A review of melt migration processes in the adiabatically upwelling mantle beneath spreading ridges. *Philosophical Transactions of the Royal Society of London A* 355: 283–318.

Kelly A and Groves GW (1970) *Crystallography and Crystal Defects*. Addison-Wesley Publishing Company, 428 pp.

King D, Zimmerman ME, and Kohlstedt DL (2010) Stress-driven melt segregation in partially molten olivine-rich rocks deformed in torsion. *Journal of Petrology* 51: 21–42. http://dx.doi.org/10.1093/petrology/egp062.

Kirby J and Swain C (2006) Mapping the mechanical anisotropy of the lithosphere using a 2D wavelet coherence, and its application to Australia. *Physics of the Earth and Planetary Interiors* 158: 122–138.

Knoll M, Tommasi A, Logé RE, and Signorelli JW (2009) A multiscale approach to model the anisotropic deformation of lithospheric plates. *Geochemistry, Geophysics, Geosystems* 10: Q08009. http://dx.doi.org/10.1029/2009GC002423.

Kocks UF, Argon AS, and Ashby MF (1975) Thermodynamics and kinetics of slip. *Progress in Materials Sciences*19: New York: Pergamon Press, 288 pp.

Kohlstedt DL (1992) Structure, rheology and permeability of partially molten rocks at low melt fractions. In: Phipps-Morgan J, Blackman DK, and Sinton JM (eds.) *Mantle Flow and Melt Generation at Mid-Ocean Ridges*. *Geophys. Monogr*, vol. 71, pp. 103–121. Washington: American Geophysical Union.

Kohlstedt DL (2002) Partial melting and deformation. In: Karato S-I and Wenk HR (eds.) *Plastic Deformation in Minerals and Rocks*. *Reviews in Mineralogy and Geochemistry*, vol. 51, pp. 105–125. Mineralogical Society of America.

Kohlstedt DL (2006) The role of water in high-temperature rock deformation. In: Keppler H and Smyth J (eds.) *Water in Nominally Anhydrous Minerals*. *Reviews in Mineralogy and Geochemistry*, vol. 62, pp. 377–396. Mineralogical Society of America.

Kohlstedt DL, Evans B, and Mackwell SJ (1995) Strength of the lithosphere: Constraints imposed by laboratory experiments. *Journal of Geophysical Research* 100: 17587–17602.

Kohlstedt DL and Holtzman BK (2009) Shearing melt out of the earth: An experimentalist's perspective on the influence of deformation on melt extraction. *Annual Review of Earth and Planetary Sciences* 37: 561–593. http://dx.doi.org/10.1146/annurev.earth.031208.100104.

Kohlstedt DL and Mackwell SJ (1998) Diffusion of hydrogen and intrinsic point defects in olivine. *Zeitschrift für Physikalische Chemie* 207: 147–162.

Kohlstedt DL and Mackwell SJ (1999) Solubility and diffusion of 'water' in silicate minerals. In: Catlow R and Wright K (eds.) *Microscopic Properties and Processes in Minerals*, pp. 539–559. Kluwer Academic Publishers.

Kohlstedt DL, Nichols HPK, and Hornack P (1980) The effect of pressure on dislocation recovery in olivine. *Journal of Geophysical Research* 85: 3122–3130.

Kohlstedt DL and Zimmerman ME (1996) Rheology of partially molten mantle rocks. *Annual Review of Earth and Planetary Sciences* 24: 41–62.

Kohlstedt DL, Zimmerman ME, and Mackwell SJ (2010) Stress-driven melt segregation in partially molten feldspathic rocks. *Journal of Petrology* 52: 9–19. http://dx.doi.org/10.1093/petrology/egp043.

Kröger FA and Vink HJ (1956) Relation between the concentrations of imperfections in crystalline solids. In: Seitz F and Turnball D (eds.) *Solid State Physics*, vol. 3, pp. 307–435. San Diego, CA: Academic Press.

Kronenberg AK, Kirby SH, Aines RD, and Rossman GR (1986) Solubility and diffusional uptake of hydrogen in quartz at high water pressures: Implications for hydrolytic weakening. *Journal of Geophysical Research* 91: 12723–12744.

Kronenberg AK and Tullis J (1984) Flow strengths of quartz aggregates: Grain size and pressure effects due to hydrolytic weakening. *Journal of Geophysical Research* 89: 4281–4297.

Langdon TG (1994) A unified approach to grain-boundary sliding in creep and superplasticity. *Acta Metallurgica et Materialia* 42: 2437–2443.

Langdon TG (1995) Mechanisms of superplastic flow. In: Ridley N (ed.) *Superplasticity: 60 years after Pearson*, pp. 9–24. London: Institute of Materials.

Langmuir CH, Klein EM, and Plank T (1992) *Petrological systematics of mid-ocean ridge basalts: Constraints on melt generation beneath ocean ridges. Mantle Flow and Melt Generation at Mid-Ocean Ridges*, vol. 71. Washington, DC: American Geophysical Union, pp. 183–200.

Lebensohn RA and Canova GR (1996) Viscoplastic modeling of texture development in polycrystalline ice with a self-consistent approach: Comparison with bound estimates. *Journal of Geophysical Research* 101: 13–851.

Lebensohn RA, Hartley CS, Tomé CN, and Castelnau O (2010) Modeling the mechanical response of polycrystals deforming by climb and glide. *Philosophical Magazine* 90: 567–583. http://dx.doi.org/10.1080/14786430903213320.

Lebensohn RA and Tomé C (1993) A self-consistent anisotropic approach for the simulation of plastic deformation and texture development of polycrystals: Application to zirconium alloys. *Acta Metallurgica et Materialia* 41: 2611–2624.

Lebensohn RA, Wenk HR, and Tomé C (1998) Modelling deformation and recrystallization textures in calcite. *Acta Materialia* 46: 2683–2693.

Lerner I and Kohlstedt DL (1981) Effect of γ radiation on plastic flow of NaCl. *Journal of the American Ceramic Society* 64: 105–108.

Lev E and Hager BH (2008) Prediction of anisotropy from flow models: A comparison of three methods. *Geochemistry, Geophysics, Geosystems* 9, Q07014.

Liftshitz IM (1963) On the theory of diffusion-viscous flow of polycrystalline bodies. *Journal of Experimental and Theoretical Physics* 17: 909–920.

Linckens J, Herwegh M, Müntener O, and Mercolli I (2011) Evolution of a polymineralic mantle shear zone and the role of second phases in the localization of deformation. *Journal of Geophysical Research* 116: B06210. http://dx.doi.org/10.1029/2010JB008119.

Lister GS and Hobbs BE (1980) The simulation of fabric development during plastic deformation and its application to quartzite; the influence of deformation history. *Journal of Structural Geology* 2: 355–370.

Lister GS, Paterson MS, and Hobbs BE (1978) The simulation of fabric development in plastic deformation and its application to quartzite: The model. *Tectonophysics* 45: 107–158.

Mackwell SJ, Dimos D, and Kohlstedt DL (1988) Transient creep of olivine: Point defect relaxation times. *Philosophical Magazine A* 57: 779–789.

Mackwell SJ and Kohlstedt DL (1990) Diffusion of hydrogen in olivine: Implications for water in the mantle. *Journal of Geophysical Research* 95: 5079–5088.

Mackwell SJ, Kohlstedt DL, and Paterson MS (1985) The role of water in the deformation of olivine single crystals. *Journal of Geophysical Research* 90: 11319–11333.

Mainprice D (2007) Seismic anisotropy of the deep Earth from a mineral and rock physics perspective. *Treatise on Geophysics* 2: 437–492.

Mainprice D, Tommasi A, Couvy H, Cordier P, and Frost DJ (2005) Pressure sensitivity of olivine slip systems and seismic anisotropy of Earth's upper mantle. *Nature* 433: 731–733.

McCarthy C and Takei Y (2011) Anelasticity and viscosity of partially molten rock analogue: Toward seismic detection of small quantities of melt. *Geophysical Research Letters* 38. http://dx.doi.org/10.1029/2011GL048776.

Mehl L and Hirth G (2008) Plagioclase preferred orientation in layered mylonites: Evaluation of flow laws for the lower crust. *Journal of Geophysical Research* 113, B05202.

Mei S, Bai W, Hiraga T, and Kohlstedt DL (2002) Influence of water on plastic deformation of olivine-basalt aggregates. *Earth and Planetary Science Letters* 201: 491–507.

Mei S and Kohlstedt DL (2000a) Influence of water on plastic deformation of olivine aggregates: 2. Dislocation creep regime. *Journal of Geophysical Research* 105: 21471–21481.

Mei S and Kohlstedt DL (2000b) Influence of water on plastic deformation of olivine aggregates 1. Diffusion creep regime. *Journal of Geophysical Research* 105: 21457–21469.

Mei S, Suzuki AN, Kohlstedt DL, Dixon NA, and Durham WB (2010) Experimental constraints on the strength of the lithospheric mantle. *Journal of Geophysical Research* 115: B08204. http://dx.doi.org/10.1029/2009JB006873.

Michibayashi K and Mainprice D (2004) The role of pre-existing mechanical anisotropy on shear zone development within oceanic mantle lithosphere; an example from the Oman Ophiolite; Orogenic lherzolites and mantle processes. *Journal of Petrology* 45: 405–414.

Mishin Y and Herzig C (1999) Grain boundary diffusion: Recent progress and future research. *Materials Science and Engineering* A260: 55–71.

Miyazaki T, Sueyoshi K, and Hiraga T (2003) Olivine crystals align during diffusion creep of Earth/'s upper mantle. *Nature* 502: 321–326.

Mott NF (1951) The mechanical properties of metals. *Proceedings of the Physical Society* 64: 729–742.

Mott NF (1953) A theory of work hardening of metals, II, flow without slip lines, recovery and creep. *Philosophical Magazine* 44: 742.

Mott NF (1956) *A discussion of some models of the rate-determining process in creep. Creep and Fracture of Metals at High Temperatures*. London: Her Majesty's Stationary Office, pp. 21–24.

Mühlhaus HB, Moresi L, and Cada M (2004) Emergent anisotropy and flow alignment in viscous rock. *Pure and Applied Geophysics* 161: 2451–2463.

Mukerjee AK, Bird JE, and Dorn JE (1969) Experimental correlations for high-temperature creep. *Transaction of ASM* 62: 155–179.

Mukherjee AK (1971) The rate controlling mechanism in superplasticity. *Materials Science and Engineering* 8: 83–89.

Muto J, Hirth G, Heilbronner R, and Tullis J (2011) Plastic anisotropy and fabric evolution in sheared and recrystallized quartz single crystals. *Journal of Geophysical Research* 116, B02206.

Nabarro F (1948) *Deformation of crystals by the motion of single ions*. *Report on a Conference on the Strength of Solids*. London: Physical Society, pp. 75–90.

Nabarro FRN (1967) Steady-state diffusional creep. *Philosophical Magazine* 16: 231–237.

Nakamura A and Schmalzried H (1983) On the nonstoichiometry and point defects of olivine. *Physics and Chemistry of Minerals* 10: 27–37.

Nakamura A and Schmalzried H (1984) On the Fe^{2+}–Mg^{2+} interdiffusion in olivine. *Berichte der Bunsengesellschaft für Physikalische Chemie* 88: 140–145.

Nicolas A, Boudier F, and Boullier A (1973) Mechanisms of flow in naturally and experimentally deformed peridotites. *American Journal of Science* 273: 853–876.

Nix WD, Gasca-Neri R, and Hirth JP (1971) A contribution to the theory of dislocation climb. *Philosophical Magazine* 23: 1339–1349.

Odqvist, Folke KG, and Jan Hult (1962) *Kriechfestigkeit metallischer Werkstoffe*, vol. 18. Berlin: Springer.

Okudaira T and Shigematsu N (2012) Estimates of stress and strain rate in mylonites based on the boundary between the fields of grain-size sensitive and insensitive creep. *Journal of Geophysical Research* 117, B03210.

Olgaard DL (1990) *The Role of Second Phase in Localizing Deformation*. London: Geological Society, Special Publications, 54, pp. 175–181.

Orowan E (1940) Problems of plastic gliding. *Proceedings of the Physical Society* 52: 8–22.

Panet I, Pollitz F, Mikhailov V, Diament M, Banerjee P, and Grijalva K (2010) Upper mantle rheology from GRACE and GPS postseismic deformation after the 2004 Sumatra–Andaman earthquake. *Geochemistry, Geophysics, Geosystems* 11: Q06008.

Paterson MS (1969) The ductility of rocks. In: Argon AS (ed.) *Physics of Strength and Plasticity*, pp. 377–392. Cambridge, MA: MIT Press.

Peach MO and Koehler JS (1950) The forces exerted on dislocations and the stress fields produced by them. *Physics Review* 80: 436–439.

Peltier W (1998) *Global glacial isostasy and relative sea level: Implications for solid Earth geophysics and climate system dynamics*. *Dynamics of the Ice Age Earth*. pp. 17–54.

Platt JP and Behr WM (2011) Grainsize evolution in ductile shear zones: Implications for strain localization and the strength of the lithosphere. *Journal of Structural Geology* 33: 537–550.

Podolefsky NS, Zhong S, and McNamara AK (2004) The anisotropic and rheological structure of the oceanic upper mantle from a simple model of plate shear. *Geophysical Journal International* 158: 287–296. http://dx.doi.org/10.1111/j.1365-246X.2004.02250.x.

Poirier JP (1985) *Creep of Crystals: High-temperature Deformation Processes in Metals*. *Ceramics and Minerals*. Cambridge: Cambridge University Press, 260 pp.

Pollitz FF, Bürgmann R, and Banerjee P (2006) Post-seismic relaxation following the great 2004 Sumatra–Andaman earthquake on a compressible self-gravitating Earth. *Geophysical Journal International* 167: 397–420.

Ponte Castañeda P (2002) Second-order homogenization estimates for nonlinear composites incorporating field fluctuations: I—Theory. *Journal of the Mechanics and Physics of Solids* 50: 737–757.

Post AD, Tullis J, and Yund RA (1996) Effects of chemical environment on dislocation creep of quartzite. *Journal of Geophysical Research* 101: 22143–22155.

Poumellec B and Jaoul O (1984) Influence of pO_2 and pH_2O on the high temperature plasticity of olivine. In: Tressler RE and Bradt RC (eds.) *Deformation of Ceramic Materials II*. *Materials Science Research*, vol. 18, pp. 281–305. New York: Plenum Press.

Pshenichnyuk AI, Astanin VV, and Kaibyshev OA (1998) The model of grain-boundary sliding stimulated by intragranular slip. *Philosophical Magazine A* 77: 1093–1106.

Raj R and Ashby MF (1971) On grain-boundary sliding and diffusional creep. *Metallurgical Transactions A* 2: 1113–1127.

Raterron P, Amiguet E, Chen J, Li L, and Cordier P (2009) Experimental deformation of olivine single crystals at mantle pressure and temperature. *Physics of the Earth and Planetary Interiors* 172: 74–83.

Raterron P, Chen J, Geenen T, and Girard J (2011) Pressure effect on forsterite dislocation slip systems: Implications for upper-mantle LPO and low viscosity zone. *Physics of the Earth and Planetary Interiors* 188: 26–36.

Raterron P, Chen J, Li L, Weidner D, and Cordier P (2007) Pressure-induced slip-system transition in forsterite; single-crystal rheological properties at mantle pressure and temperature. *American Mineralogist* 92: 1436–1445.

Raterron P, Girard J, and Chen J (2012) Activities of olivine slip systems in the upper mantle. *Physics of the Earth and Planetary Interiors* 200–201: 105–112.

Read WT Jr. (1953) *Dislocations in Crystals*. New York: McGraw-Hill Book Company, 175 pp.

Read WT and Shockley W (1950) Dislocation models of crystal grain boundaries. *Physics Review* 78: 275–289.

Ready DW (1966) Chemical potentials and initial sintering in pure metals and ionic compounds. *Journal of Applied Physics* 37: 2309–2312.

Reuss A (1929) Calculation of the flow limits of mixed crystals on the basis of the plasticity of monocrystals. *Zeitschrift für Angewandte Mathematik und Mechanik* 9: 49–58.

Ricoult DL and Kohlstedt DL (1983a) Structural width of low-angle grain boundaries in olivine. *Physics and Chemistry of Minerals* 9: 133–138.

Ricoult DL and Kohlstedt DL (1983b) Low-angle grain boundaries in olivine. In: Yan MF and Heuer AH (eds.) *Advances in Ceramics, Character of Grain Boundaries*, vol. 6, pp. 59–72. Columbus: American Ceramic Society.

Ricoult DL and Kohlstedt DL (1985) Experimental evidence for the effect of chemical environment upon the creep rate of olivine. In: Schock RN (ed.) *Point Defects in Minerals*, pp. 171–184. Washington: Amer. Geophys. Union.

Ridley N (1995) C.E. Pearson and his observations of superplasticity. In: Ridley N (ed.) *Superplasticity: 60 Years after Pearson*, pp. 1–5. London: Institute of Materials.

Riley GN Jr. and Kohlstedt DL (1990) An experimental study of melt migration in an olivine-melt system. In: Ryan MP (ed.) *Magma Transport and Storage*, pp. 77–86. New York: John Wiley & Sons.

Roscoe R (1952) The viscosity of suspensions of rigid spheres. *British Journal of Applied Physics* 3: 267–269.

Rudolph M and Manga M (2012) Effects of anisotropic viscosity and texture development on convection in ice mantles. *Journal of Geophysical Research: Planets, 1991–2012,* 117.

Ruoff AL (1965) Mass transfer problems in ionic crystals with charge neutrality. *Journal of Applied Physics* 36: 2903–2907.

Rutter EH (1999) On the relationship between the formation of shear zones and the form of the flow law for rocks undergoing dynamic recrystallization. *Tectonophysics* 303: 147–158.

Rutter E and Brodie K (2004) Experimental grain size-sensitive flow of hot-pressed Brazilian quartz aggregates. *Journal of Structural Geology* 26: 2011–2023.

Rutter EH, Brodie KH, and Irving DH (2006) Flow of synthetic, wet, partially molten “granite” under undrained conditions: An experimental study. *Journal of Geophysical Research* 111: B06407. http://dx.doi.org/10.1029/2005JB004257.

Rutter EH and Neumann DHK (1995) Experimental deformation of partially molten Westerly granite, with implications for the extraction of granitic magmas. *Journal of Geophysical Research* 100: 15697–15715.

Rybacki E and Dresen G (2000) Dislocation and diffusion creep of synthetic anorthite aggregates. *Journal of Geophysical Research* 105: 26017–26036.

Schmalzried H (1981) *Solid State Reactions*, 2nd edn. Weinheim: Verlag Chemie, 254 pp.

Schmalzried H (1995) *Chemical Kinetics of Solids*. New York: VCH Publishers, 433 pp.

Schmid E and Boas W (1950) *Plasticity of Crystals with Special Reference to Metals*. London: F.A. Hughes.

Schmid S, Boland JN, and Paterson MS (1977) Superplastic flow in fine grained limestone. *Tectonophysics* 43: 257–291.

Scott T and Kohlstedt DL (2006) The effect of large melt fraction on the deformation behavior of peridotite. *Earth and Planetary Science Letters* 246: 177–187.

Sherby OD and Burke PM (1967) Mechanical behavior of crystalline solids at elevated temperature. In: Chalmers B and Hume-Rothery W (eds.) *Progress in Materials Science*, vol. 13, pp. 325–390. New York: Pergamon Press.

Shewmon PG (1983) *Diffusion in Solids*. Jenks, OK: J. Williams Book Company, 203 pp.

Siemes H (1974) Anwendung der Taylor-Theorie auf die Regelung von kubischen Mineralen. *Contributions to Mineralogy and Petrology* 43: 149–157.

Simons FJ and van der Hilst RD (2003) Seismic and mechanical anisotropy and the past and present deformation of the Australian lithosphere. *Earth and Planetary Science Letters* 211: 271–286.

Skemer P, Warren JM, Hansen LN, Hirth G, and Kelemen PB. The influence of water and LPO on the initiation and evolution of mantle shear zones. *Earth and Planetary Science Letters*, submitted for publication.

Spingarn JR, Barnett DM, and Nix WD (1979) Theoretical descriptions of climb controlled steady state creep at high and intermediate temperatures. *Acta Metallurgica* 27: 1549–1561.

Stalder R and Skogby H (2003) Hydrogen diffusion in natural and synthetic orthopyroxene. *Physics and Chemistry of Minerals* 30: 12–19.

Stevenson DJ (1989) Spontaneous small-scale melt segregation in partial melts undergoing deformation. *Geophysical Research Letters* 16: 1067–1070.

Stone DS, Plookphol T, and Cooper RF (2004) Similarity and scaling in creep and load relaxation of single-crystal halite (NaCl). *Journal of Geophysical Research* 109. http://dx.doi.org/10.1029/2004JB003064.

Sundberg M and Cooper RF (2008) Crystallographic preferred orientation produced by diffusional creep of harzburgite: Effects of chemical interactions among phases during plastic flow. *Journal of Geophysical Research* 113: B12208. http://dx.doi.org/10.1029/2008JB005618.

Takei Y (2005) Deformation-induced grain boundary wetting and its effects on the acoustic and rheological properties of partially molten rock analogue. *Journal of Geophysical Research* 110: B12203. http://dx.doi.org/10.1029/2005JB003801.

Takei Y and Holtzman BK (2009a) Viscous constitutive relations of solid–liquid composites in terms of grain boundary contiguity: 1. Grain boundary diffusion control model. *Journal of Geophysical Research* 114, B06205.

Takei Y and Holtzman BK (2009b) Viscous constitutive relations of solid–liquid composites in terms of grain boundary contiguity: 3. Causes and consequences of viscous anisotropy. *Journal of Geophysical Research* 114, B06207.

Takei Y and Katz RF (2013) Consequences of viscous anisotropy in a deforming, two-phase aggregate. Part 1. Governing equations and linearized analysis. *Journal of Fluid Mechanics* 734: 424–455. http://dx.doi.org/10.1017/jfm.2013.482.

Takeuchi S and Argon AS (1976) Review: Steady-state creep of single-phase crystalline matter at high temperature. *Journal of Materials Science* 11: 1542–1566.

Taylor SGI (1938) Plastic strain in metals. *Journal of the Institute of Metals* 62: 307–323.

Tomé C, Wenk HR, Canova G, and Kocks U (1991) Simulations of texture development in calcite: Comparison of polycrystal plasticity theories. *Journal of Geophysical Research* 96: 11865–11875.

Tommasi A (1998) Forward modeling of the development of seismic anisotropy in the upper mantle. *Earth and Planetary Science Letters* 160: 1–13. http://dx.doi.org/10.1016/S0012-821X(98)00081-8.

Tommasi A, Knoll M, Vauchez A, Signorelli JW, Thoraval C, and Logé R (2009) Structural reactivation in plate tectonics controlled by olivine crystal anisotropy. *Nature Geoscience* 2: 423–427. http://dx.doi.org/10.1038/ngeo528.

Tommasi A, Mainprice D, Canova G, and Chastel Y (2000) Viscoplastic self-consistent and equilibrium-based modeling of olivine lattice preferred orientations: Implications for the upper mantle seismic anisotropy. *Journal of Geophysical Research* 105: 7893–7908. http://dx.doi.org/10.1029/1999JB900411.

Tommasi A, Mainprice D, Cordier P, Thoraval C, and Couvy H (2004) Strain-induced seismic anisotropy of wadsleyite polycrystals and flow patterns in the mantle transition zone. *Journal of Geophysical Research* 109. http://dx.doi.org/10.1029/2004JB003158 B12405.

Tommasi A, Tikoff B, and Vauchez A (1999) Upper mantle tectonics: Three-dimensional deformation, olivine crystallographic fabrics and seismic properties. *Earth and Planetary Science Letters* 168(1–2): 173–186. http://dx.doi.org/10.1016/S0012-821X(99)00046-1.

Tsai T-L and Dieckmann R (2002) Variations in the oxygen content and point defects in olivines (Fex, Mg1 $-x$)$_2$SiO4, 0.2–1.0. *Physics and Chemistry of Minerals* 29: 680–694.

Tullis J and Yund RA (1980) Hydrolytic weakening of experimentally deformed Westerly granite and Hale albite rock. *Journal of Structural Geology* 2: 439–451.

Tullis J and Yund RA (1985) Dynamic recrystallization of feldspar: A mechanism for ductile shear zone formation. *Geology* 13: 238–241.

Turcotte DL and Schubert G (2002) *Geodynamics*, 2nd edn Cambridge: Cambridge University Press, 456 pp.

Vauchez A, Tommasi A, and Barruol G (1998) Rheological heterogeneity, mechanical anisotropy and deformation of the continental lithosphere. *Tectonophysics* 296: 61–86. http://dx.doi.org/10.1016/S0040-1951(98)00137-1.

von Mises R (1928) Mechanik der plastischen Formänderung von Kristallen. *Zeitschrift für angewandte Mathematik und Mechanik* 8: 161–185.

Wanamaker BJ (1994) Point defect diffusivities in San Carlos olivine derived from reequilibration of electrical conductivity following changes in oxygen fugacity. *Geophysical Research Letters* 21: 21–24.

Wang Z, Zhao Y, and Kohlstedt DL (2010) Dislocation creep accommodated by grain-boundary sliding in dunite. *Journal of Earth Science* 21: 541–554. http://dx.doi.org/10.1007/s12583-010-0113-1.

Warren JM and Hirth G (2006) Grain size sensitive deformation mechanisms in naturally deformed peridotites. *Earth and Planetary Science Letters* 248: 438–450. http://dx.doi.org/10.1016/j.epsl.2006.06.006.

Warren JM, Hirth G, and Kelemen PB (2008) Evolution of olivine lattice preferred orientation during simple shear in the mantle. *Earth and Planetary Science Letters* 272: 501–512. http://dx.doi.org/10.1016/j.epsl.2008.03.063.

Weertman J (1955) Theory of steady-state creep based on dislocation climb. *Journal of Applied Physics* 26: 1213–1217.

Weertman J (1957a) Steady-state creep through dislocation climb. *Journal of Applied Physics* 28: 362–364.

Weertman J (1957b) Steady-state creep of crystals. *Journal of Applied Physics* 28: 1185–1189.

Weertman J (1978) Creep laws for the mantle of the Earth. *Philosophical Transactions of the Royal Society of London A* 288: 9–26.

Weertman J (1999) Microstructural mechanisms of creep. In: Meyers MA, Armstrong RW, and Kirschner H (eds.) *Mechanics and Materials: Fundamentals and Linkages*, pp. 451–488. New York: John Wiley & Sons.

Weertman J and Weertman JR (1992) *Elementary Dislocation Theory*. Oxford: Oxford University Press, 213 pp.

Wendt AS, Mainprice D, Rutter E, and Wirth R (1998) A joint study of experimental deformation and experimentally induced microstructures of pretextured peridotites. *Journal of Geophysical Research* 103: 18205–18221. http://dx.doi.org/10.1029/98JB01555.

Wenk HR (1999) A voyage through the deformed Earth with the self-consistent model. *Modelling and Simulation in Materials Science and Engineering* 7: 699–722.

Wenk HR, Canova G, Molinari A, and Kocks U (1989a) Viscoplastic modeling of texture development in quartzite. *Journal of Geophysical Research* 94: 17895–17906.

Wenk H, Canova G, Molinari A, and Mecking H (1989b) Texture development in halite: Comparison of Taylor model and self-consistent theory. *Acta Materialia* 37: 2017–2029.

Wenk HR and Christie JM (1991) Comments on the interpretation of deformation textures in rocks. *Journal of Structural Geology* 13: 1091–1110.

Wenk H and Tomé C (1999) Modeling dynamic recrystallization of olivine aggregates deformed in simple shear. *Journal of Geophysical Research* 104: 513–525.

Wheeler J (2009) The preservation of seismic anisotropy in the Earth's mantle during diffusion creep. *Geophysical Journal International* 178: 1723–1732. http://dx.doi.org/10.1111/j.1365-246X.2009.04241.x.

Xu Y, Nishihara Y, and Karato S-i (2005) Development of a rotational Drickamer apparatus for large-strain high-pressure deformation experiments. In: Chen J, Wang Y, Duffy TS, Shen G, and Dobrzhinetskaya LF (eds.) *Frontier of High-Pressure Research: Applications to Geophysics*, pp. 167–182. Amsterdam: Elsevier.

Xu Y, Zimmerman ME, and Kohlstedt DL (2004) Deformation behavior of partially molten mantle rocks. In: Karner GD, Driscoll NW, Taylor B, and Kohlstedt DL (eds.) *Rheology and Deformation of the Lithosphere at Continental Margins*. *MARGINS Theoretical and Experimental Earth Science Series*, vol. 1, pp. 284–310. Columbia University Press.

Yurek GJ and Schmalzried H (1974) Interdiffusion in the (A, B)O system and the validity of Darken's equation. *Berichte der Bunsengesellschaft für Physikalische Chemie* 78: 1379–1386.

Zhang S and Karato S (1995) Lattice preferred orientation of olivine aggregates deformed in simple shear. *Nature* 375: 774–777.

Zhang S, Karato S, Fitzgerald J, Faul UH, and Zhou Y (2000) Simple shear deformation of olivine aggregates. *Tectonophysics* 316: 133–152. http://dx.doi.org/10.1016/S0040-1951(99)00229-2.

Zimmerman ME and Kohlstedt DL (2004) Rheological properties of partially molten lherzolite. *Journal of Petrology* 45: 275–298.

Zimmerman ME, Zhang S, Kohlstedt DL, and Karato S (1999) Melt distribution in mantle rocks deformed in shear. *Geophysical Research Letters* 26: 1505–1508.